The vorticity dynamics of coastal currents and outflows

Sean Jamshidi

Department of Mathematics
University College London

A thesis submitted in conformity with the requirements for the degree of Doctor of Philosophy

Supervised by Prof. E. R. Johnson

July, 2020

I, Sean Jamshidi, confirm that the work presented in this thesis is my own. Where information has been derived from other sources, I confirm that this has been indicated in the thesis.

Abstract

This thesis is concerned with the interaction between an along-shore coastal current and flow driven by a jump in potential vorticity. In particular, we develop and apply idealised models for a river outflow, a potential vorticity front, and waves generated by changes in continental-shelf width. In all cases the model ocean has one active layer with piecewise-uniform potential vorticity, and analytic progress is made by assuming the flow varies slowly in the along-shore direction. The behaviour of the model depends strongly on whether the vorticity dynamics reinforce or oppose the coastal current, and on the relative strengths of these two effects.

In the outflow model, vorticity is generated by stretching or squashing of fluid columns as they leave the source and adjust to the depth of the upper ocean layer. We explore how this basic mechanism affects the behaviour of the outflow plume by extending the quasi-geostrophic model of Johnson et al. [2017]. In chapter 2, we extend Johnson et al.'s model to order-one Rossby number using the semi-geostrophic equations, and show that the same range of behaviours occurs. In chapter 3 we allow the potential vorticity of the outflow to vary in space, and show that the behaviour of the resulting plume depends on the net contribution of vorticity at the source.

Chapter 4 considers free waves on a potential vorticity front, and shows how they are affected by the presence of a coast. The evolution of the front is described by a nonlinear finite-amplitude equation including first-order dispersive effects, which is analysed using 'dispersive shock-fitting' [El, 2005]. Chapter 5 extends this model to include the continental shelf, and shows that the flow can become hydraulically controlled when the background current opposes coastal-trapped wave propagation.

Impact statement

The models developed below are simple representations of coastal flows, and thus provide insight into the underlying dynamics which can in principle be applied to any coastal region. Chapters 2-3 explore how vorticity dynamics affect the behaviour of river water once it discharges into the ocean. River water transports nutrients, pollutants and sediments from the land to the sea and thus river plumes play an important role in coastal ecosystems. Real river plumes display a 'menagerie' of behaviours, and there are many theoretical, experimental, numerical and observational studies that seek to explain these differences. The results presented here contribute to this discussion by isolating the role of source vorticity, and showing that this mechanism alone can produce the three most commonly observed behaviours. Further, §2 identifies the nonlinear Kelvin wave as an important dynamical feature of the ocean's response to an outflow, and the concept of vorticity competition discussed in §3 contributes to the general problem of flow around a curved wall. Both of these topics are of interest to experimentalists wishing to understand fundamental properties of rotating flows, and the idealised nature of the models used here makes them well-suited to comparison with laboratory experiments.

In §§4-5, theoretical predictions from a dispersive long-wave model are compared to contour-dynamic simulations of the full quasi-geostrophic system. The high level of agreement between these two indicates that first-order dispersive effects are sufficient to capture the quantitative long-time behaviour of the full system, and thus the analytical techniques applied below (dispersive shock fitting, hydraulic and dispersive critical control) are useful in studying a wider range of quasi-geostrophic flows. In addition to its analytic properties, numerical integration of the long-wave model is orders of magnitude faster than contour dynamics. Researchers investigating similar problems thus may use the long-wave model to first explore the parameter space, and then select particular values for use in contour dynamics.

Coastal-trapped waves, which are the topic of §5, form a major component of high-frequency variability in the coastal oceans. However, these waves are too small to be resolved directly by global climate models and must instead be included through parameterisation. A greater understanding of how the properties of these waves relate to known data such as coastal bathymetry is thus important for improving the reliability of model output. Chapter 5 shows that sufficiently large changes in shelf width can lead to reduced alongshore transport, and thus provides further evidence of the importance of bathymetry-aware parameterisations. This chapter was also guided

by an ongoing discussion with researchers at Johns Hopkins Earth and Planetary Sciences, who are interested in the possibility that coastal-trapped waves may contribute to melting of the Greenland ice sheet.

The results presented here have produced three publications in peer-reviewed journals [Jamshidi and Johnson, 2019a,b, 2020]. Presentations based on these results have also been given at several conferences in the U.K. (British Applied Mathematics Colloquium, 2017, 2018, 2019; The dynamics of rotating fluids, 2017, 2020) and internationally (Japan Geoscience Union, 2018; AGU Ocean Sciences, 2020) to audiences in both mathematics and oceanography. Communication between these two disciplines is vital; as a way of providing insight into observations and for understanding the limits of idealised models.

Acknowledgements

I am extremely grateful to all those who have provided support, encouragement, perspective and welcome distraction during the last four years, including the UCL mathematics department staff and faculty, my Ph.D. colleagues and friends—particularly Andrew, Matty, Olivia and Ollie, my sister Kathryn, and my parents Carol and Bahman.

Education is a lifelong journey and I am lucky to have had many caring and dedicated mentors along the way so far. I would particularly like to acknowledge Peter Bigwood, Aled Williams, Andrew Hodges, Phil Trinh, Mary-Louise Timmermans and of course Ted Johnson, who supervised this thesis. Working with Ted has been a joy, and I have benefited enormously from his insight, experience and honesty, his continued enthusiasm for our research, and his encouragement to take advantage of opportunities for personal and professional development.

This thesis is dedicated to my grandparents, Barbara and Roy.

Contents

List of Figures

List of Tables

Chapter 1

Introduction

1.1 Coastal outflows

Rivers play an important role in the transport of nutrients, sediment and pollutants from the land to the sea, and as such the dynamics of coastal outflow plumes is an active area of study. Outflow plumes that are large enough to be affected by planetary rotation often comprise two distinct parts: an anticylonic gyre or 'bulge' of fresh water that accumulates near the river mouth, and a coastally-trapped current that transports some or all of the outflow away from the mouth in the direction of Kelvin-wave propagation [Horner-Devine et al., 2015]. This prototypical structure has been observed in the Chang Jiang, Hudson and Columbia river plumes [Beardsley et al., 1985, Chant et al., 2008, Horner-Devine, 2009], as well as in laboratory and numerical studies [Avicola and Huq, 2003a,b, Chen, 2014]. However some river plumes do not typically develop bulges, and instead all of the outflow volume is transported away from the source by the coastal current. This 'coastal-current mode' has been observed in the Delaware and Chesapeake bay plumes [Münchow and Garvine, 1993a,b, Donato and Marmorino, 2002] and, in one particularly striking example, after the removal of a hydroelectric dam on the Elwha river released a large amount of silt into the Strait of Juan De Fuca, leaving the shape of the outflow plume clearly visible from the air (figure 1.1). Other plumes may operate in either mode at different times of the year [Conlon, 1982, Shetye et al., 1993]. This wide range of behaviours is a result of nonlinear interaction between many influencing factors including

Figure 1.1: A hydroelectric dam on the Elwha river was removed in 2014, releasing a large build up of silt into the Strait of Juan De Fuca, where it formed a coastal current. Image reproduced by permission of Tom Roorda.

outflow buoyancy, rotation, bathymetry, tides and currents, and highlights the importance of theoretical or numerical studies that seek to isolate the contribution made by each of these. Here our focus is on the vorticity-driven dynamics of outflow plumes, and in particular how vorticity generated at the mouth of the river affects plume behaviour. A convenient way to visualise the effect of source vorticity on plume behaviour is through the so-called 'method of images'. A cyclonic vortex near a vertical, impermeable boundary propagates in the direction of Kelvin-wave flow (rightward in the Northern hemisphere, referred to hereafter as downstream) under the influence of its image, while an anticyclonic vortex propagates upstream. In the context of a coastal outflow cyclonic vorticity increases transport in the coastal current, while anticyclonic vorticity feeds the bulge and can even drive fluid upstream in the direction opposite to Kelvin-wave propagation [Garvine, 2001, Magome and Isobe, 2003, Johnson et al., 2017].

Although it is known that vorticity plays an important role in outflow dynamics, it is not clear how source vorticity can be controlled in a laboratory, or even measured at the required scales in real plumes (see §4.3 of Crawford [2017] for a discussion of the difficulties involved). Thus one way to make progress is to relate coastal-current transport to properties

of the bulge rather than of the outflow profile [Nof and Pichevin, 2001, Chen, 2014]. While these theories have been successful at explaining coastal current transport, it is not clear how one could determine the properties of the bulge a priori. An alternative approach that incorporates source conditions is to parameterise vorticity using the source Rossby number $\mathrm{Ro_S} = U_\mathrm{S}/(fW)$. Here U_S is a scaling for the outflow velocity, f is the Coriolis frequency and W is the width of the river mouth. The source Rossby number thus gives the ratio of source vorticity to the background rotation rate [Fong and Geyer, 2002, Horner-Devine et al., 2006]. However as noted by Horner-Devine et al. [2015], the empirical relationship derived in these experiments suggests that coastal current transport depends only weakly on the source Rossby number.

1.1.1 Idealised models of coastal outflows

Another way to avoid the difficulties associated with measuring source vorticity is to use an idealised, inviscid model where the potential vorticity (PV) of the outflow can be specified. Kubokawa [1991] uses a quasi-geostrophic (QG) model in which the outflow has the same density as a buoyant upper layer of oceanic fluid. Part of the outflow has the same PV as the (uniform) upper ocean layer, and the remainder has a lower PV. Possible flows are split into three distinct modes depending on the total volume and PV distribution of the outflow. These modes are a steady coastal current, a widening current, and the prototypical anticyclonic gyre and coastal current mode. Johnson et al. [2017] (JSM hereafter) employ a similar model where the outflow has uniform PV, and show that the dynamics are governed by the PV anomaly (PVa) of the outflow. If the upper ocean layer is deeper than the river mouth (positive PVa) then fluid columns stretch on leaving the source and, by PV conservation, gain positive vorticity. The source vorticity is cyclonic everywhere and all the outflow travels downstream, leading to a steady, constant-width coastal current and no bulge formation. On the other hand, if the upper layer is shallower than the river mouth (negative PVa) then fluid columns squash on leaving and gain negative vorticity. In some cases, this leads to an outflow where the source vorticity is negative everywhere and so all fluid turns left, forming an upstream coastal current with only a fraction of the outflow eventually recirculating downstream. JSM identify two mechanisms that drive the flow in their model: flow driven downstream by a Kelvin wave and flow driven by image vorticity. The vortical flow is caused by the PV jump and, depending on the sign of the PVa, can drive fluid in either

direction. In fact Johnson and McDonald [2006] show that in the vorticity-dominated limit all of the outflow turns left and the coastal current flows upstream.

In §2, we extend the quasi-geostrophic model of JSM to allow order-one Rossby number. That is, we allow the difference between the initial upper-layer depth and the PV depth of the river water to be of arbitrary magnitude. Analytical progress relies on invoking a long-wave assumption—that along-shore scales are large compared to cross-shore scales. This results in a semi-geostrophic (geostrophic balance alongshore only) set of equations, which have been used previously for studying similar problems involving coastal currents with uniform PV [Stern, 1980, Stern et al., 1982, Kubokawa and Hanawa, 1984a, Stern and Helfrich, 2002]. The boundary of these currents can be completely described by similarity solutions that relate the current width to the velocity at the current edge. Similar ideas are applicable for the present set-up in regimes where the flow evolves to become steady. These steady flows can be matched with unsteady coastal currents away from the source region, and thus it is possible to develop a full theory for the behaviour of the plume that depends only on the non-dimensional PVa and the outflow mass flux.

In §3, we return to the quasi-geostrophic model and allow the outflow to have spatially-varying PV. In particular we choose the PV distribution such that the outflow has a region of positive vorticity on the left and a region of negative vorticity on the right, looking seaward. Image vorticity drives a tendency for fluid emerging from each region to turn and propagate into the other, and so we call such an outflow 'competitive'. Alternatively, if the outflow consists of a region of negative vorticity on the left and a region of positive vorticity on the right, there is no competition and the fluid with negative vorticity turns upstream unimpeded. This chapter thus generalises the work of Kubokawa [1991] to include a wider range of PV distributions, and re-analyses previous results within the framework of vorticity competition. We derive a simple constraint on the source vorticity that must be satisfied in order for the outflow to operate in coastal current mode.

1.1.2 Validity of the coastal outflow model

The models developed here are not appropriate for quantitative comparison with real outflows, due to two important simplifications. Firstly, neither model allows the plume boundary to outcrop, and so ignores horizontal density gradients. However, the interaction between vorticity dynamics and

Kelvin-wave flow which is the main focus of this work is still relevant in a more realistic setting, and may sometimes (for example, in the limit of weak horizontal stratification) be a dominant factor in determining plume behaviour. Secondly, we have chosen to model the coast as a vertical wall and are thus ignoring the effect of topographic stretching, which introduces additional cyclonic vorticity into the plume. The role played by topography in plume behaviour is discussed at length in Garvine [2001] and Pimenta et al. [2011], but as it pertains to the present work we note that for a steep bottom slope the plume is known to be 'surface advected' and the influence of topography is small [Yankovsky and Chapman, 1997].

Two important parameters in the theoretical study of coastal outflows are the source Rossby number $\mathrm{Ro_S}$ discussed above and the Kelvin number, $K = W/L_\mathrm{R}$, where $L_\mathrm{R} = c/f$ is the Rossby radius of deformation (here $c = (g'H)^{1/2}$ is the internal gravity-wave speed for a layered model, with g' the reduced gravity for the active layer and H a depth scale to be chosen later). The Kelvin number was introduced by Garvine [1995] as a means of classifying plume behaviour. Outflows with large K have relatively slow flow and are in geostrophic balance, whereas those with small K are little-affected by rotation. Huq [2009] presents laboratory experiments showing that bulges only form in outflows with $K < 1$, while Garvine [1995] notes that real outflows fall into the 'large-K regime' when K is as small as 2. Note that the two parameters differ only in their choice of velocity scale; that is $K^{-1} = \mathrm{Ro_S} \times F_\mathrm{S}$ for $F_\mathrm{S} = U_\mathrm{S}/c$ the source Froude number. Further discussion of model results in an oceanographic context is given within.

1.2 Coastal fronts

Coastal or boundary currents are an integral part of global ocean circulation. For example, currents may respond to external forcing or intrinsic instability by expelling vortex filaments or larger eddies into the ocean, with implications for the mixing of coastal and ocean waters; and currents driven by outflows are important for the transport of fresh water, pollutants and land-derived nutrients. Theoretical studies of coastal currents often employ idealised models in which the current and the upper ocean have uniform PV, a simplification that allows the dynamics to be understood by following the evolution of the PV front separating the ocean from the current. Stern and Pratt [1985] use this model to study the nonlinear evolution of a coastal front in a non-rotating environment, and Pratt and Stern [1986] develop a general QG model for a PV front. There is also much interest in the behaviour of 'free' fronts, i.e. those that are far from the coast, which can

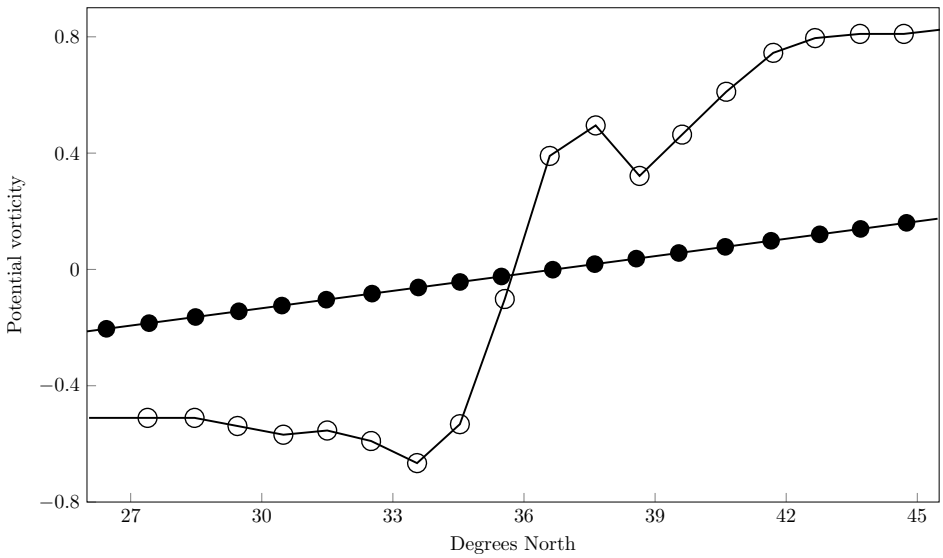

Figure 1.2: A meridional section of the upper-layer QG PV (open circles) and planetary vorticity (closed circles) within the Kuroshio Extension (150°E, August 2005) showing that the centre line of the current can be modelled as a PV jump. From Sasaki and Schneider [2011a].

be used to model Western boundary currents such as the Gulf Stream or the Kuroshio Extension (see figure 1.2) [Pratt et al., 1991, Cushman-Roisin et al., 1993, Sasaki and Schneider, 2011a, Tracey et al., 2012].

§4 considers the propagation of unforced long waves on a coastal front using a $1\frac{1}{2}$-layer, QG model introduced by Pratt and Stern [1986]. Although Pratt and Stern developed the model in a general form, their specific calculations are mostly concerned with free fronts in which the only wave is the Rossby wave. At leading order in the long-wave expansion, waves on a free front are stationary. At next order, the curvature of the front obeys the modified Korteweg–de Vries (KdV) equation [Pratt, 1988, Nycander et al., 1993]. The picture is dramatically different in the presence of a coastal boundary, and the purpose of this chapter is to provide an initial exploration of the regime in which the front is sufficiently close to the boundary to be influenced by two coastal effects; namely Kelvin wave-driven flow, and flow due to image vorticity. The combination of the two coastal effects and the Rossby wave leads to a rich set of dynamics, with the behaviour of the front depending strongly on the relative strengths of the three mechanisms. When first-order dispersive effects are included in the model, the governing equation belongs to a class of 'weakly-dispersive' equations and is somewhat similar to the modified KdV. We analyse the Riemann initial-value problem for this equation using 'dispersive shock-fitting' [El, 2005] and show that the dispersive long-wave theory captures

the quantitative behaviour of the full QG system extremely well.

1.3 Continental shelf waves

As well as being of interest in its own right, the coastal front model used in §4 can be extended to include a continental shelf (which is modelled as a constant-height step of variable width). In §5 we use this model to study the hydraulic control of coastal-trapped waves (CTWs) generated by variations in shelf width. (CTWs are vorticity waves that arise when columns of fluid are forced across isobaths, either by upper-layer Ekman transport or by the interaction of a mean current with an alongshore change in bathymetry.) CTWs are ubiquitous in the worlds oceans and play an important role in coastal upwelling. They are very long-lived, and can communicate the ocean's response to localised events over hundreds to thousands of kilometres. Linear CTWs in a continuously stratified ocean are governed by a form of the vorticity equation in which the non-dimensional parameter is the slope Burger number,

$$S = \left(\frac{N_0 H}{fL}\right)^2, \tag{1.1}$$

where $N_0 = (-g\rho_0^{-1}\rho'(z))^{1/2}$ is the buoyancy frequency, ρ_0 is a reference density and $\rho(z)$ is the (small) deviation from this in the vertical co-ordinate. H and L are representative depth and cross-shelf length scales respectively, and f is the Coriolis frequency. The slope Burger number illustrates the relative importance of stratification and the continental shelf. For large S, the shelf-width scale L is small compared to the Rossby radius of deformation $L_\mathrm{R} = c/f$ (where here $c = N_0 H$ is the internal gravity-wave speed in a continuously stratified fluid), and CTWs behave much like Kelvin waves (i.e. they ignore the shelf and propagate as if along a vertical wall). Alternatively when $S \ll 1$ stratification is not important and CTWs are barotropic topographic Rossby waves, often called continental shelf waves (CSWs). CTWs can therefore be thought of as a hybrid between internal Kelvin waves and topographic Rossby waves [Brink, 1991]. §5 is concerned with CSWs, which are known to occur off the coast of Scotland, along the Iceland-Faroe ridge, and on the Amundsen Sea shelf [Gordon and Huthnance, 1987, Miller et al., 1996, Wåhlin et al., 2016].

1.3.1 Hydraulic control of CTWs

CTWs always propagate to the right in the Northern hemisphere (the same direction as Kelvin wave flow), and can become arrested if the mean flow

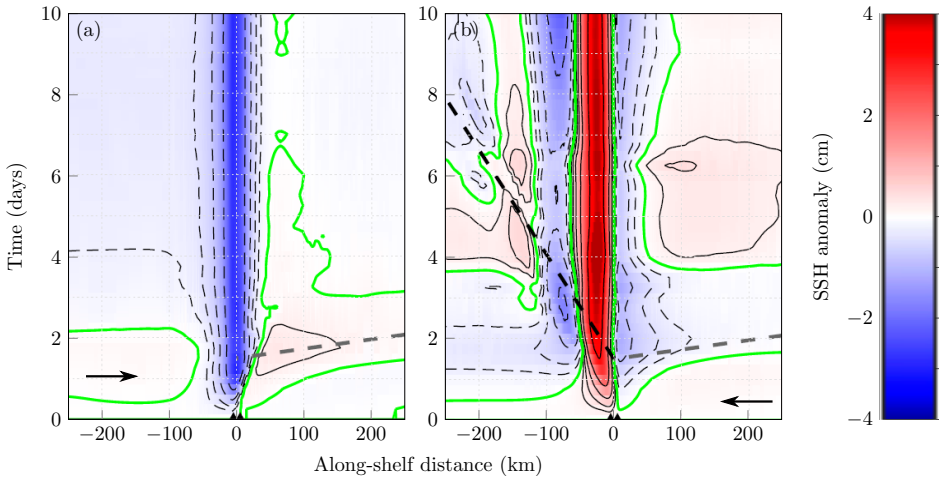

Figure 1.3: Hovmöller diagram showing sea-surface height (SSH) anomaly in an along-shore slice taken at the centre of the valley. The anomaly is defined relative to the far-field. The wind direction is marked by the thick black arrows and drives flow (a) in the direction of CTW propagation, and (b) counter to CTW propagation. Grey dashed lines show mode-1 CTW phase speed, and the black dashed line in (b) is the mean speed of the background flow. Triangles mark the edge of the valley. Adapted from Zhang and Lentz [2017].

is to the left. Zhang and Lentz [2017] use numerical simulations representative of the Hudson shelf valley to illustrate the asymmetric response of topographically-generated CTWs to the direction of the background flow. The Hovmöller diagram in figure 1.3 (adapted from figure 11 of Zhang and Lentz [2017]) shows an alongshore slice of the sea-surface height at the valley centre. For either direction of background flow, a mode-1 CTW (defined as the lowest-frequency solution to the relevant eigenvalue equation, (16) in Zhang and Lentz [2017]) propagates away from the valley (grey dashed line in (a) and (b)), while a train of standing lee waves develops on the left of the valley when the background flow opposes CTW propagation, and spreads at approximately the mean speed of the background current (black dashed line in (b)). Zhang and Lentz [2017] show that the characteristics of the lee waves are consistent with CTWs that have phase speed equal and opposite to the background flow, and thus they are arrested CTWs. The mode-1 wave is not arrested because its phase speed is much greater than the mean speed of the background flow. Martell and Allen [1979] identify the same response in a simpler barotropic model, and additionally demonstrate that the standing lee waves are a dispersive feature which do not occur in the long-wave limit.

As noted by Zhang and Lentz [2017], the combination of a wave that propagates away from an obstacle against the background flow and

standing waves on the other side is suggestive of hydraulic control, whereby geometric constrictions force a transition from subcritical to supercritical flow [Gill, 1977, Johnson and Clarke, 2001, Pratt and Whitehead, 2008]. Gill and Schumann [1979] and Dale and Barth [2001] study the hydraulic control of coastal flows using a model where each layer has uniform PV. This model therefore does not have Rossby waves, and the controlling mode is the internal Kelvin wave ($S \gg 1$). In contrast, Haynes et al. [1993] study controlled barotropic flow ($S = 0$) in a stepped channel with piecewise-uniform PV and thus a single Rossby mode. They show that two different types of control are possible: one where the flow is controlled at the maximum perturbation in step width, as for Kelvin waves, and one where the flow transitions from one supercritical branch of the solution to another via a control point at the edge of the perturbation. Johnson and Clarke [1999] extend this model to include first-order dispersive effects, which enables them to specify the location of the jump between branches. Chapter 5 studies the hydraulic control of CSWs and the corresponding lee waves, and thus is a coastal extension of the rigid-lid, channel model used by Haynes et al. [1993].

1.4 Vortical and Kelvin-wave flow

All of the models developed in this thesis focus on the dynamical behaviour of a coastal current with anomalous vorticity in a rotating co-ordinate system. Thus the flux and PV anomaly of the current, denoted Q_0 and Π_0 respectively, are key parameters in the analysis. In the QG limit Q_0 has units of area flux (Q_0 multiplied by the vertical scale gives the volume flux) and Π_0 has units of vorticity, so the vortex length $L_\mathrm{V} = \sqrt{(Q_0/|\Pi_0|)}$ emerges as a natural scale for the problem. In two-dimensional rigid-lid flow, Johnson and McDonald [2006] show that a vortical current against a vertical wall has width L_V, with the direction of flow determined by $\mathrm{sign}\,(\Pi_0)$. For systems where the Rossby radius of deformation is finite, JSM show that the parameter $a = L_\mathrm{R}/L_\mathrm{V}$ provides a useful means of interpreting the behaviour of such currents ($L_\mathrm{R} = (g'H)^{1/2}/f$ now reverting to the definition for a layered model). Vortical effects dominate when a is large, with the limit $a \to \infty$ recovering the two-dimensional flow of Johnson and McDonald [2006]. For smaller values of a vortical effects are relatively weaker and the response is instead dominated by the zero-PVa component, which we will call the 'Kelvin-wave driven flow' or, in §5, the 'background current'. In the QG limit the parameter a can be understood either as the ratio of the Kelvin-wave decay scale L_R to the width of the vortical

current L_{V}, or equivalently as the ratio of the vortical speed Q_0/L_{V} to the Kelvin-wave speed Q_0/L_{R}.

To estimate a for a coastal current in the real ocean we may take $L_{\mathrm{R}} = O(1 - 10\mathrm{km})$ as a typical range of values. The vorticity length L_{V} is less well-studied but may be estimated as follows. Assuming that the ocean is stagnant outside the coastal current, we may scale the vorticity within the current as the coastal velocity divided by the current width, that is we set $|\Pi_0| = u_{\mathrm{w}}/w$ for u_{w} the velocity at the coast. Further, we may scale w with L_{R} so that $a^2 = L_{\mathrm{R}}u_{\mathrm{w}}/Q_0$. Away from any source, $u_{\mathrm{w}} = O(0.1\mathrm{m\,s^{-1}})$ is reasonable while Q_0 varies between currents, say over the range $O(10 - 1000\mathrm{m^2/s})$, assuming an upper-layer depth of $O(10\mathrm{m})$ [Horner-Devine et al., 2015]. This gives $a^2 = O(0.1 - 100)$ so that the full range of behaviours shown below, including both Kelvin wave-dominated and vorticity-dominated flows, is reasonable in the real ocean.

In §2 we show that, for finite Rossby number, the Kelvin wave propagates ahead of the vortical outflow, leaving behind a steady geostrophic current which displaces the interface and establishes the coastal boundary condition for all time. In the QG model employed in §3 the Kelvin wave travels at infinite speed relative to the outflow, and is instead represented by a coastal boundary condition where the interface is displaced everywhere downstream of the source at $t = 0^+$ [Hermann et al., 1989]. In §§4-5 there is no source and the coastal boundary condition is applied everywhere. In this setting the boundary condition can be interpreted as the signal of a quickly-propagating mode such as the Kelvin wave, or simply as the zero-PVa component of the current which, depending on the direction of the flow, either depresses or raises the interface at the coast.

1.5 Background on the shallow-water model

The models used in this thesis can all be derived from the shallow-water equations, in which the continuously stratified ocean is represented by a (usually small) number of vertically-stacked layers, each with homogeneous density. As such we will briefly present some important properties of the shallow-water model, following chapter 3 of Vallis [2017].

In chapter 5 the model ocean consists of a single layer, with density ρ_0 and a free surface at $z = \eta(x, y, t)$. Taking the shallow-water (small aspect ratio) limit of the rotating Euler equations reduces the vertical momentum equation to hydrostatic balance. Integrating with respect to z and applying

the boundary condition that the pressure p vanishes at the free surface gives

$$p(x, y, z, t) = \rho_0 g(\eta(x, y, t) - z). \tag{1.2}$$

Thus horizontal pressure gradients are proportional to the free-surface gradient $\nabla\eta$ and consequently horizontal velocities are independent of z (∇p is independent of z). An important corollary of this is that the relative height of particles within a column of fluid is materially conserved: stretching or squashing is uniform throughout the water column. Note that in chapter 5 we write η as the sum of a mean value H and a small deviation (here denoted $h(x, y, t)$) in order to apply quasi-geostrophic theory.

In chapters 2-4 we use the 'reduced-gravity' shallow-water equations, in which the ocean consists of a thin upper layer of density ρ_1 lying above an infinitely-deep inactive layer with density $\rho_0 > \rho_1$. The upper layer represents the top few hundred metres of the ocean, and the lower-layer the stagnant abyss. The pressure in the lower layer, p_1, is given by the weight of the water above it:

$$p_1(x, y, z, t) = \rho_1 g(\eta - h) + \rho_0 g(h - z), \tag{1.3}$$

where here $z = h(x, y, t)$ is the interface between the two layers. Since there is no motion in the lower layer, $\nabla p_1 = 0$ and thus

$$g\nabla\eta + g'\nabla h = \text{ constant}, \tag{1.4}$$

where we have introduced the reduced gravity $g' = g(\rho_0 - \rho_1)/\rho_1$. The dynamics of the active layer are the same as those of the single layer in §5, up to replacing g with g'. Assuming that variations in density are small, $g' \ll g$ and thus $\nabla\eta \ll \nabla h$. We may therefore further simplify the model by placing a rigid lid at $z = 0$, and thus in this thesis we refer to h as the depth of the upper layer. The rigid-lid approximation is supported by observations: the vertical displacement of isopycnals in the upper ocean is much larger than variations in the mean height of the ocean surface (tens of meters versus a few centimetres).

Chapter 2

A semi-geostrophic model for coastal outflows

In this chapter, we model a coastal outflow using the long-wave, reduced-gravity, shallow-water equations (the semi-geostrophic equations). The river water is taken to have the same density as a finite-depth upper layer of oceanic fluid, and the two fluids have different, uniform, potential vorticities. The model is thus an extension of Johnson et al. [2017] (JSM hereafter) to order-one Rossby number. We show that, as in JSM, the dynamics are determined by the sign of the PVa and the strength of the outflow, and are strongly correlated with the value of a single dimensionless parameter (a) which expresses the ratio of the speed of the flow driven by the Kelvin wave to that driven by image vorticity. We show that for moderate values of the Rossby number the behaviour of the outflow depends on the magnitude of both effects independently, unlike in the QG limit where the plume behaviour is determined by their ratio alone.

In §2.1 we derive the semi-geostrophic system from the rotating shallow-water equations, and show that the assumption of piecewise uniform PV reduces the problem to a pair of nonlinear partial differential equations in flux form. A similar set of equations has previously been used to study coastal currents with uniform PV [Stern, 1980, Stern et al., 1982, Kubokawa and Hanawa, 1984a, Stern and Helfrich, 2002], and is amenable to analysis due to the existence of similarity solutions in unforced regions of the domain (i.e. away from the source, which here is a novel addition to the semi-

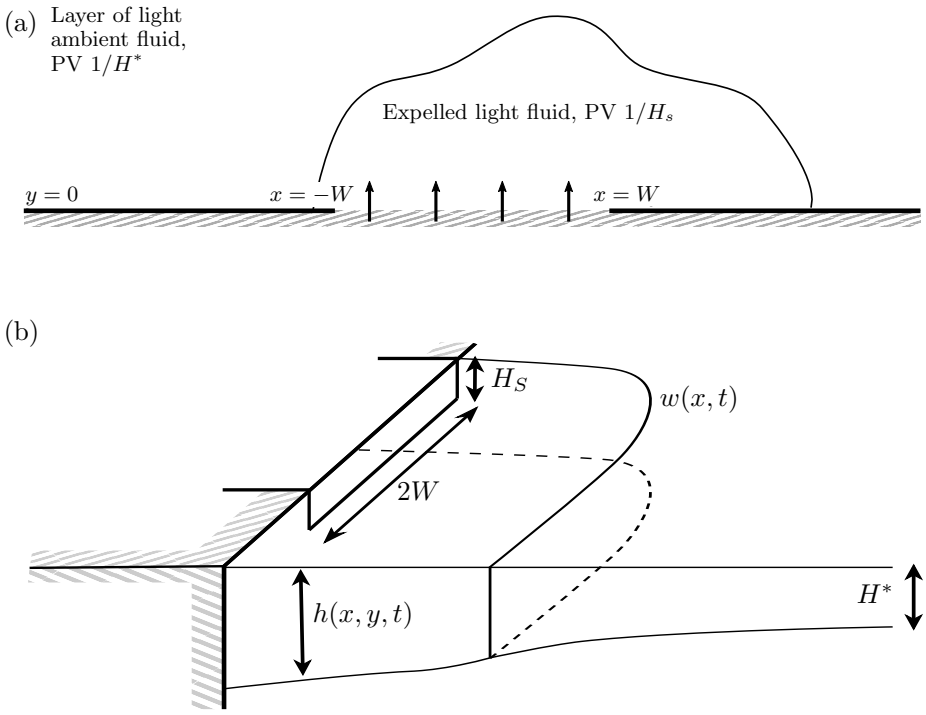

Figure 2.1: Fluid is expelled from a coastal source of depth H_s located at $|x| < W$, $y = 0$. The oceanic fluid in $y > 0$ initially consists of a lighter layer (with the same density as the expelled fluid) of dimensional depth H^* lying over a deep, denser, inactive layer. (a) Plan view, (b) side view with $y = w(x,t)$ denoting the boundary of the expelled fluid. Variables are dimensional.

geostrophic model). When the outflow has positive PVa, all fluid turns to the right and the plume always becomes steady. This allows us to describe the plume behaviour analytically by matching steady solutions in the source region with similarity solutions downstream. §§2.2-2.3 derives theoretical results for outflows with positive and negative PVa respectively and shows that they agree excellently with numerical simulations of the semi-geostrophic system, while §2.4 briefly compares the main results to previous theoretical and experimental studies.

2.1 Model and governing equations

Consider a layer of buoyant fluid with dimensional depth H^* lying above an infinitely deep, inactive layer, with the whole system rotating about a vertical axis Oz at constant angular speed $f/2 > 0$, where $Oxyz$ are Cartesian axes fixed in the fluid. The fluid lies in $y > 0$, with the coast at $y = 0$ a solid vertical boundary. At time $t = 0$, a coastal source lying

between $-W < x < W$ is switched on. The fluid expelled by the source is of the same density as the active layer, and has a different PV. The active layer is taken to be sufficiently shallow to be governed by the reduced-gravity rotating shallow-water equations, which in non-dimensional form are:

$$\frac{\partial u}{\partial t} + u\frac{\partial u}{\partial x} + v\frac{\partial u}{\partial y} - v = -\frac{\partial h}{\partial x}, \tag{2.1}$$

$$\left(\frac{L_{\mathrm{R}}}{W}\right)^2 \left(\frac{\partial v}{\partial t} + u\frac{\partial v}{\partial x} + v\frac{\partial v}{\partial y}\right) + u = -\frac{\partial h}{\partial y}, \tag{2.2}$$

$$\frac{\partial h}{\partial t} + \frac{\partial}{\partial x}(uh) + \frac{\partial}{\partial y}(vh) = 0, \tag{2.3}$$

where h is the depth of the active layer, and u and v are the along-shore and off-shore velocities respectively. Here x has been non-dimensionalised with W (so that the source lies in $|x| < 1$), y with the Rossby radius for the source fluid $L_{\mathrm{R}} = \sqrt{g'H_s}/f$, velocities u and v with $\sqrt{g'H_s}$ and $\sqrt{g'H_s}(L_{\mathrm{R}}/W)$ respectively, h with H_s (the source depth) and t with the advective time-scale $W/\sqrt{g'H_s}$, where g' is the reduced gravity for the upper layer. Within the upper layer horizontal velocities are independent of z and the boundary between the expelled fluid and the upper ocean layer remains vertical. A schematic of this set-up is shown in figure 2.1.

Taking the limit $L_{\mathrm{R}}/W = K^{-1} \to 0$ gives the semi-geostrophic or long-wave equations, and requires that the flow is slowly varying in the x direction, or that the river mouth is wide relative to the Rossby radius (recall from §1.1 that the Kelvin number K is large for outflows that are strongly-affected by rotation [Garvine, 1995]). The semi-geostrophic equations can in fact still be a valid asymptotic description of the full shallow-water system if variations in x are fast (for example, in the region of a shock) provided the off-shore velocity $v \ll u$ [Kubokawa and Hanawa, 1984b]. The long-wave assumption requires further justification in the source region, especially at early times when v and u are of the same order, and the x and y scales are similar. Strong support for the use of this scaling comes from JSM, where they find excellent agreement between their long-wave theory and contour-dynamic simulations of the full QG problem, even in simulations where fluid is expelled from a point source (their figures 11-13). Discrepancies do exist in the source region, but it appears that the long-wave scaling does not affect the qualitative behaviour of the outflow, including the strength of the upstream propagation in outflows with negative PVa. Thus while the present model may have applications to outflows of any width, it is formally only valid for those where $K \gg 1$ and thus, as shown in Huq [2009], bulges are not expected to form at the river

mouth. In the coastal oceans the deformation radius is on the order of a few kilometres, so that some rivers that fall into the $K \gg 1$ regime are the Delaware [Münchow and Garvine, 1993b] and the Hudson [Chant et al., 2008], in both of which $W \approx 20$km. For example, Münchow and Garvine [1993b] employ conductivity-temperature-depth casts over a period of three months in 1989 to estimate L_R at the mouth of the Delaware as 6.2km, which gives $K = 3.2$. Further estimates of K for different plumes are given in table 1 of Garvine [1995] and figure 10 of Huq [2009].

A standard manipulation of equations (2.1) - (2.3) shows that the PV

$$q = \frac{1 - \partial u/\partial y + (L_\mathrm{R}/W)^2 \partial v/\partial x}{h} \tag{2.4}$$

is conserved by fluid parcels [Stern, 1980]. Taking the limit $L_\mathrm{R}/W \to 0$ and substituting (2.2) gives the field equation for h,

$$\frac{\partial^2 h}{\partial y^2} - qh + 1 = 0. \tag{2.5}$$

The ambient outer layer begins at rest with non-dimensional depth H and so has PV $q_\mathrm{out} = 1/H$, while the non-dimensional PV of the expelled fluid is $q_\mathrm{in} = 1$. Thus $H > 1$ corresponds to positive PVa, and $H < 1$ to negative PVa. In the scenario described here, where flow starts at rest and the source has uniform depth, the choice of uniform PV would seem quite natural. This restriction on the river mouth geometry is not necessary for the outflow to have uniform PV. One could instead consider flow from a wide, deep upstream reservoir as in Gill [1977] where H_s is the potential vorticity depth of the river water. In either case, the use of piecewise-constant PV is a necessary simplification required to solve (2.5) and make analytic progress. Models with uniform PV have been used to provide a theoretical framework for understanding large-scale ocean flows [Stern, 1980, Kubokawa, 1991, Helfrich et al., 1999, for example] and this simplification has also been used successfully to describe laboratory experiments that simulate coastal outflows [Thomas and Linden, 2007, Gregorio et al., 2011]. The Rossby number of the flow can be defined, following Clarke and Johnson [1999], as

$$\mathrm{Ro} = \left| \frac{H^* - H_s}{H_s} \right| = |H - 1|, \tag{2.6}$$

that is, the ratio of the PVa and background PV. The limit $H \to 1$ thus recovers the quasi-geostrophic flow of JSM.

Provided it does not overturn, the boundary of the expelled fluid can be described as a single-valued function $y = w(x, t)$ and the field equation (2.5) can be solved separately in the river water and the ambient to give h

(and hence u and, by (2.1), v), in terms of y, w and $U = u(x, w, t)$. Solving (2.5) gives

$$h = \begin{cases} H + \sqrt{H}U\mathrm{e}^{(w-y)/\sqrt{H}} & y > w(x,t) \\ 1 + \left(H - 1 + \sqrt{H}U\right)\cosh(w-y) + U\sinh(w-y) & 0 < y < w(x,t), \end{cases} \tag{2.7}$$

where the following conditions have been applied:

$$\begin{aligned} h \to H \text{ as } y \to \infty, \\ u = U \text{ at } y = w, \\ h \text{ is continuous at } y = w. \end{aligned} \tag{2.8}$$

That the solution depends on x parametrically through U and w is a common feature of long-wave models. This prohibits wave-breaking, and requires that the expelled fluid remain contiguous. This is at odds with, for example, the shallow-water numerical results of Helfrich [2006] (their figure 10) which shows that wave-breaking occurs during the geostrophic adjustment of buoyant fluid against a vertical coast. However, differences between theory and numerical results are restricted to the area around the current boundary and the long-wave model still provides a useful guide to the behaviour of the full shallow-water system.

Other quantities that appear in the calculations below are the layer depths at the wall and the current edge, and the fluid velocity at the wall. These are given by:

$$h_\mathrm{w} = h(x,0,t) = 1 + (H - 1 + \sqrt{H}U)\cosh(w) + U\sinh(w), \tag{2.9}$$

$$h_\mathrm{e} = h(x,w,t) = H + \sqrt{H}U, \tag{2.10}$$

$$u_\mathrm{w} = u(x,0,t) = U\cosh(w) + (H + \sqrt{H}U - 1)\sinh(w). \tag{2.11}$$

The mass flux of oceanic fluid at a station x is given by

$$\int_w^\infty uh \, \mathrm{d}y = \frac{h^2}{2}\bigg|_\infty^w = \frac{h_\mathrm{e}^2}{2} - \frac{H^2}{2}. \tag{2.12}$$

These expressions are used in (2.1)-(2.3) to write the governing equations as a pair of first-order partial-differential equations (PDEs) in terms of $U(x,t)$ and $w(x,t)$, which are amenable to analysis and a simpler numerical treatment than the original system. In deriving these PDEs below we also make use of the kinematic boundary condition

$$v = \frac{\partial w}{\partial t} + U\frac{\partial w}{\partial x} \quad \text{at } y = w, \tag{2.13}$$

and the relationship

$$\left.\frac{\partial \Phi}{\partial \xi}\right|_{y=w} = \frac{\partial}{\partial \xi}\Phi(y=w) - \left.\frac{\partial \Phi}{\partial y}\right|_{y=w}\frac{\partial w}{\partial \xi}, \tag{2.14}$$

for $\xi = x$ or t and $\Phi = h$ or u.

Stern [1980] notes that the y-derivative of the alongshore momentum equation (2.1) vanishes and thus it is sufficient to solve (2.1) at one y-value only, which we choose to be the current edge. Evaluating (2.1) at $y = w$ gives

$$\frac{\partial U}{\partial t} + U\frac{\partial U}{\partial x} + \sqrt{H}\frac{\partial U}{\partial x} - \frac{\partial w}{\partial t} = 0. \tag{2.15}$$

The system is closed by an integrated form of mass conservation (2.3), which is

$$\frac{\partial}{\partial t}\int_0^w h \, \mathrm{d}y + H\left(\frac{\partial U}{\partial t} - \frac{\partial w}{\partial t}\right) + h_{\mathrm{w}}\frac{\partial h_{\mathrm{w}}}{\partial x} = Q'(x), \tag{2.16}$$

for

$$\int_0^w h \, \mathrm{d}y = (H-1)\sinh(w) + w + U\left(-1 + \cosh(w) + \sqrt{H}\sinh(w)\right). \tag{2.17}$$

Here, $Q(x)$ is a monotonic-increasing function that gives the (steady) cumulative volume flux from the river mouth for $t > 0$ through

$$\int_{-1}^{x} vh|_{y=0} \, \mathrm{d}x' = Q(x) \tag{2.18}$$

so that the total mass flux from the source is $Q_0 = Q(1)$ which, along with H, is a key physical parameter for the flow. Thus the coastal boundary condition is applied by specifying a mass outflow profile $Q(x)$, and extending this function to take values zero and Q_0 in $x < -1$ and $x > 1$ respectively. The long-term evolution of the current away from the source region is found below to depend on $Q(x)$ only through the total mass flux Q_0, and so for simplicity all examples presented here use the linear profile $Q(x) = (Q_0/2)(x+1)$ in $|x| < 1$. The theory below classifies the qualitative behaviour of the outflow in terms of the two parameters Q_0 and H, and so applies to any steady volume flux profile $Q(x)$, including those resulting from a critically controlled outflow. Results presented here can also be easily extended to unsteady outflows, and an analysis of such changes is explored in more detail for the quasi-geostrophic limit in Southwick et al. [2017].

2.1.1 Vortical and Kelvin-wave driven flow

The two principal mechanisms that drive the outflow are the Kelvin wave and image vorticity. In the QG model employed by JSM and elsewhere in

this thesis, the relative strengths of the two mechanisms can be controlled through the parameter $a = L_{\mathrm{R}}/L_{\mathrm{V}}$, which can be understood either as the ratio of the Rossby radius to the vortex length or as the ratio of the vortex speed to the Kelvin-wave speed (see 1.4). JSM show that solutions to the QG model can be fully characterised by the value of a and the sign of the PVa, and one of the main goals of this chapter is to assess to what extent a can be used to categorise outflows with finite Ro. It is expected, and shown below, that the results here reduce to those of JSM in the limit $\mathrm{Ro} \to 0$ and $Q_0 \to 0$, with $a \sim \sqrt{(\mathrm{Ro}/Q_0)}$ fixed. However the speed and length-scale ratios are not equivalent in the semi-geostrophic model and so, finding the interpretation in terms of speed to be more instructive, for this chapter only we set $a = |u_{\mathrm{V}}|/u_{\mathrm{KW}} \neq L_{\mathrm{R}}/L_{\mathrm{V}}$, with these speeds discussed in more detail below.

First consider the Kelvin-wave flow, which propagates faster than the river water and thus transports both river and oceanic fluid [Helfrich et al., 1999, Helfrich, 2006]. In the zero-PVa problem (that is, with $H = 1$) image vorticity is absent and flow is due to the Kelvin wave alone. In this case, the problem reduces to solving (2.1) at the wall,

$$\frac{\partial B}{\partial t} + (1 + B)\frac{\partial B}{\partial x} = Q'(x), \tag{2.19}$$

with B related to the layer depth by

$$h = 1 + B(x, t)\mathrm{e}^{-y}. \tag{2.20}$$

Equation (2.19) is the forced Hopf equation, which can be solved explicitly using the method of characteristics, and gives rise to a current that expands offshore and spreads downstream at speed $u_{\mathrm{KW}} = -1 + \sqrt{(1 + 2Q_0)}$ at the wall. This is referred to hereafter as the Kelvin-wave flow. Non-trivial solutions of the homogeneous Hopf equation always develop shocks, which occur in the present problem in the oceanic (rather than river) water at the leading edge of the Kelvin-wave flow. These shocks are discussed in greater detail in §2.2.5.

The effect of image vorticity can be isolated by considering the limiting case of rotating fluid ejected into a non-rotating background, and it is shown in Johnson and McDonald [2006] that the velocity of the current at the wall is $u_{\mathrm{V}} = \pm\sqrt{(Q_0|H - 1|/H)}$ where the sign depends on the sign of the PVa. Thus, for positive PVa both the vortical and Kelvin-wave effects drive fluid downstream, and the dynamics are reinforcing, while for negative PVa the dynamics are opposing. The ratio between the two speeds is

$$a = \frac{|u_{\mathrm{V}}|}{u_{\mathrm{KW}}} = \frac{\sqrt{Q_0|H - 1|}}{-\sqrt{H} + \sqrt{H(1 + 2Q_0)}}. \tag{2.21}$$

Anticipating the importance of a in determining the behaviour of the flow, we will briefly outline some results from the quasi-geostrophic limit.

When $a < 1$, the Kelvin wave-driven flow is dominant: $|u_{\mathrm{V}}| < u_{\mathrm{KW}}$ and $L_{\mathrm{R}} < L_{\mathrm{V}}$. For positive PVa, vortical overturning is weak at the nose of the river water and the outflow boundary joins smoothly to the coast. For negative PVa, the weak vortical flow is not sufficient to counteract the Kelvin wave, and the solution expands indefinitely away from the coast, with fluid spreading up and downstream. When $a > 1$, vorticity dynamics dominate the outflow: $|u_{\mathrm{V}}| > u_{\mathrm{KW}}$ and $L_{\mathrm{R}} > L_{\mathrm{V}}$. For positive PVa, vortex turning affects fluid closer to the wall, causing the boundary of the current to overturn and a shock to form. As a increases further, this happens over a shorter and shorter scale until, for $a = a_m \approx 1.868$, the vortical current manages to adjust to the far-field condition within the expelled fluid and there is no disturbance in the oceanic fluid $y > w$. In this case, the solution downstream is a current of constant width. For negative PVa, the relatively stronger vortical flow balances the Kelvin wave and the flow is steady in the source region.

Note that the choice of L_{R} for horizontal length scales ensures that the length over which the Kelvin wave decays is $O(1)$, while vortical currents can be of arbitrary width. On the other hand, JSM scale horizontal lengths on L_{V}, thus keeping the vortical current width at $O(1)$ and allowing the Kelvin wave decay scale to be arbitrarily small as $a \to 0$.

2.1.2 Constants of motion

Benjamin and Lighthill [1954] describe trains of steadily-translating long gravity waves using three constants of motion: volume flux, alongshore momentum flux, and total energy. The volume flux of river water is simply the parameter Q_0, and similar expressions for the momentum flux and total energy can also be derived.

Multiplying the along-shore momentum equation (2.1) by h, the mass conservation equation (2.3) by u, taking the sum of these and integrating from $y = 0$ to $y = \infty$ gives

$$\frac{\partial}{\partial t}\int_0^\infty uh \,\mathrm{d}y + \frac{\partial}{\partial x}\int_0^\infty \left(hu^2 + \frac{h^2}{2}\right) \,\mathrm{d}y - u_{\mathrm{w}}h_{\mathrm{w}}v_{\mathrm{w}} = \int_0^\infty vh \,\mathrm{d}y. \quad (2.22)$$

(Note that u and v decay exponentially as $y \to \infty$, so that the integrals in (2.22) and below are bounded.) The right hand side of (2.22) can be written in flux form by multiplying (2.3) by y and integrating:

$$\int_0^\infty vh \,\mathrm{d}y = \frac{\partial}{\partial t}\int_0^\infty yh \,\mathrm{d}y + \frac{\partial}{\partial x}\int_0^\infty yuh \,\mathrm{d}y \quad (2.23)$$

so that (2.22) becomes

$$\frac{\partial I}{\partial t} + \frac{\partial S}{\partial x} = u_{\mathrm{w}} h_{\mathrm{w}} v_{\mathrm{w}}, \tag{2.24}$$

where

$$I = \int_0^\infty (u-y)h \, \mathrm{d}y, \qquad S = \int_0^\infty \left(hu(u-y) + \frac{h^2}{2} \right) \, \mathrm{d}y \tag{2.25}$$

are the along-wall impulse and the flow force respectively. The quantity $u_{\mathrm{w}} h_{\mathrm{w}} v_{\mathrm{w}}$ is the downstream momentum input at the wall, and vanishes away from the source region. The total downstream momentum added across the source in steady flow is thus

$$S_0 = \int_{-1}^{1} u_{\mathrm{w}} Q'(x) \, \mathrm{d}x = \int_0^{Q_0} u_{\mathrm{w}} \, \mathrm{d}Q, \tag{2.26}$$

giving a second constant of the motion. The momentum input term is discussed in greater deal for QG flow in Southwick et al. [2017], where its presence is shown to resolve the momentum imbalance paradox of Pichevin and Nof [1997].

In steady flow, (2.3) allows a volume-flux streamfunction ψ to be defined such that $vh = \psi_x$ and $uh = -\psi_y$. The along-shore momentum equation (2.1) can be integrated once in x to give

$$\frac{u^2}{2} - \psi + h = R. \tag{2.27}$$

Since the y-derivative of (2.1) vanishes R is constant throughout the domain, providing a third constant of motion for steady flow that can be found by evaluating (2.27) at the wall, where $\psi = Q$.

2.2 Outflows with positive PVa

2.2.1 Numerical results

Having now reduced the problem to two nonlinear PDEs (2.15) and (2.16) in x and t, solutions can be obtained numerically. Starting from the initial conditions $U = w = 0$, the equations are integrated away from $t = 0$ using the Lax-Wendroff method with a nonlinear smoothing filter [Engquist et al., 1989] to prevent overshoot in the region of a shock. To ensure that the numerical scheme explicitly preserves mass and momentum, the equations are solved in conservation form, i.e

$$\frac{\partial}{\partial t} \begin{pmatrix} \phi_1 \\ \phi_2 \end{pmatrix} + \frac{\partial}{\partial x} \begin{pmatrix} U^2/2 + \sqrt{H}U \\ h_{\mathrm{w}}^2/2 \end{pmatrix} = \begin{pmatrix} 0 \\ Q'(x) \end{pmatrix}, \tag{2.28}$$

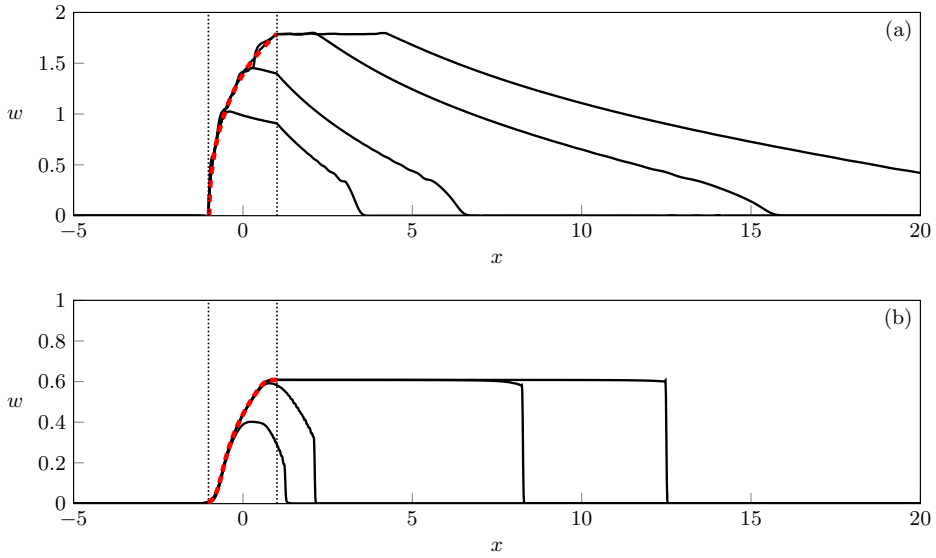

Figure 2.2: The off-shore extent of the expelled fluid, $y = w(x,t)$, for flows with positive PV anomaly. (a) $Q_0 = 1$, Ro $= 0.3$ and hence $a = 0.66$ (Kelvin-wave dominated flow) at $t = 5, 10, 25, 40$. (b) $Q_0 = 0.4$, Ro $= 1$ and $a = 1.31$ (vortically-dominated flow) at $t = 5, 10, 40, 60$. Vertical dotted lines mark the source region, and the dashed red curve is the steady profile w_{sp} computed in §2.2.2.

where

$$\phi_1 = U - w, \quad \phi_2 = \int_0^w h \, \mathrm{d}y + H(U - w). \tag{2.29}$$

This presents some difficulty, since the $\partial/\partial x$-terms cannot be written explicitly in terms of ϕ_1 and ϕ_2, and so U and w are extracted at each grid-point and each time step via Newton's method, using as an initial guess the values of the solution at the previous time-step. Applying homogenous Neumann boundary conditions at the upstream end of the spatial domain increases stability. Runs are conducted with grid spaces of $\Delta t = 0.01$ or 0.005, and $\Delta x \approx 0.03$ as increasing the resolution further made no noticeable difference.

Figure 2.2 shows numerically computed w for two different sets of parameters, with each subplot showing the solution at several times. Figure 2.3 shows w, U and contours of $h - H$ for a third set of parameters. In all plots, the source region is marked by vertical dotted lines, and theoretical results derived below are shown dashed and in red. From the two functions w and U, the depth and velocity profile at any point can be computed using (2.7). In all solutions with positive PVa, a steady current forms across the source region. The current width increases monotonically across the source and the fluid at the current edge has zero velocity, so the outer layer is undisturbed in regions where the flow is steady. Numerical results agree

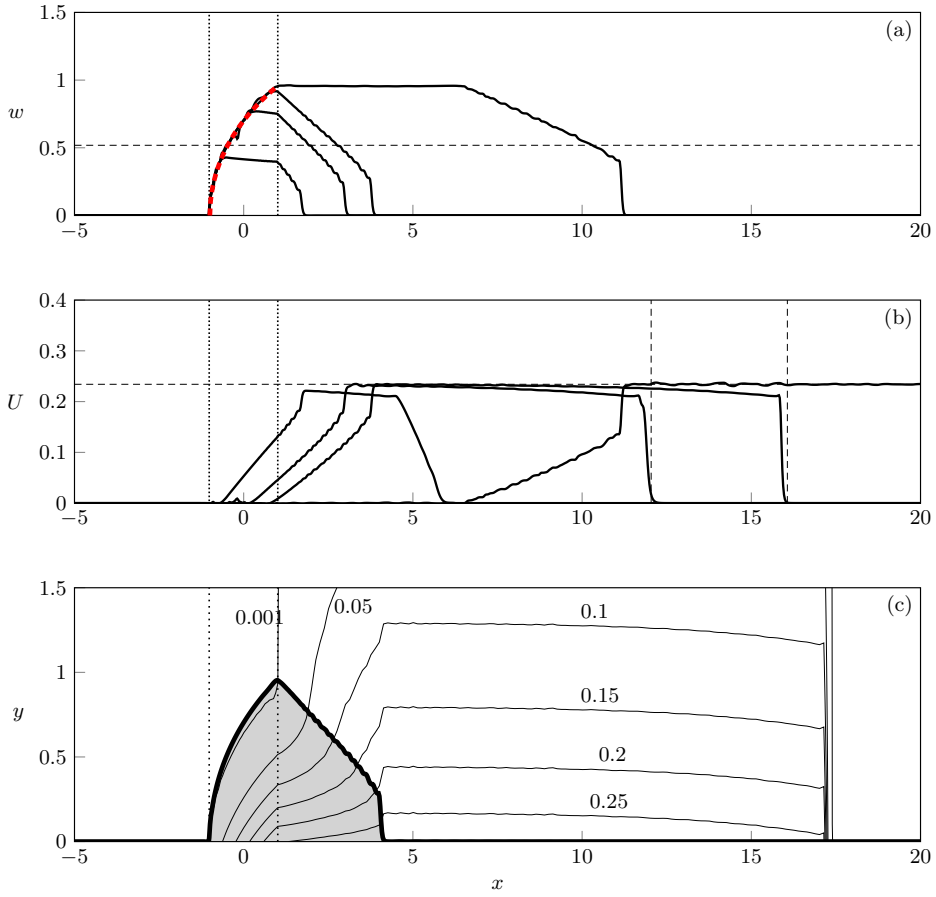

Figure 2.3: Outflow with positive PVa, $Q_0 = 0.4$, Ro $= 0.5$ and hence $a = 1.07$. (a) The current width w and (b) the edge velocity U are shown at times $t = 4, 9, 12, 40$. The red dashed curve in (a) gives the steady profile $w_{\rm sp}$, and thin dashed lines in (a) and (b) correspond to predictions from the theory of §§2.2.3-2.2.5. (c) Contours of $h - H$, perturbations to the depth of the upper layer at $t = 12$. The thick curve gives w at the same time, thus the shaded region is the extent of the expelled fluid.

excellently with the theory presented in §2.2.2 (red dashed curve). Once the steady solution reaches all the way across the source, a steady current of constant width propagates downstream.

Downstream of the steady region, the current narrows and the velocity around the edge increases according to a similarity solution discussed in §2.2.3. The parameters in figures 2.2-2.3 are chosen to illustrate each possible qualitative behaviour and, as in JSM, these correlate with the value of the speed ratio a. For small a, as in figure 2.2(a), the flow is dominated by the Kelvin wave and the downstream current joins smoothly to the wall. For larger a, as in figures 2.2(b) and 2.3(a), vorticity is stronger and the current terminates in a shock. The width of the shock increases monotonically, until it reaches a maximum value that is set by the flow

parameters. If a is large enough, and vortical effects are strongly dominant, this maximum value can be the same as the width of the steady current at the downstream edge of the source region, in which case there is no rarefaction and the solution after a finite time is a 'blunt-headed current' (c.f. Figure 2.2(b)).

In regions where $w = 0$, the governing equations are still valid but U is now to be interpreted as the velocity at the coast, with the layer depth decaying offshore as $U \exp(-y/\sqrt{H})$. At all times and for all parameters, a nonlinear Kelvin wave propagates ahead of the expelled fluid. That is, $U > 0$ in some region where $w = 0$. The effects of this are most clearly seen in the contour plot of figure 2.3(c) – the river water (shaded) has reached $x = 4$, but the wall depth is increased by 0.25 over the region $4 < x < 16$, an interfacial disturbance travelling in the oceanic fluid ahead of the river water. In the quasi-geostrophic limit, the Kelvin wave travels at infinite speed in the outer layer and so is not seen explicitly in the solutions – although it still induces a flow of finite velocity in the river water. The properties of the Kelvin wave are discussed in detail in §2.2.5.

2.2.2 Analysis across the source region

Since the PVa is positive, the image vorticity and the Kelvin wave both drive the flow downstream. System (2.15), (2.16) has two eigenvalues, λ_{R} and λ_{C}, with $\lambda_{\mathrm{R}} \leq \lambda_{\mathrm{C}}$ always (see appendix A for more details). Kubokawa and Hanawa [1984a] note that λ_{C} is a nonlinear coastal wave, and that λ_{R} is associated with disturbances at the current edge – across which the density jump from their model has been replaced by a PV jump in the present model.

For the initial conditions $w = U = 0$, $\lambda_{\mathrm{R}} = 0$ and $\lambda_{\mathrm{C}} = \sqrt{H}$. Thus, characteristics λ_{R} that start in $x < -1$ are unable to reach the source region. Further, it is impossible to satisfy $\lambda_{\mathrm{C}} = 0$ or $\lambda_{\mathrm{R}} = 0$ when $U > 0$ and $H > 1$ and so the flow is supercritical everywhere in $x > -1$, with no information able to propagate upstream. Since the characteristic speed λ_{R} vanishes at $x = -1$ this is the control point for the steady flow that forms across the source region. The flow matches smoothly to the undisturbed outer layer at $x = -1$, where $w = U = 0$.

Solving the steady versions of (2.15) and (2.16) gives

$$\begin{aligned} U &= c_1, \\ h_{\mathrm{w}} &= \sqrt{2Q(x) + c_2}, \end{aligned} \tag{2.30}$$

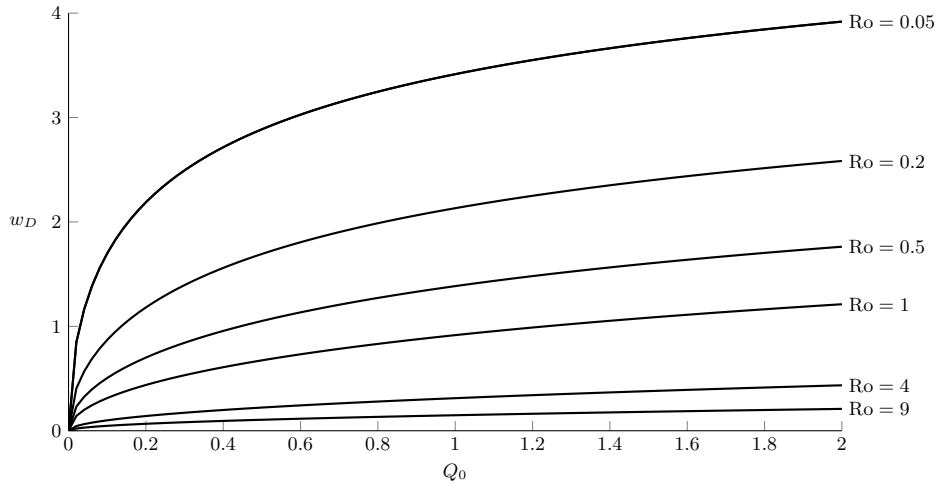

Figure 2.4: The width of the steady current w_D downstream of the source, as a function of the total mass flux Q_0, for various values of the Rossby number Ro.

where c_1 and c_2 are constants of integration determined by the requirement that U and h_w are continuous at $x = -1$ to be 0 and H^2 respectively. Downstream, the dimensional depth of the current at the wall is therefore

$$h^* = \sqrt{\frac{2Q^* f}{g'} + H^{*2}} \tag{2.31}$$

where Q^* and H^* are the (dimensional) mass flux and outer-layer depth respectively. The relationship (2.31) can be derived from a simple quasi-geostrophic scaling argument when $H = 0$ [Chant, 2011, p. 218].

Solving (2.9) for w provides the steady solution

$$w_\mathrm{sp}(Q) = \operatorname{acosh}\left(\frac{\sqrt{2Q + H^2} - 1}{H - 1}\right), \tag{2.32}$$

which is valid exactly when $H > 1$. The steady solution w_sp is shown as a dashed red curve in figure 2.2 and 2.3(a). Agreement with the numerical results is excellent in all cases. The steady current depends on x only parametrically through Q, and hence the downstream current width $w_\mathrm{D} = w_\mathrm{sp}(Q_0)$ does not depend on the specific form of the outflow velocity. In the quasi-geostrophic limit, $\mathrm{Ro} \to 0$ and $Q_0 \to 0$ with $a^2 = \mathrm{Ro}/Q_0$ fixed,

$$w_\mathrm{D} \sim \log\left(1 + 1/a^2 + \sqrt{1/a^4 + 2/a^2}\right) + O(\mathrm{Ro}) \qquad \text{as } \mathrm{Ro} \to 0, \tag{2.33}$$

as in (3.9) of JSM, up to the use of L_V as the characteristic length for y.

The downstream width of the steady solution w_D is shown as a function of Q_0 and H in figure 2.4. Since the steady solution always has $U = 0$, the river water completely adjusts to the upper layer depth over the vortex

scale L_V in the source region. Large Q_0 – which corresponds to small a and large L_V – thus gives rise to a wider current (growing logarithmically as $Q_0 \to \infty$), while large Ro gives small L_V and a narrow current as the vortical turning happens closer to the wall.

2.2.3 Downstream solution

Away from the source region the governing equations are unforced, and hence possess two Riemann invariants, i.e. there exist functions $\mathcal{R}_{C/R}(w, U)$ such that

$$\frac{\mathrm{d}}{\mathrm{d}t}\,\mathcal{R}_{C/R}(w,U) = 0 \qquad \text{on} \qquad \frac{\mathrm{d}x}{\mathrm{d}t} = \lambda_{C/R}. \tag{2.34}$$

Thus $\mathcal{R}_{C/R}$ are constant on each characteristic, with that constant determined by the values of w and U at the time when a given characteristic leaves the source region. For this system, the Riemann invariants cannot be found analytically and are obtained instead by solving the equivalent problem

$$\frac{\mathrm{d}U}{\mathrm{d}w} = \alpha_{C/R}(w,U) \qquad \text{on} \qquad \frac{\mathrm{d}x}{\mathrm{d}t} = \lambda_{C/R} \tag{2.35}$$

as in Helfrich [2006]. The functions $\alpha_{C/R}$ are found by diagonalising the system (2.15)-(2.16), and are given explicitly in appendix A. The initial conditions for integrating (2.35) along a particular characteristic are given by the values of w and U at the point when that characteristic leaves the source region. In particular, once the steady solution reaches the downstream edge of the source region, the values of w and U are fixed and so all integrations start with the same conditions – the Riemann invariants are uniform.

The uniformity of one Riemann invariant is used in Stern and Helfrich [2002] to build similarity solutions $U(w)$ and describe the propagation of a coastal current with negative PVa. The same approach is applied here, whilst noting that uniform Riemann invariants only occur once the steady solution has been completely set up, and so the similarity solution is only valid after a finite time.

Immediately downstream of $x = 1$ both Riemann invariants are uniform. Here, there are two universal relationships $\mathcal{R}_{C/R}(w, U) = m_{C/R}$ and so the only continuous solution has $w = w_D$ and $U = 0$ (visible at late times in figures 2.2 and 2.3). The region of two uniform invariants is led by the slower characteristic λ_R, and so the speed at which the constant-width current spreads can be calculated by setting $w = w_D$ and $U = 0$ in λ_R. Downstream of this constant-width region, only the λ_C characteristic is determined by the steady values of w and U and so only the $\mathcal{R}_C$ invariant

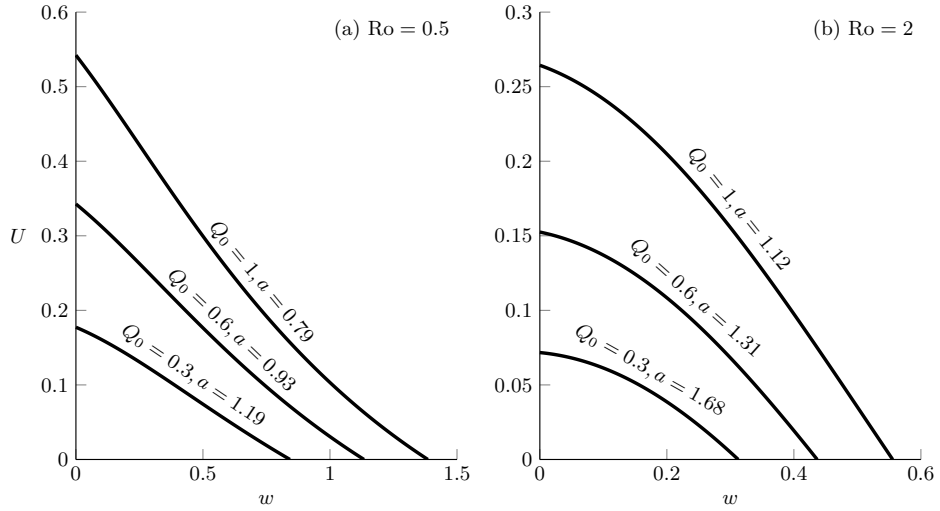

Figure 2.5: The velocity U at the edge of the expelled fluid, as a function of the width w, in the unsteady downstream rarefactions that lead the outflow. (a) Ro = 0.5, (b) Ro = 2. These relationships are valid once the steady solution has been been set up across the source region.

is uniform. The similarity solution $U(w)$ can thus be found by integrating (2.35) away from the initial conditions $U = 0$, $w = w_{\mathrm{D}}$ until the point $w = 0$, where we define $U(w = 0) = U_{\mathrm{nose}}$. Similarity solutions for various source fluxes are shown for Ro = 0.5 and Ro = 2 in figure 2.5. The solutions are all rarefactions (also called wedge intrusions or expansion waves) since they all have the property that U increases as w decreases. Rarefaction solutions have been previously described for coastal currents driven by PV jumps in Helfrich [2006] and JSM.

2.2.3.1 Termination of the rarefaction

In regions where the similarity solution applies, the slope of the λ_{R} characteristics – those on which the Riemann invariant $\mathcal{R}_{\mathrm{R}}$ is *not* uniform – can be computed as a function of w only. This is done for various parameter values in figure 2.6.

Since the solution grows monotonically in the source region, characteristics with larger values of w leave the source later and thus shocks form after a finite time if λ_{R} is not a monotonic decreasing function of w. Differentiating the characteristic speed with respect to w and evaluating at the wall gives

$$\left.\frac{\mathrm{d}\lambda_{\mathrm{R}}}{\mathrm{d}w}\right|_{w=0} = \frac{\partial\lambda_{\mathrm{R}}}{\partial w} + \frac{\partial\lambda_{\mathrm{R}}}{\partial U}\left.\frac{\mathrm{d}U}{\mathrm{d}w}\right|_{w=0} = H - 1 + \frac{H-2}{\sqrt{H}}\,U_{\mathrm{nose}} \tag{2.36}$$

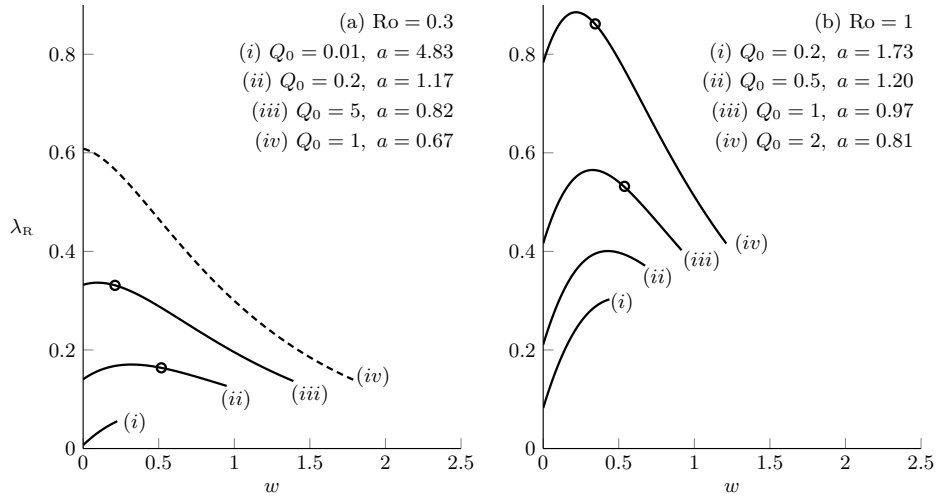

Figure 2.6: Characteristic slope $\mathrm{d}x/\mathrm{d}t = \lambda_\mathrm{R}$ as a function of w in regions where the similarity solution $U(w)$ applies (downstream of the source). The characteristic slopes are computed over the range $0 \le w \le w_\mathrm{D}$ with (a) Ro = 0.3, (b) Ro = 1. The dashed curve (a)(iv) does not form a shock, and circular markers on other curves indicate the maximum value of w immediately behind the shock for that outflow. Solid curves without a marker develop shocks that increase in width until $w = w_\mathrm{D}$ (a 'blunt-headed current').

A shock develops if (2.36) is positive. This occurs either if $H \ge 2$, or if

$$U_\mathrm{nose} < \frac{\sqrt{H}(H-1)}{2-H} \tag{2.37}$$

and $1 < H < 2$. For large Rossby number ($H > 2$) a shock always forms, while for moderate or small Rossby number a shock forms only if the vortical current overturns at the wall and the nose velocity is sufficiently small. From the plots of U_nose shown in figure 2.7, a slow nose velocity corresponds to smaller Q_0 (and bigger a) and so, as in the quasi-geostrophic limit, vortically dominated flows are more likely to develop a shock. The values of Q_0 below which a shock forms are marked on curves with $1 < H < 2$ in figure 2.7. The dashed curve in figure 2.6(a) is the only one presented that does not develop a shock – note that it has the smallest a of all solutions shown.

If no shock forms then the rarefaction is propagated by the λ_R characteristic, which reduce to $\lambda_\mathrm{R} = U$ when $w = 0$. The expelled fluid thus travels along the wall with velocity U_nose and the fluid velocity is equal to the propagation velocity. If, on the other hand, a shock does form then, applying conservation of mass moving at the shock speed V gives

$$\int_0^w (u - V)h \, \mathrm{d}y = 0 \tag{2.38}$$

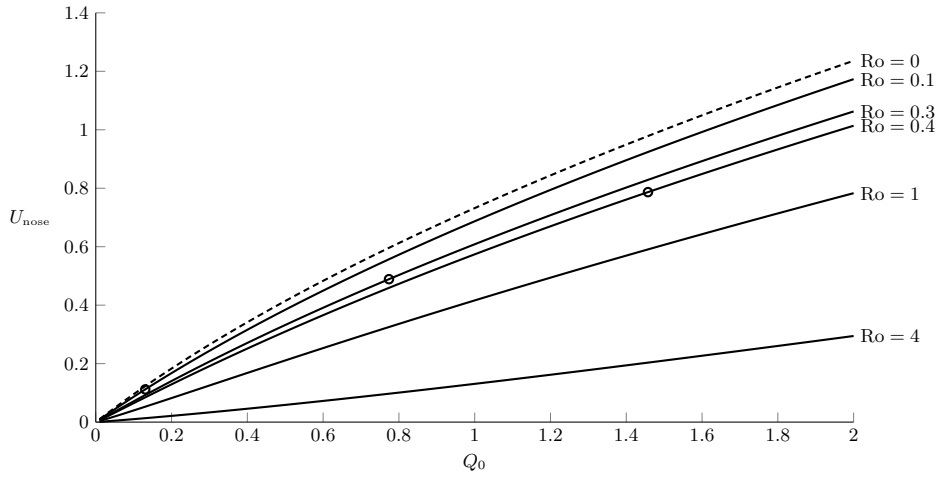

Figure 2.7: Speed at the coast, at the leading edge of the expelled fluid, for various Ro as a function of the source mass flux Q_0. Circles mark the value of Q_0 below which a shock forms in the expelled fluid, and curves without circles always form a shock. Also shown (dashed) is the wall velocity of the zero PVa solution.

or

$$V = \frac{\left(1 + (-1 + H + \sqrt{H}U)\cosh w + U \sinh w\right)^2 - (H + \sqrt{H}U)^2}{2(w - U + U\cosh w + (-1 + H + \sqrt{H}U)\sinh w)} \tag{2.39}$$

where U and w are evaluated just behind the shock.

Because shocks form after a finite time, jumps in w and U are initially small and increase in magnitude until one of two things happens. If the shock velocity V becomes equal to the characteristic speed λ_{R}, then at this point the shock and characteristic are tangential in the (x, t) plane and no more information can enter the shock. That is, there exists some value w_{M} such that $\lambda_{\mathrm{R}}(w_{\mathrm{M}}, U(w_{\mathrm{M}})) = V(w_{\mathrm{M}}, U(w_{\mathrm{M}}))$. The solution is thus a rarefaction terminating in a shock, where the width of the shock approaches w_{M} as $t \to \infty$. The circular markers on characteristic curves in figure 2.6 indicate the value of w_{M} for that particular Q_0 and H. An example of such a solution is displayed in figure 2.3(a), where the value of w_{M} is marked as a horizontal dashed line. Alternatively, the characteristic speed λ_{R} can be greater than V for all $0 < w < w_{\mathrm{D}}$. In this case, the shock keeps expanding until the maximum width of the current is reached, as seen in figure 2.2(b) where at late times the solution is simply a blunt current of width w_{D}. This situation occurs when vortical effects are dominant and a is large, as in the unmarked solid curves of figure 2.6.

2.2.4 Interpretation in terms of the speed ratio a

From §2.2.3, the qualitative behaviour of outflows can be categorised according to the form of the downstream current as: a rarefaction joining smoothly to the wall, a rarefaction terminating in a shock, or a blunt current. The space of parameters (Q_0, H) can be divided into three regions, the boundaries of which can be computed efficiently by integrating the Riemann ODE (2.35) to determine whether a shock forms and, if it does, whether the maximum jump magnitude is less than w_{D}.

Figure 2.8 compares the numerically-determined boundaries of these regions (numbered one, two and three respectively) with contours of a, to illustrate the extent to which the flow behaviour depends on Q_0 and H independently or whether, as in the quasi-geostrophic limit, the value of a alone is sufficient to categorise the solution. In the quasi-geostrophic limit (inset) the region boundaries coincide precisely with the contours $a = 1$ and $a = a_m \approx 1.87$ given in JSM. For larger Ro and Q_0, however, the region boundaries deviate from these values of a, although the progression from no shock to partial-width shock and full-width shock with increasing a remains.

2.2.5 Disturbance in the oceanic fluid

The similarity solutions obtained by integrating (2.35) give U_{nose} – the value of U at the point where $w = 0$, i.e. the fluid velocity at the leading edge of the expelled fluid. The horizontal dashed line in figure 2.3(b) marks the predicted value of U_{nose}, and the figure also indicates that $u_{\mathrm{w}} = U_{\mathrm{nose}}$ in the Kelvin wave that travels ahead of the river water. This follows by noting that the similarity solution is valid anywhere that the $\mathcal{R}_{\mathrm{C}}$ Riemann invariant is uniform – that is, at any point in the (x, t)-plane occupied by a λ_{C} characteristic that left the source region after the steady solution was set up. In particular, this region extends beyond the nose of the river water and into the oceanic fluid. As discussed below, this then creates a shock in the oceanic fluid (the Kelvin wave shock) and so all remnants of the initial conditions are erased with, at late times, $\mathcal{R}_{\mathrm{C}}$ uniform everywhere that the fluid is disturbed. Note also that in vorticity-dominated flows where a shock develops in the river water, this is through the collision of λ_{R} characteristics and so $\mathcal{R}_{\mathrm{C}}$ is conserved across the shock [El, 2005]. The similarity solution thus remains valid at the nose of river water, and $U = U_{\mathrm{nose}}$ ahead of the expelled fluid. Curves showing U_{nose} as a function of the total mass flux are presented in figure 2.7 for various Ro, along with the speed of the Kelvin wave-driven flow u_{KW} (dashed).

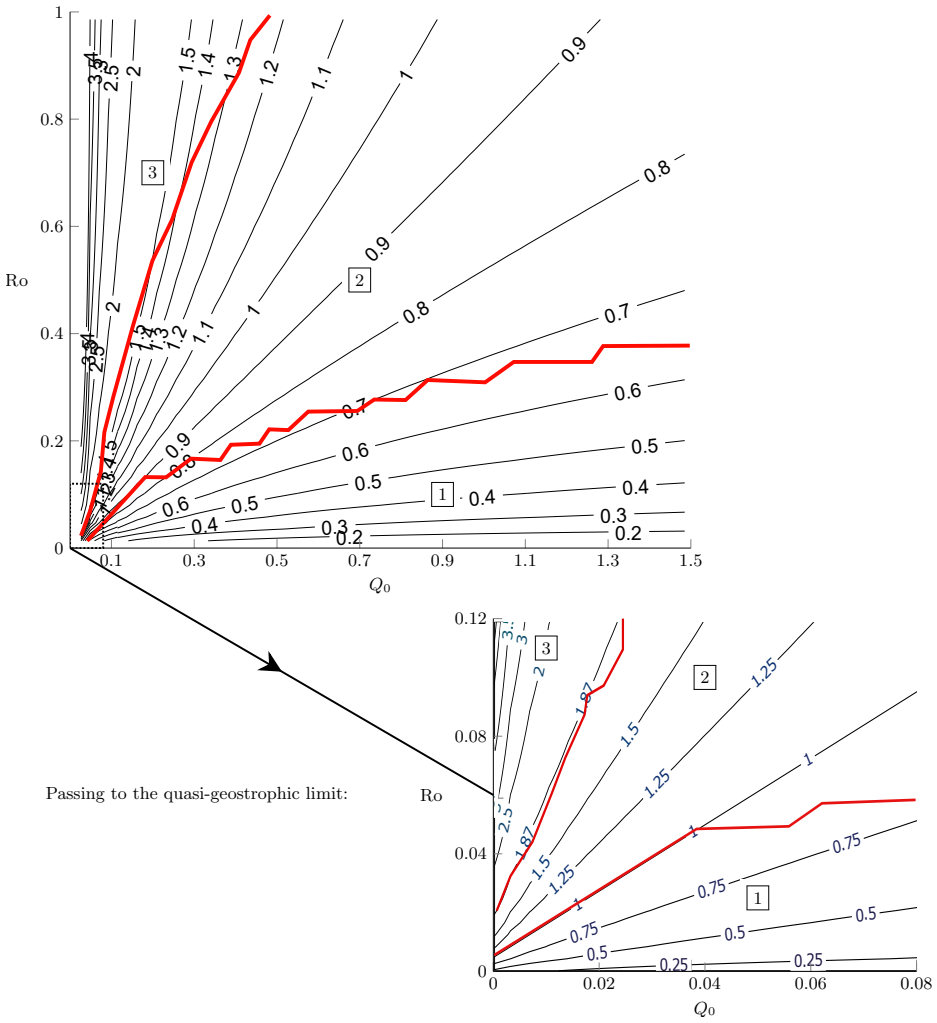

Figure 2.8: For positive PVa, the (Q_0, Ro) parameter space is divided into three regions (thick red curves). Solution type one joins smoothly to the wall, solution type two is a rarefaction terminating in a shock, and solution type three is a full-width shock. Also shown are contours of the speed ratio a. The inset details the behaviour in the quasi-geostrophic limit.

The motion in the oceanic fluid ahead of the river fluid is governed by (2.15) with $w = 0$,

$$\frac{\partial U}{\partial t} + (U + \sqrt{H})\frac{\partial U}{\partial x} = 0 \tag{2.40}$$

(c.f. the zero-PVa equation (2.19)). The propagation speed ahead of the river water is therefore the sum of $\sqrt{H}$, the non-dimensional speed of the linear Kelvin wave, and a nonlinear advection at speed U. Solutions to (2.40) always develop a shock when U is a decreasing function of x, as seen in the development of figure 2.3(b). Once a shock forms, the jump height increases until $U = U_{\text{nose}}$ and the shock propagates into the resting fluid

at a speed determined by the relevant Rankine-Hugoniot condition to be

$$V_{\mathrm{KW}} = \frac{U_{\mathrm{nose}}}{2} + \sqrt{H}. \tag{2.41}$$

The horizontal vertical lines on figure 2.3(b) are separated by $3V_{\mathrm{KW}}$, and match well with the solutions at $t = 9, 12$ even though U has not quite reached U_{nose}. A full 3-dimensional model of such shocks is considered in Fedorov and Melville [1996], and the propagation speed here agrees with their relation (7.20).

2.3 Outflows with negative PVa

When the expelled fluid has negative PV anomaly ($H < 1$), image vorticity opposes the Kelvin wave-driven flow and fluid travels both upstream and downstream. JSM show that steady flow only occurs if the outflow is vortically dominated ($a > 1$); otherwise the current expands indefinitely in the source region. For the positive PVa outflows of §2.2, fluid travels downstream only and the oceanic layer is undisturbed in $x < -1$. This matching condition leads to a full description of the steady current in the source region, which then provides initial conditions for integrating the Riemann ODEs (2.35) and the theory that describes the rarefaction solution. For outflows with negative PVa, fluid is disturbed both upstream and downstream and so analogous matching conditions do not exist. For outflows that evolve to become steady across the source region, an asymptotic theory based on properties of the steady quasi-geostrophic solution can be derived, and this is shown to agree well with numerical results even at moderate Ro.

2.3.1 Numerical results

An example of an unsteady, widening current is shown in figure 2.9 where $\mathrm{Ro} = 0.4$, $Q_0 = 0.7$ and so $a = 1.24$. Since $a > 1$ the outflow is vortically dominated and the corresponding quasi-geostrophic flow would evolve to become steady across the source region. Here, however, Ro is sufficiently large that the current width continues to grow. Some expelled fluid travels downstream, joining smoothly to the wall in a rarefaction with a Kelvin wave travelling ahead in the outer layer. The rest of the expelled fluid travels upstream. The boundary between fluid moving upstream and fluid moving downstream (where the upper-layer depth is at a maximum) is denoted $y = \widetilde{w}(x, t)$ and shown as a dotted blue curve in figure 2.9(a). Fluid thus travels upstream along the wall, before turning and heading

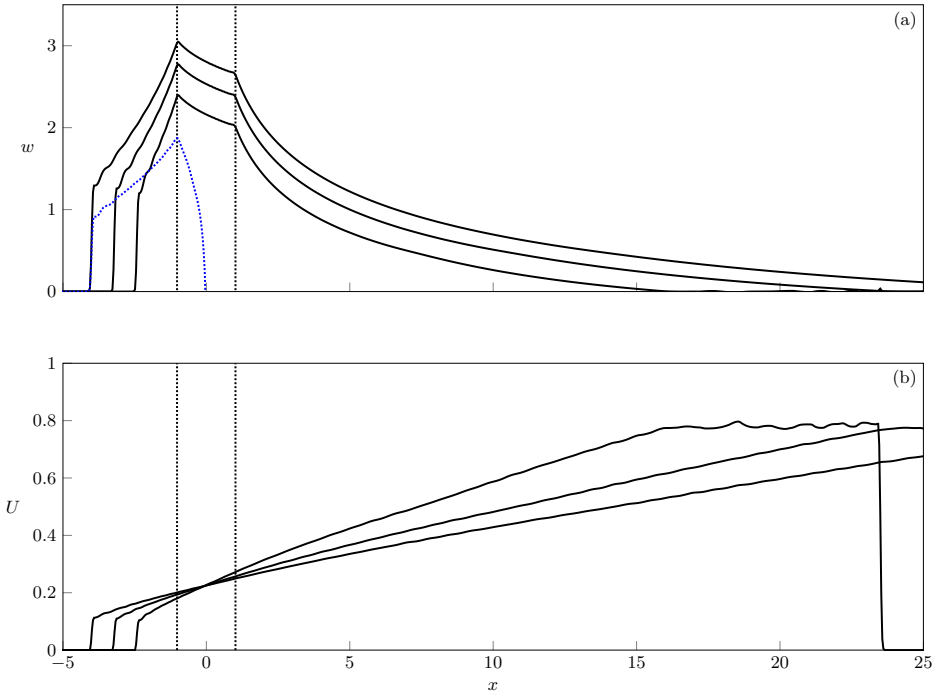

Figure 2.9: An outflow with negative PVa, Ro = 0.4, $Q_0 = 0.7$ and $a = 1.24$ at times $t = 20, 30, 40$. (a) The current width w, which continues increasing across the source region (marked by vertical dotted lines). The dotted blue curve gives $y = \widetilde{w}$ along which $u = 0$ (at $t = 40$). (b) The edge velocity U at $t = 20, 30, 40$.

downstream around the edge of the current, taking oceanic water with it as $U > 0$. Thus one important difference between solutions with positive and negative PVa is that outflows with negative PVa transport oceanic fluid from upstream of the source region to downstream. Computation of the off-shore velocity v reveals that fluid travels at infinite velocity around the upstream boundary of the outflow before heading downstream. This failure of the semi-geostrophic equations is due to the short length-scales in the shock region, as noted by Helfrich [2006].

Figure 2.10 shows an example of a steady current where Ro = 0.5, $Q_0 = 0.2$ and $a = 2.44$. In steady solutions, the curve $y = \widetilde{w}$ (blue, dotted online) touches the wall at $x = 1$, thus $u_{\mathrm{w}} = 0$ here and all the outflow first heads upstream before a portion recirculates to form the downstream current, which again is a rarefaction. In all solutions with negative PVa, the shock condition (2.37) cannot be satisfied with $U > 0$ and so the downstream rarefaction joins smoothly to the wall, demonstrating the importance of vortical flow in the formation of leading shocks. The steady solution is very similar to that of McCreary et al. [1997] (their figure 9) where upstream flows are driven by geostrophic adjustment of a density front. The upstream solution here is similar to the downstream solution for

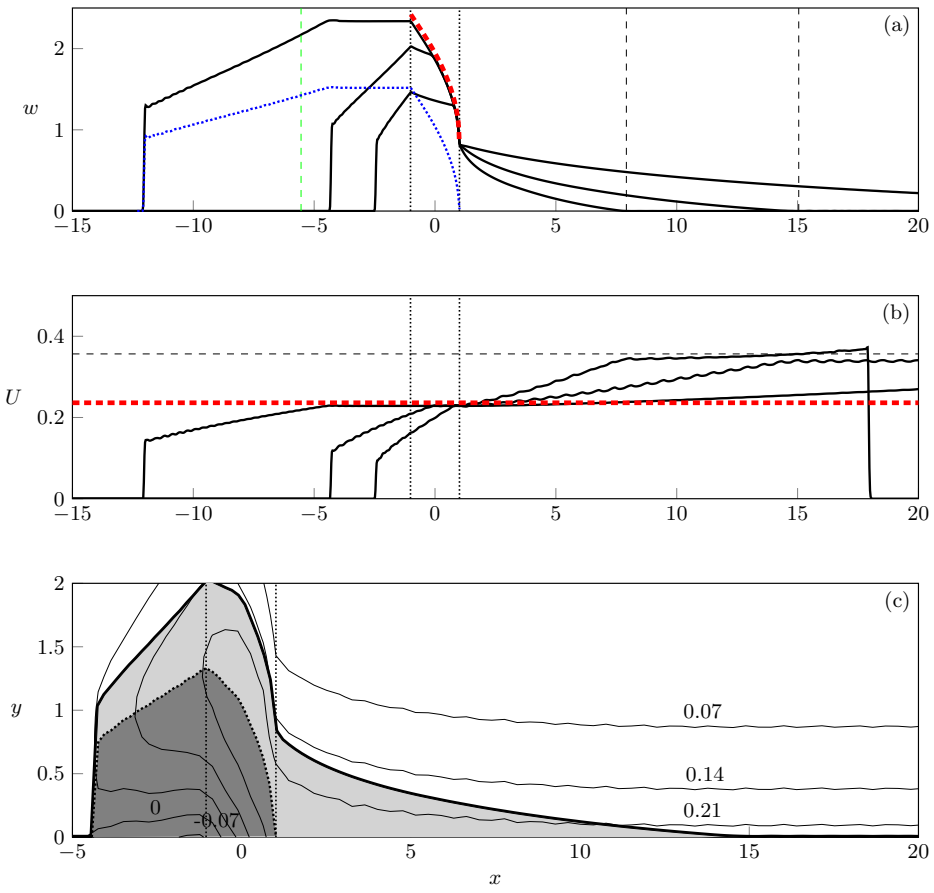

Figure 2.10: Solutions to the outflow problem with negative PVa, Ro $= 0.5$, $Q_0 = 0.2$ and $a = 2.44$ at times $t = 20, 40, 120$. (a) The current width w. The green dashed line at $x \approx -6$ indicates the location of the transect used to compare with experimental solutions in §2.4. (b) The velocity U at the current edge. The red dashed curves are the steady solutions $w_{\rm sn}$ and U_c from §2.3.2, the blue dotted line is $y = \widetilde{w}$, and the black dashed lines are derived from the theory of §2.3.3 and discussed there. (c) Contours of the depth perturbation $h - H$ at $t = 40$, where the shaded region indicates the expelled fluid.

positive PVa; a constant-width region near the source, then a rarefaction terminating in a leading shock. Figure 2.10(b) shows the edge velocity U, and the ripples visible at late times are the result of numerical dispersion. Figure 2.10(c) shows contours of the layer-depth perturbation $h - H$ at $t = 40$. The contour closest to the coast has a negative value: the outflow has caused a shallowing of the layer upstream of the source. The river fluid is shaded, with the region where $u < 0$ shaded darker, and the Kelvin wave is again seen to travel ahead of the river water and disturb the oceanic fluid.

2.3.2 Steady solutions across the source region

Since the oceanic layer is disturbed both upstream and downstream of the source, there are no matching conditions to determine the constants of integration and obtain a steady solution as in §2.2.2. Instead, specifying the constants requires two additional relations, which are based on quasi-geostrophic theory and later verified against numerical results to the initial-value problem.

First, note that one family of characteristic slopes λ_{C} are always positive (see appendix A), while the other set λ_{R} vanishes whenever $u_{\mathrm{w}} = 0$, i.e. when

$$U = U_c = \frac{1 - H}{\coth(w) + \sqrt{H}}. \tag{2.42}$$

Now $U_c < 0$ when $H > 1$ but $U_c > 0$ when $H < 1$, allowing λ_{R} to send information upstream if the PVa is negative. Thus the λ_{R} characteristic may be associated with the vortical flow and λ_{C} with the Kelvin wave-driven flow, as noted for the special case $H = 0$ in Kubokawa and Hanawa [1984a].

As in outflows with positive PVa, steady currents are controlled at the edge of the source region. In particular there exists a separatrix, i.e. a characteristic λ_{R} that has a turning point at $x = 1$. Characteristics that start to the right of the separatrix end up downstream of the source, and those that start to the left go upstream. There is thus a region in the wake of the turning point of the separatrix where characteristics that originate at $t = 0$ cannot penetrate, and characteristics instead propagate out from the turning point, where (2.42) is satisfied. The steady solution thus spreads upstream across the source region, starting at the downstream edge where it is controlled by the λ_{R} characteristic. Physically, this sets $u_{\mathrm{w}} = 0$ at the downstream edge of the source region and shows that, for steady solutions, all of the outflow must first head upstream driven by image vorticity, as seen in figure 2.10(c). There are, however, an infinite number of steady solutions that satisfy this control condition, and a further equation is needed to close the system.

Note that the curve $y = \widetilde{w}$, on which $u = 0$, can be computed from (2.7) as

$$\widetilde{w} = w - \log\left(\frac{\sqrt{H - 1 - U + \sqrt{HU}}}{\sqrt{H - 1 + U + \sqrt{HU}}}\right) \tag{2.43}$$

so that $w - \widetilde{w}$ is constant for steady solutions. Using (2.43), the system can be closed with one further relationship between w and $\widetilde{w}$. This is equation

(21) in McCreary et al. [1997],

$$\widetilde{w}_\infty = \frac{1}{2}\log\left(2\mathrm{e}^{w_\infty} - 1\right), \tag{2.44}$$

where the subscript refers to values evaluated far upstream at late times, after a steady current has completely developed. In McCreary et al. [1997], (2.44) is derived by taking the first term in an asymptotic expansion of a mass-balance equation similar to (2.38), which effectively requires that the coastal depth change is small relative to H. As such, (2.44) is also the relationship between w and $\widetilde{w}$ in the quasi-geostrophic solutions of JSM and so must hold for small Ro and Q_0 in the semi-geostrophic problem. We thus develop here a theory assuming that (2.44) holds for all values of Q_0 and Ro, and then verify numerically that this asymptotic approximation captures the qualitative behaviour of the outflow even at moderate Q_0 and Ro.

Given the conditions (2.42)-(2.44), the relevant solution to the steady equations (2.30) can be most succinctly described as

$$w_{\mathrm{sn}}(Q) = \log\left(\frac{r(Q) + \sqrt{r(Q)^2 + k^2 - 1}}{1 + k}\right) \tag{2.45}$$

where

$$k = \frac{U}{H - 1 + \sqrt{H}U}, \quad r(Q) = \frac{\sqrt{2(Q + c)} - 1}{H - 1 + \sqrt{H}U}$$

and c and U are determined by applying (2.42)-(2.44). The red dashed curves in figure 2.10 give w_{sn} and U_c, both of which are in good agreement with the numerical results even at $\mathrm{Ro} = 0.5$.

Figure 2.11 shows the downstream width of the steady current $w_{\mathrm{sn}}(Q_0) = w_{\mathrm{D}}$. As for positive PVa, for a given Ro the downstream current width increases with increasing mass flux. For fixed Q_0, the width dos not increase monotonically with Ro. As the magnitude of the PVa is increased, the current first contracts (in line with the results for positive PVa) before expanding again after $\mathrm{Ro} \approx 0.6$. Numerical computations show that for a given Ro there is a maximum flux Q_0 for which both (2.42) and (2.44) can be solved simultaneously, and thus an upper bound on the mass flux that supports a steady solution (marked by a dot in figure 2.11). The limited capacity of coastal currents to transport fluid with negative PVa was remarked on in Kubokawa [1991] and observed in laboratory experiments in Horner-Devine et al. [2006]. Figure 2.12(a) shows this maximum flux, which is not a monotonic function of Ro – a result discussed in more detail in §2.3.4. Also marked (dashed) in figure

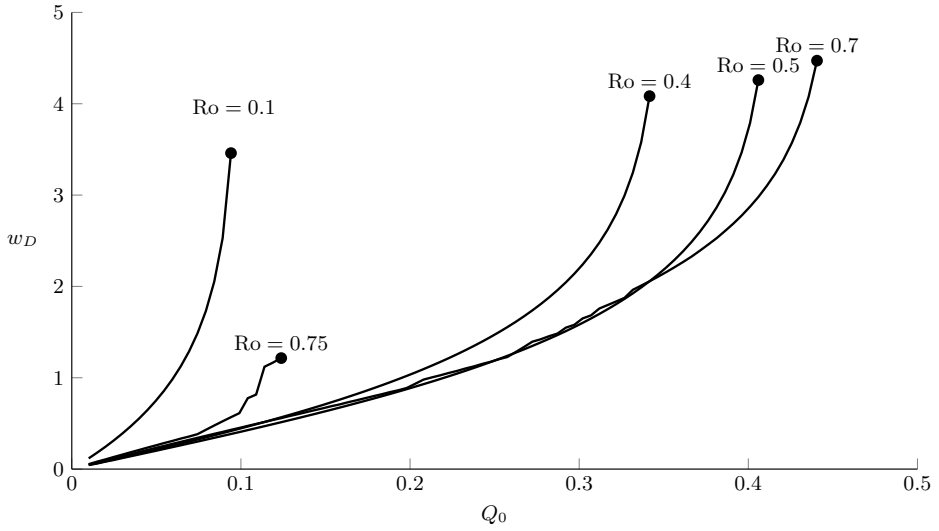

Figure 2.11: The steady solution width at the downstream edge, w_D, as a function of the flux Q_0. The largest Q_0 for which a steady solution exists at a given Ro is marked by a dot.

2.12(a) is the line $Q_0 = \mathrm{Ro}$, which is the maximum flux that supports a steady solution in the quasi-geostrophic limit.

In addition to the upper bound on Q_0 at fixed Ro, there is an absolute maximum of Q_0 over all Ro that supports a steady current. For real solutions, (2.45) requires that r is positive, which only occurs when $Q + c < 1/2$. As Q and c are non-negative, they must both individually be less than $1/2$. Thus no controlled steady solution exists when $Q_0 > 1/2$, as in the similar relation obtained in Whitehead and Salzig [2001] for flow out of a wide basin.

For negative PVa, only a portion of the outflow recirculates and so the downstream flux Q_d, given by

$$Q_d = \int_0^{w_\mathrm{D}} uh \, \mathrm{d}y = \frac{h^2}{2}\bigg|_{y=w_\mathrm{D}}^{y=0}, \tag{2.46}$$

is less than the total flux Q_0. Profiles of Q_d as a function of Q_0 are shown for various Ro in figure 2.12(b). The curve for $\mathrm{Ro} = 0.6$ lies above that for $\mathrm{Ro} = 0.5$, in accord with the non-monotonic behaviour of the total flux shown in (a).

2.3.3 Downstream rarefaction

Once the steady solution has been determined, analysis via Riemann invariants can be applied by integrating (2.35) away from the point $U(w_\mathrm{D}) = U_c$. In particular, figure 2.13 shows U_nose as a function of

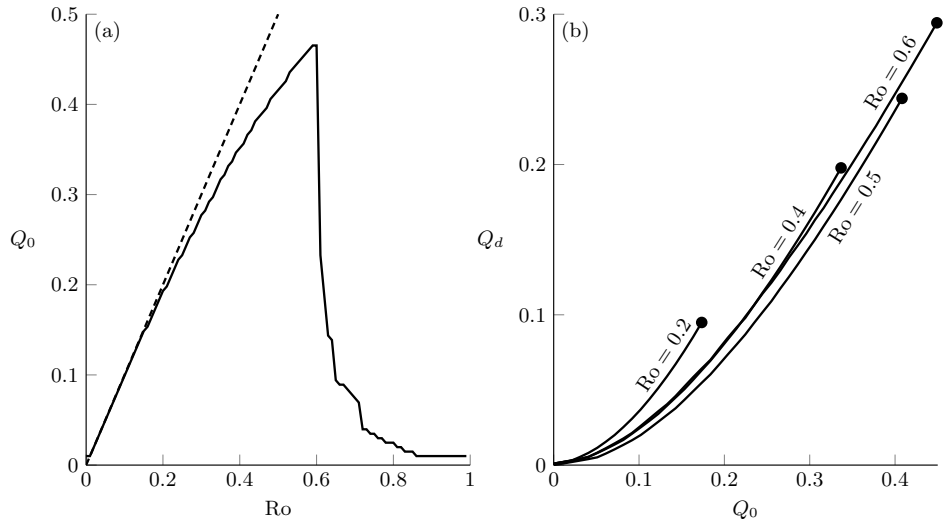

Figure 2.12: Mass flux for steady solutions with negative PVa. (a) The maximum mass flux supported by a given Ro. (b) The downstream mass flux Q_d as a function of total mass flux Q_0, for various Ro.

Q_0 for various Ro, allowing direct comparison with figure 2.7. As with positive PVa, increasing the mass flux for a fixed Ro increases the nose speed. However, in contrast to figure 2.7, fixing Q_0 and increasing Ro now increases the nose speed. That is, the fluid speed in the nonlinear Kelvin wave becomes slower and slower as the outer layer depth is decreased, irrespective of the sign of the PVa. A similar relationship between U_{nose} and layer depth is shown in figure 2 of Stern and Helfrich [2002], and in figure 3 of Martin et al. [2005]. The thin dashed horizontal line in figure 2.10(b) shows the value of U_{nose} predicted from the analysis of the Riemann invariants, and is in good agreement with the numerical solution. When the current width vanishes U_{nose} is also the propagation velocity of the expelled fluid at the farthest downstream edge. This is confirmed by the two vertical lines in figure 2.10(a), which are separated by $20U_{\text{nose}}$ corresponding to the interval between solutions at $t = 20$ and $t = 40$.

The upstream rarefaction for steady solutions with negative PVa can also be described by Riemann invariants, although in this case it is $\mathcal{R}_{\text{R}}$ that is uniform. Applying a similar test to (2.36) shows that a shock always forms upstream for negative PVa, and the same ideas about matching shock and characteristic velocities can be used to determine the maximum width of this, which increases as vortical effects become more important.

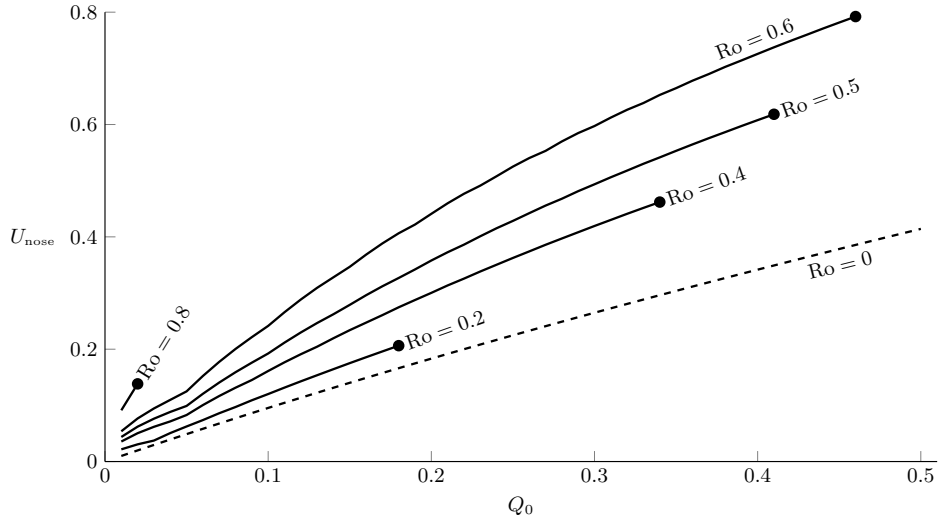

Figure 2.13: The nose speed U_{nose} for a controlled rarefaction, as a function of Q_0. The dashed line shows the wall velocity of the zero PVa solution.

2.3.4 Range of behaviours for negative PVa

For negative PVa, solutions can be categorised according to whether they are steady in the source region. In the quasi-geostrophic limit, JSM found that the speed ratio a was again of crucial importance; with $a > 1$ being necessary for a steady solution to form. Figure 2.14 shows the type of solution that occurs in semi-geostrophic flow as Ro and Q_0 are varied. The solution type was determined by attempting to compute a steady solution that satisfies both (2.42) and (2.44). If, for a given Q_0 and Ro, such a solution is possible, then these values permit a steady solution (region two). A higher-resolution sweep of the quasi-geostrophic limit of small Q_0 and Ro shows that the boundary between flows that are steady and those that grow (region one) aligns with the contour $a = 1$ as expected. In addition to this test, which is based on the asymptotic theory of §2.3.2, the initial-value problem was solved over the full parameter range, using a grid that was refined close to the apparent boundaries between regions. Although there were some quantitative differences between theoretical and numerical results (these being larger far away from the QG limit) the test based on (2.44) and (2.42) was found to correctly describe the qualitative behaviour of all solutions.

As for positive PVa, away from the quasi-geostrophic limit region boundaries can differ from contours of a, and so the system depends on Q_0 and Ro independently, although it is still the case that solutions with small a (Kelvin wave dominated) are of the growing type. The shape of

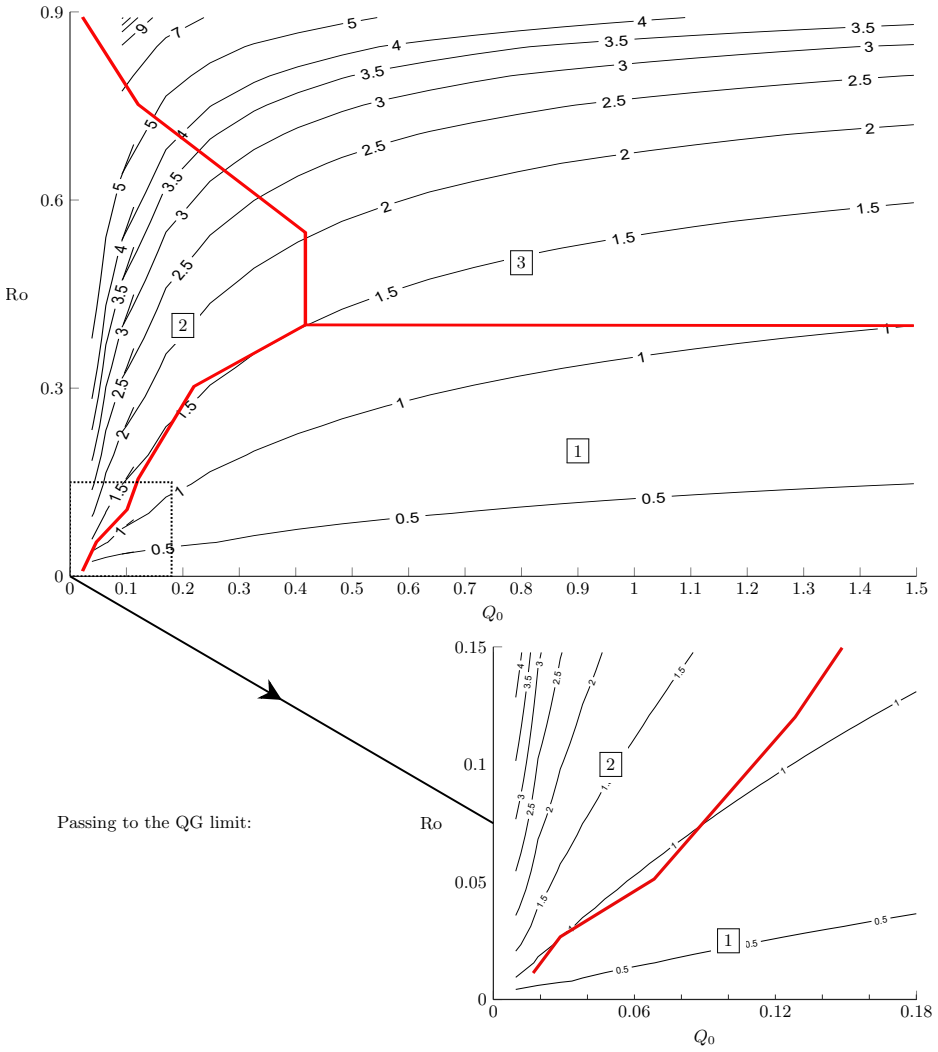

Figure 2.14: Solution type for negative PVa, compared with curves of constant speed ratio a. Solution type one grows indefinitely in the source region, solution type two is steady and solution type three is believed to separate from the wall. The inset shows that the boundary between regions one and two aligns with the curve $a = 1$ in the quasi-geostrophic limit.

region two reflects the results of figure 2.12(a), where increasing Ro allows a larger flux to be supported by steady solutions until, at some cut-off point around Ro = 0.6, the maximum permitted flux starts to decrease again. Increasing Ro past this point is associated with a rapid increase in the value of a – for flows that are strongly dominated by vorticity, steady solutions occur only at small fluxes.

Parameter values in the region marked three on figure 2.14 give rise to complex solutions to (2.42) and (2.44). It appears that as the current width grows, the coastal layer depth h_w decreases to zero and the expelled fluid separates from the coast. Separation is explicitly excluded from the

present model by the assumption that the expelled fluid lies in $0 < y < w$. Preliminary results from adapting the model to remove this restriction suggest that the fluid tries separates in the source region, as discussed for separated flow out of a basin by Helfrich et al. [1999] and Gill [1977], as well as for laboratory experiments in Horner-Devine et al. [2006]. Separation in the source region modifies the outflow profile $Q(x)$ and thus alters the problem beyond the scope considered here.

If for a given Q_0 and Ro the solution starts to separate ($h_\mathrm{w} = 0$), the initial-value problem is halted and the parameter pair is included in region three. It appears that the boundary between solutions which grow and those which separate is sharp in terms of Ro – if the Rossby number is increased beyond some critical value of Ro ≈ 0.4 then all unsteady flows eventually separate from the wall.

2.4 Discussion

Numerical and theoretical results for coastal outflows have been discussed using a semi-geostrophic model that allows for large variations in Rossby number by adjusting the depth of the outer buoyant ocean layer. For positive PVa (when the depth of the buoyant layer is greater than the potential vorticity depth of the river water) a full theory has been developed based on numerically computed Riemann invariants, while for negative PVa an asymptotic theory for solutions that are steady across the source region is derived. The speed ratio a, which measures the relative strengths of Kelvin wave-flow and image vorticity, is a useful guide to determining the behaviour of the outflow. However, for moderate and larger Rossby number, solutions depend on both Ro and the total mass flux Q_0 independently. Diagrams describing the behaviour of the solutions for a given Q_0 and Ro are presented for positive PVa in figure 2.8, and for negative PVa in figure 2.14.

For positive PVa, the range of possible behaviours is the same as in the quasi-geostrophic limit of JSM. All currents flow exclusively downstream, are steady across the source region, and are led by a rarefaction that either joins smoothly to the wall or develops a shock in finite time. A key feature here, however, is that the Kelvin wave that propagates ahead of the expelled fluid does so at a finite speed. The speed of the fluid within the Kelvin wave, U_nose, is found to be greater when the depth of the outer layer is shallower. The propagation speed of the Kelvin wave is given as V_KW in (2.41), while the propagation speed of the expelled fluid can be computed from (2.39) using the maximum values of w and U just behind the shock. The ability

to measure the fluid and propagation speeds of these two waves separately is a key feature of this model, and the way that these quantities vary with the parameters, along with the range of behaviours observed, highlights the importance of vortical turning in determining how the outflow behaves. It is also important to note that most experiments on outflows use colouring to identify the expelled fluid, and thus tend to report on disturbances only within this coloured region, leaving laboratory investigation of the Kelvin wave in the outflow problem as an avenue for future work. Once the Kelvin wave has passed a station x the qualitative behaviour at that station is much the same as in the QG limit. This result supports the use of a coastal boundary condition to model the passage of the Kelvin wave in the following chapters.

For negative PVa, steady and growing solutions exist as in the quasi-geostrophic limit, with steady solutions occurring in cases where the vortical flow is stronger than the Kelvin wave-driven flow. However, for large Ro (shallow oceanic layers) sufficiently strong forcing can cause the flow to separate from the wall – a phenomenon that has previously been noticed when studying related flows and one that remains to be explored further in the present context. The steady solutions obtained here are critically controlled at the downstream edge of the source: the phase-speed of all long-wave disturbances is positive in $x > 1$, so the flow here is supercritical, while in $x < 1$ long-wave disturbances can propagate in either direction and the flow is subcritical. All fluid first heads upstream along the wall, before a portion of it recirculates and re-crosses the source region. This creates an anti-cyclonic circulation within and upstream of the river mouth, as in the density driven solutions of McCreary et al. [1997], the numerical results of Isobe [2005] and the laboratory experiments of Thomas and Linden [2007] and Avicola and Huq [2003a]. That similar qualitative behaviours are observed here as in the experiments supports an analogy between PV jumps and density fronts previously alluded to in McCreary et al. [1997], and possibly suggests that both mechanisms contribute to the behaviour of real plumes.

The photograph of the Elwha river after dam removal (figure 1.1) bears a striking similarity to solutions with positive PVa (figures 2.2, 2.3). Although the outflow after dam removal involved the expulsion of sediment-laden river water (and so differs from the homogeneous-density model considered here) it is evident that there was a strong downstream transport of river water, with a qualitatively similar shape to the positive PVa solutions of §2.2. A comprehensive survey of Juan de Fuca (the strait into which the Elwha runs) was conducted between 1975-1980 and shows

that prevailing currents and tides carry surface water towards the sea, i.e. leftwards out of the river mouth [Cannon, 1978, Holbrook et al., 1980, Holbrook and Halpern, 1982]. Although rightward ambient flow does occur, it is comparatively rare and weak and is thus unlikely to be the sole cause of the rightward turning in figure 1.1. Further Curran et al. [2008] presents data which suggests that the outflow after dam removal satisfies the criteria for a surface-advected plume [Yankovsky and Chapman, 1997] and so the behaviour of the outflow should not be affected by topography.

Horner-Devine et al. [2006] study experimentally the injection of fluid into a rotating annulus of uniform, denser fluid. Their results are therefore most comparable to our model with small H (large negative PVa). Indeed, they find a bulge in the source region and a thinning current that propagates downstream. Figure 2.15 makes a quantitative comparison of dimensional u^* from our model with that from their experiments, in an off-shore transect that intersects the bulge centre (the green dashed line in figure 2.10(a)). Non-dimensionalising their experimental values gives a mass flux $Q_0 = 0.53$, and so our model predicts unsteady flow in the source region for all H. JSM show that in the QG limit, the growth of the current width $\partial w/\partial t$ is proportional to $1/t$ for unsteady solutions, and so the flow is approximately steady at large t. The best comparison between our theory and the results of Horner-Devine et al. [2006] is therefore made by taking the smallest H for which the flow remains attached to the coast sufficiently long to become approximately steady. The choice of $H = 0.4$ allows the numerical integration to run until $t = 80$, and tests with other values of H show that the quantitative behaviour is remarkably unaffected. In the experimental result (solid curve) the flow within the bulge is bi-directional, with fluid closer to the wall travelling upstream under the influence of image vorticity – something that is only possible when the source fluid has lower PV than the oceanic fluid. There is excellent agreement between the wall velocity of the model and the near-wall velocity observed in the experiment, and both the predicted and the observed velocities increase until they reach a maximum value at a similar off-shore co-ordinate (which occurs at the PV jump in our results, and the edge of the bulge in the laboratory experiment) before decaying to zero. As $H \to 0$, $a \to \infty$ and the vortical length-scale $L_{\mathrm{V}} \to 0$, so we expect that vortical effects will only be felt close to the wall. Indeed the agreement between the present model and the experiment is best closer to the coast and the largest discrepancies occur further offshore, where the differences in set-up between the experiment and the model are more significant.

The present model focuses on the role of PVa in determining plume

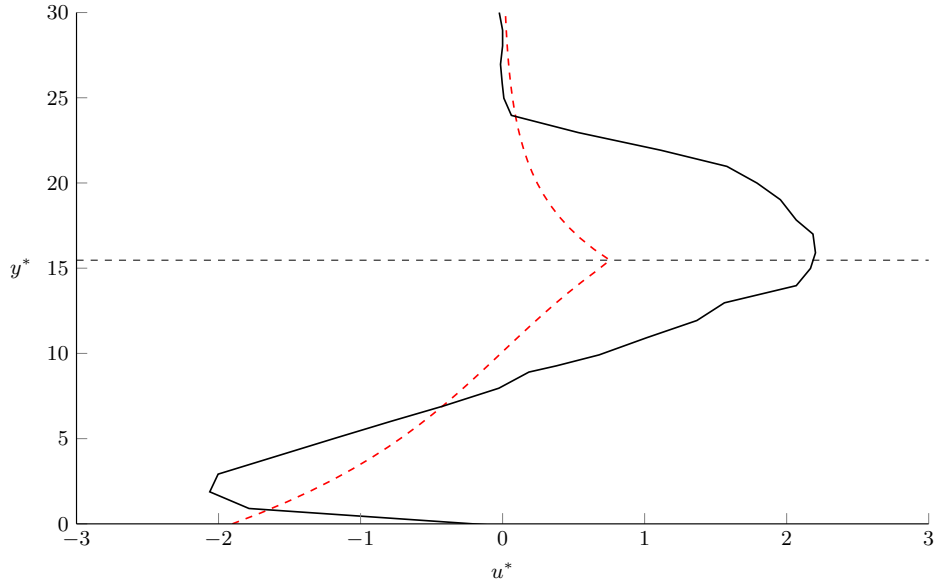

Figure 2.15: Comparison between numerical results from the present model with $H = 0.4$, $Q_0 = 0.53$ (red, dashed) and laboratory experiment VB6 from Horner-Devine et al. [2006] (black, solid). The dimensional along-shore velocity u^* is shown as a function of the off-shore co-ordinate y^*. The transect is taken at the mid-point between the downstream edge of the source and the upstream edge of the expelled fluid, and so intersects the centre of the bulge, at the time $t = 30$. The horizontal dashed line gives w at this value of x and t.

behaviour by assuming that the expelled fluid and the buoyant ocean layer have the same density. This is rarely, if ever, true in an ocean setting where horizontal buoyancy gradients also play a role in the formation and propagation of coastal currents, and so direct applicability of the model to a real ocean is limited. On the other hand, the two mechanisms of image vorticity and Kelvin-wave driven flow described in this work are still present, and in the limit of weak horizontal stratification it is possible that they are the dominant dynamical factors. Further discussion of how the present model relates to the real oceans, including the important effects of topography and outlet geometry, is given in §3.5.

Chapter 3

Vortex competition in coastal outflows

In this chapter we return to the quasi-geostrophic model, and investigate the role played by spatial variability of outflow vorticity in determining the behaviour of the plume. That is, we extend JSM's model to an outflow with spatially-varying (but still piecewise-uniform) PV. In particular we choose the outflow profile to be 'competitive', i.e. it consists of regions of positive and negative vorticity arranged so that image vorticity drives a tendency for fluid emerging from each region to turn and propagate into the other. We show that for such outflows plume behaviour can be categorised by the net vorticity flux through the river mouth (the integral of vorticity times velocity across the source region). We show that if this integral is positive the cyclonic region dominates, and all of the expelled fluid turns to the right on leaving the source (the coastal current mode). If the cyclonic and anticyclonic contributions cancel, as in the laboratory experiments of Avicola and Huq [2003a,b], then the flow is unstable in the source region and a bulge may form downstream of the river mouth. The importance of spatially-varying vorticity has been discussed previously in numerical and laboratory studies (for example, Avicola and Huq [2003b], Huq [2009], Chen [2014]) and the present work supports this discussion by making using of the analytical results that are available in the idealised long-wave QG model.

Section 3.1 describes the quasi-geostrophic model, and determines

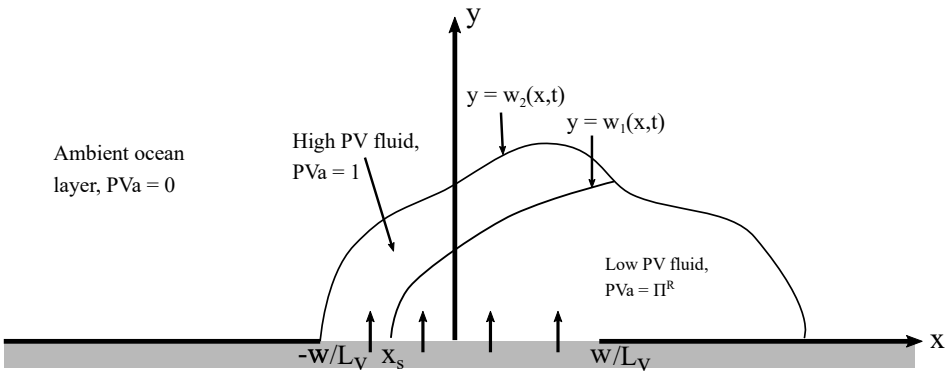

Figure 3.1: Fluid is expelled from a coastal source located at $|x| < W/L_{\mathrm{V}}$, $y = 0$. The ocean fluid in $y \geq 0$ initially consists of an upper, active layer (with the same density as the outflow) on top of a deep, denser, inactive layer. The source vorticity is positive in $x < x_S$, and negative in $x > x_S$. Variables are non-dimensional, with the relevant scales defined below.

the range of parameters for a competitive outflow. §3.2 presents steady solutions to the long-wave limit of the model, and derives a necessary and sufficient condition for the existence of the coastal current mode. The present model is similar to that employed by Kubokawa [1991], in which part of the outflow has negative PVa and part has the same PV as the upper ocean layer, and §3.2.1.2 presents their results in terms of net vorticity flux. The full QG equations are solved numerically in §3.3, and the unsteady features of these results are discussed in §3.4. Section 3.5 discusses the relevance of these results to real outflows.

3.1 Model and governing equations

Consider flow relative to a frame rotating about a vertical axis Oz at constant angular speed $f/2 > 0$. Suppose that there is a straight, vertical coast at $y = 0$ and consider flow in $y \geq 0$ only, with Ox directed along the coast. Initially the ocean in $y > 0$ is still, with a buoyant upper layer of uniform depth H lying on top of an infinitely deep, dense layer. At time $t = 0$ a source in the coast located at $|x| < W$ starts emitting fluid of the same density as the buoyant layer at a rate $U_{\mathrm{S}} = Q_0 H_S$ per unit time, where H_S is a measure of the source depth and so Q_0 is the outflow area flux. If $|H - H_S|$ is sufficiently small then the flow is geostrophic everywhere and the motion is governed by the quasi-geostrophic equation for conservation of PV, formulated in terms of $h(x, y, t)$, which measures the departure of the depth interface from the initial value H. Quasi-geostrophic dynamics apply when the source Rossby number $\mathrm{Ro_S}$ is small, where recall from §1.1 that $\mathrm{Ro_S} = U_{\mathrm{S}}/(fW)$. We may take $U_{\mathrm{s}} = 1\mathrm{m\,s^{-1}}$ and $f \approx 10^{-4}\mathrm{s^{-1}}$

as representative values, while for a wide river and $W \approx 10$km, which gives $\mathrm{Ro} = 1$. Thus nonlinear advection (non-quasi-geostrophic dynamics) may be important in many river plumes (although Münchow and Garvine [1993b] estimate $\mathrm{Ro_S} = 0.1$ at the mouth of the Delaware river). Further discussion of how the restriction to quasi-geostrophy may affect the present model is given in §6.

Under these assumptions, the source vorticity profile can be expressed in terms of the outflow velocity and PVa, which can be chosen in such a way that the outflow is competitive. One simple way to do this is to let the PVa take two values: $\Pi_0 > 0$ in $-W < x < x_S^*$, and $\Pi_0^{\mathrm{R}} < 0$ in $x_S^* < x < W$, where x_S^* is the location of the dividing streamline in the outflow at which the sign of the vorticity changes. Fluid that exits the outflow to the left of x_S^* has positive vorticity, and will be referred to as HPVF (high potential-vorticity fluid). The HPVF competes with fluid that exits to the right of x_S^* and has negative vorticity (LPVF, low potential-vorticity fluid). The choice of piecewise-constant PVa allows for accurate and efficient numerical simulations of the flow using the method of contour dynamics with surgery [Dritschel, 1989], and also facilitates the analytical results that follow. A similar model with piecewise constant vorticity was used by Stern and Whitehead [1990] to study the flow of a jet around a corner in a non-rotating environment. A schematic of the situation described above is shown in figure 3.1.

Following JSM, horizontal lengths are non-dimensionalised on the source-vortex scale $L_{\mathrm{V}} = (Q_0/\Pi_0)^{1/2}$, speeds on Q_0/L_{V} and t on the advective time $L_{\mathrm{V}}^2/Q_0 = (\Pi_0)^{-1}$. The governing equation is therefore

$$\nabla^2\psi - \psi/a^2 = \begin{cases} 0 & \text{in the ambient} \\ 1 & \text{in HPVF} \\ \Pi^{\mathrm{R}} & \text{in LPVF.} \end{cases} \tag{3.1}$$

Here, $\psi = g'h/fQ_0$ is a streamfunction that is related to the non-dimensional velocity by $(u, v) = (-\psi_y, \psi_x)$, and $\Pi^{\mathrm{R}} = \Pi_0^{\mathrm{R}}/\Pi_0$. The parameter $a = L_{\mathrm{R}}/L_{\mathrm{V}}$ is the non-dimensional Rossby radius, and is discussed in more detail in §1.4. The choice of L_{V} for horizontal length-scale is a natural one for the study of vortical effects, as it ensures that the width of the vortically-drive current remains $O(1)$, while the Kelvin-wave decay scale changes with a. Later we will take the long-wave limit of (3.1) and require that $L_{\mathrm{V}}/W \ll 1$, although the numerical simulations that follow show that this has little qualitative effect on the results.

The source is impulsively switched on at $t = 0$, with the outflow

velocity given by a specified profile $Q'(x)$, which we assume to be positive throughout the source region (i.e. there is no inflow). The boundary condition at the coast is therefore

$$v(x,0,t) = \begin{cases} 0, & |x| > W/L_{\mathrm{V}} \\ Q'(x), & |x| < W/L_{\mathrm{V}}. \end{cases} \tag{3.2}$$

Integrating (3.2) shows that the coastal interface displacement is set for all time as

$$\psi(x,0,t) = Q(x), \tag{3.3}$$

with $Q(x) = 1$ for $x > W/L_{\mathrm{V}}$ and $Q(x) = 0$ for $x < -W/L_{\mathrm{V}}$. Thus the boundary condition (3.3) represents the signature of the Kelvin wave in the QG limit. When the Rossby number is finite (as in §2), the Kelvin wave propagates along the coast ahead of any frontal waves and sets the boundary condition for the vortical flow behind it. In the QG limit, the Kelvin wave travels at effectively infinite speed, setting the boundary condition (3.3) at $t = 0^+$ and for all time [Hermann et al., 1989]. Thus the role of the coastal Kelvin wave is to set up a steady geostrophic background flow that interacts with vortical effects. Below, for brevity, we will refer to this simply as the 'Kelvin-wave flow'. Although here we restrict ourselves to steady mass efflux profiles, the extension to unsteady profiles $Q(x,t)$ follows immediately and is considered by both Kubokawa [1991] and, for the uniform-PV case, in Southwick et al. [2017].

The relative vorticity is given by $\zeta = \nabla^2\psi$, so from (3.1) and (3.3) the source vorticity profile is completely specified as

$$\zeta(x,0,t) = \zeta_S(Q) = \begin{cases} 1 + Q/a^2 & 0 < Q < Q_+ \\ \Pi^{\mathrm{R}} + Q/a^2 & Q_+ < Q < 1, \end{cases} \tag{3.4}$$

where $Q_+ = Q(x_s)$ is the fraction of the outflow occupied by the HPVF. Note that ζ_S is a function of Q with x appearing parametrically in (3.4), so that many of the results below do not depend on the choice of outflow profile $Q(x)$.

Equation (3.4) shows that the source vorticity in the HPVF is always positive. Some of the LPVF will have negative vorticity if $\Pi^{\mathrm{R}} + Q_+/a^2 < 0$, and all of the LPVF has negative vorticity if $\Pi^{\mathrm{R}} + 1/a^2 < 0$. Therefore the entire outflow is competitive if and only if $\Pi^{\mathrm{R}} < -1/a^2$. Figure 3.2 illustrates two vorticity profiles: in (a) the whole outflow is competitive, while in (b) the non-competitive region of the LPVF where $\zeta_S > 0$ is shown dotted.

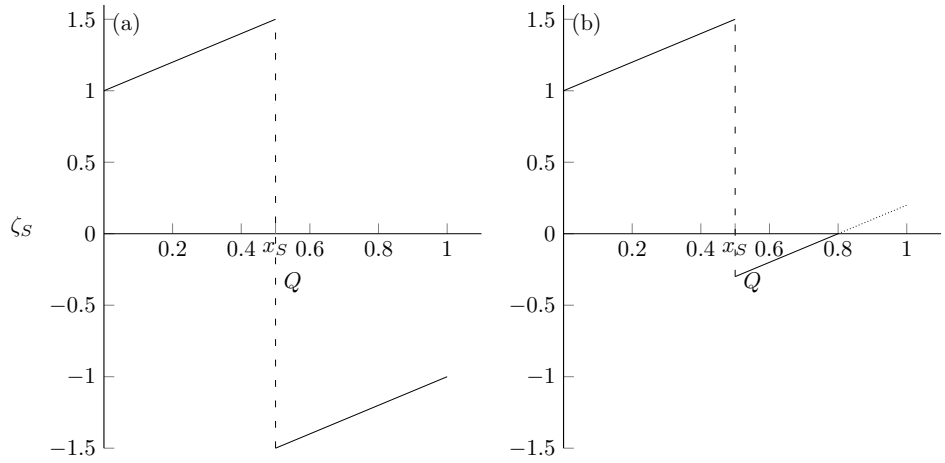

Figure 3.2: Two examples of the source vorticity profile, $\zeta_S(Q)$, with $a = 1$ and $Q_+ = 0.5$. (a) $\Pi^{\mathrm{R}} = -2 > 1/a^2$, so that the outflow is competitive. (b) $\Pi^{\mathrm{R}} = -0.8 < -1/a^2$ so that the outflow is competitive for $Q < 0.8$.

3.2 The coastal current mode

JSM show that if the source vorticity is positive everywhere no bulge forms and all of the outflow travels downstream in a steady, constant-width coastal current. Kubokawa [1991] finds that this 'coastal current mode' occurs if Q_+ is greater than a critical value Q_{C}, which is a function of Π^{R} and a. In this section we present solutions that fully describe the coastal current mode in the long-wave limit of the present model, and show that the critical ratio can be interpreted in terms of a simple condition on the source vorticity.

3.2.1 The steady long-wave equations

The field equation (3.1) can be solved analytically in the long-wave limit, where disturbances to the interface occur on scales that are much larger in the x-direction than in the y-direction. Formally, this limit requires that the source is wide compared to the chosen length-scale L_{V}, however we are guided by JSM who find that their long-wave theory captures the essential dynamics even in the limiting case where the outflow is modelled as a point source. Therefore let $\epsilon = L_{\mathrm{V}}/W$ be small and introduce $X = \epsilon x$ and $T = \epsilon t$, so that the source region is $|X| < 1$. Suppose additionally that the boundaries that mark the PV jumps do not overturn, so there are single-valued functions $y = w_1(X,T)$ and $y = w_2(X,T)$ that denote the boundaries between LPVF and HPVF, and between HPVF and the ambient ocean layer respectively. In the coastal current mode, the existence of single-valued functions to describe the location of the PV jumps implies

that $w_2 \geq w_1$. Under these assumptions, the field equation (3.1) becomes, at leading order,

$$\psi_{yy} - \psi/a^2 = \begin{cases} 0 & y > w_2 \\ 1 & w_1 < y < w_2 \\ \Pi^{\mathrm{R}} & 0 < y < w_1. \end{cases} \tag{3.5}$$

We may now consider (3.5) as the governing equation for the plume in coastal current mode and revert to using the variables x and t. Treating w_1 and w_2 as fixed, equation (3.5) may be solved subject to the coastal boundary condition (3.3), the far-field condition

$$\nabla\psi \to 0 \text{ as } y \to \infty, \tag{3.6}$$

and continuity of ψ and u at $y = w_1$ and $y = w_2$. We may write ψ as:

$$\begin{aligned} \psi_0 &= Q_e \mathrm{e}^{-y/a} && y > w_2, \\ \psi_+ &= -a^2 + a^2 \cosh\left[(y - w_2)/a\right] + Q_e \mathrm{e}^{-y/a} && w_1 < y < w_2, \\ \psi_- &= -a^2 \Pi^{\mathrm{R}} + A \cosh\left[(y - w_1)/a\right] \\ &\quad + B \sinh\left[(y - w_1)/a\right] && 0 < y < w_1, \end{aligned} \tag{3.7}$$

where the far-field condition (3.6) and continuity at $y = w_2$ have already been applied. The remaining coefficients A, B and Q_e are to be determined by continuity conditions at w_1 and the coastal boundary condition (3.3). The function Q_e is the net flux of ocean fluid at any station x.

For the particular case when the outflow is in coastal current mode, A, B and Q_e can be determined analytically. Since all of the river water travels downstream, ψ takes the values Q_+ and zero on $y = w_1$ and w_2 respectively. The unique solution in the ambient is therefore $\psi_0 \equiv 0$ so that $Q_e = 0$ and the ambient layer is stagnant. The flow in $-1 < x < x_S$ is unaffected by the region of LPVF, so the solution is exactly the same as for the positive-PVa outflows of JSM. That is, $w_1 = 0$ and

$$\cosh\left(w_2/a\right) = 1 + Q/a^2. \tag{3.8}$$

Downstream of x_S, the condition $\psi(w_1) = Q_+$ is applied to (3.7):

$$Q_+ + a^2 = a^2 \cosh\left[(w_2 - w_1)/a\right], \tag{3.9}$$

$$Q_+ + a^2 \Pi^{\mathrm{R}} = A, \tag{3.10}$$

so that the width of the HPVF, $w_2 - w_1$, is constant. The along-shore velocity u is continuous at $y = w_1$ so that from (3.7),

$$B = a^2 \sinh\left[(w_1 - w_2)/a\right]. \tag{3.11}$$

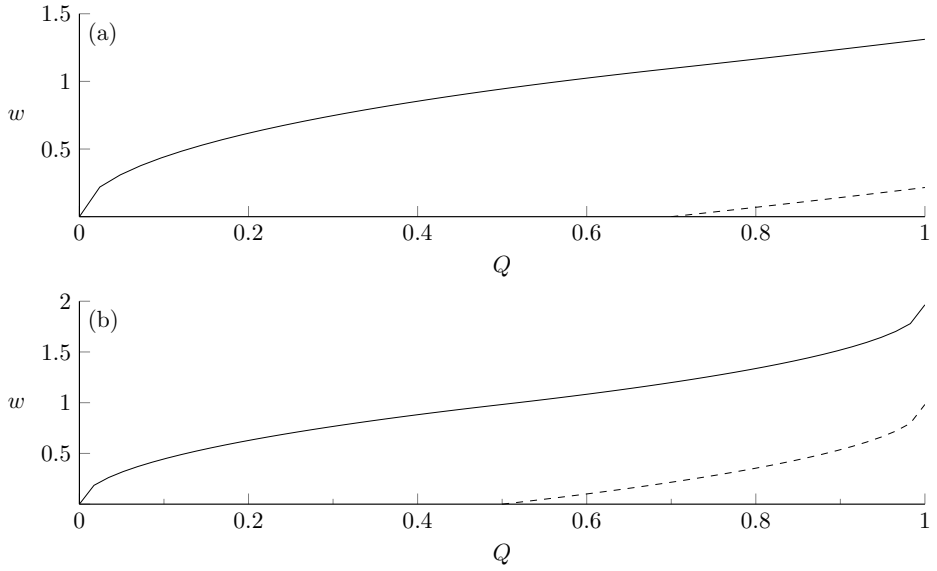

Figure 3.3: Steady long-wave profiles in the source region. The solid curve shows w_2, the boundary of the river plume, and the dashed curve is w_1, the location of the PV jump within the current. (a) $a = 0.8$, $Q_+ = 0.7$, $\Pi^{\mathrm{R}} = -2$, (b) $a = 1.5$, $Q_+ = 0.5$, $\Pi^{\mathrm{R}} = -1.44$.

The coastal boundary condition (3.3) can then be written in terms of w_1 alone:

$$Q + a^2\Pi^{\mathrm{R}} = (Q_+ + a^2\Pi^{\mathrm{R}})\cosh(w_1/a) + \sqrt{(2a^2Q_+ + Q_+^2)}\sinh(w_1/a). \tag{3.12}$$

Equation (3.12) only has physically meaningful solutions for certain values of the parameters a, Q_+ and Π^{R}, and it is these conditions that determine whether the coastal current mode is possible. We will discuss these conditions and their physical meaning presently, but first note that if the conditions are met the solution in the source region is given by

$$\frac{w_1}{a} = \log\frac{F(Q)}{F(Q_+)}, \tag{3.13}$$

for

$$F(Q) = a^2\Pi^{\mathrm{R}} + Q + \sqrt{Q^2 + 2a^2(\Pi^{\mathrm{R}}(Q - Q_+) + Q_+)},$$

where the positive root to the quadratic equation (3.12) is chosen as the only physically relevant solution. This expression is valid in the source region, and gives the offshore location of the internal PV jump as a function of Q. The boundary of the outflow plume, w_2, can be found through (3.9). Downstream of the source, $Q \equiv 1$ and the coastal current has constant width.

Figure 3.3 shows two examples of steady long-wave profiles in the source region, plotted as a function of Q. In both cases, the dashed curve is w_1

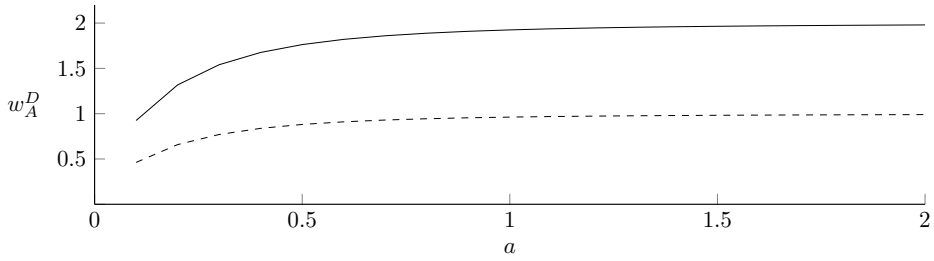

Figure 3.4: The width of the coastal current, as a function of a, for the special case where the source vorticity profile is antisymmetric. The dashed curve shows the width of the interior PV jump.

from (3.13), and the solid curve is the plume boundary w_2. Figure 3.3(b) has $Q_+ = 0.5$ and $\Pi^{\mathrm{R}} = -1 - 1/a^2$, with these parameter values chosen so that the source vorticity profile is antisymmetric about $x = 0$ and the ratio of HPVF to LPVF is 1:1. This is the source vorticity profile described in the experiments of Horner-Devine et al. [2006], and consists of a cyclone and anticyclone of equal and opposite strength. Figure 3.4 shows w_A^D, the width of the coastal current downstream of the source region for the antisymmetric vorticity profile, plotted as a function of a. As a increases the image effect becomes stronger relative to the Kelvin-wave driven flow, and the profile approaches the vorticity-dominated limit of Johnson and McDonald [2006], where the current width is equal to twice the vortex-length L_{V}.

As noted above, the coastal current mode is only possible under certain conditions. We now derive these conditions by considering the parameter range in which (3.13) is valid.

3.2.1.1 Competitive outflows

For the moment, let us restrict ourselves to the case where the entire outflow is competitive, so that $\Pi^{\mathrm{R}} < -1/a^2$. With this condition imposed, (3.13) is valid provided $F(1)$ is real-valued, or

$$Q_+ > Q_{\mathrm{C}} = \frac{\Pi^{\mathrm{R}} + 1/2a^2}{\Pi^{\mathrm{R}} - 1}. \tag{3.14}$$

Thus, as in Kubokawa [1991] we find that the fraction of the outflow occupied by the HPVF must exceed a critical value Q_{C} in order for a steady coastal current to form. Outflows dominated by vorticity (either with large a or large $|\Pi^{\mathrm{R}}|$) require more HPVF, and a stronger cyclonic vortex, in order to form a coastal current.

The physical meaning of (3.14) can be seen by re-writing the equation in terms of source vorticity. From (3.4), ζ_S can be written as a function

of Q (equivalently the streamfunction ψ) and integrated across the source region:

$$\int_0^1 \zeta_S \, \mathrm{d}Q = Q_+ + \frac{1}{2a^2} + \Pi^{\mathrm{R}}(1 - Q_+), \tag{3.15}$$

which is positive exactly when $Q_+ > Q_{\mathrm{C}}$. That is, the coastal current mode occurs if and only if the net contribution of the source vorticity is positive. Since $\zeta_S \, \mathrm{d}Q = \zeta_S v \, \mathrm{d}x$, equation (3.15) gives the net vorticity flux out of the source. The first two terms of (3.15) are positive, and correspond to the downstream flow generated by the cyclonic part of the outflow and the Kelvin wave respectively (since the second term is the only one that depends on the Rossby radius a, and vanishes in the vorticity dominated limit of $a \to \infty$). For a steady current to form, the sum of these two must be greater in magnitude than the third term, which is negative and corresponds to the upstream flow generated by the anticyclonic part of the outflow.

3.2.1.2 Other outflows

The integral condition (3.15) suggests that previous results about coastal current formation in a QG system should be re-analysed with source vorticity in mind. In JSM, the outflow has uniform PVa, Π. They find that if $\Pi = 1$ (and so $\zeta_S > 0$ everywhere) then the coastal current mode always occurs, while if $\Pi = -1$ the coastal current mode is impossible, although other steady solutions may occur. The second case differs from our set-up since the anticyclonic portion of the outflow is on the left and there is no competition between vortices, resulting in upstream propagation even in steady flow.

In Kubokawa [1991], the outflow is split between fluid with zero PVa on the left of the source and LPVF on the right. If $a > 1$ then all of the LPVF has negative vorticity and so the outflow is competitive. In our notation, the vorticity integral becomes,

$$\int_0^1 \zeta_S \, \mathrm{d}Q = \int_0^1 \frac{Q}{a^2} \, \mathrm{d}Q + \int_{Q_0}^1 \mathrm{d}Q, \tag{3.16}$$

where Q_0 is the fraction of the outflow that has zero PVa. Equation (3.16) is positive if $Q_0 > 1 + 1/2a^2$, which agrees with the condition for coastal current formation given in (3.3a) of Kubokawa [1991].

Finally let us now consider the case where only a portion of the outflow is competitive, and the source vorticity is positive at the downstream edge (as in figure 3.2(b)). This situation occurs in the present model if $Q_+ < |a^2\Pi^{\mathrm{R}}| < 1$, in which case the competitive region is $0 < Q < |a^2\Pi^{\mathrm{R}}|$.

One can show that (3.13) is valid and the coastal current mode occurs if and only if

$$\int_0^{|a^2\Pi^{\mathrm{R}}|} \zeta_S \, \mathrm{d}Q > 0, \tag{3.17}$$

so that the critical fraction is $Q_{\mathrm{C}} = (a\Pi^{\mathrm{R}})^2/2(1-\Pi^{\mathrm{R}})$.

To summarise the results of this section, we have shown that for a competitive outflow the coastal current mode occurs if and only if the source vorticity profile satisfies an integral condition of the form (3.15). In fact, there is a simple physical interpretation of this constraint. The element $\zeta\delta Q$ represents the total amount of vorticity contained in a patch of infinitesimal area δQ with uniform vorticity ζ. Equation (3.15) shows that the plume behaves just as the sum of all of these infinitesimal patches, and turns to the right if its 'total vorticity' is positive, as if it were a cyclonic vortex of finite area. Equivalently, the coastal current mode exists if and only if the net vorticity flux from the source is positive. Non-competitive regions of the outflow do not interfere in this process and so are not counted, although of course they still influence the plume strucutre. The general nature of this condition suggests that it might have wider applicability, and an extension to $O(1)$ Rossby number is briefly discussed in appendix B. We also emphasise that the integral condition (3.15) does not depend on the specific outflow profile, but only on the relative strengths of the cyclonic and anticyclonic parts.

3.3 Numerical results

The full equations (3.1) (without the long-wave approximation) can be solved using the method of contour dynamics with surgery, which gives fast and accurate results for problems involving piecewise-constant potential vorticity [Dritschel, 1989]. In this case, the velocity field $\mathbf{u} = (u, v)$ can be written as

$$\mathbf{u}(\mathbf{x}, t) = -\sum_k \Pi_k \int_{C_k} \mathrm{K}_0 \left(|\mathbf{x} - \mathbf{x_k}|/a\right) \, \mathrm{d}\mathbf{x_k}. \tag{3.18}$$

The kernel K_0 is the modified Bessel function of the second kind of order zero, which is the appropriate Green's function for the Helmholtz equation (3.1). The sum is taken over all contours C_k, where each contour is parameterised by some $\mathbf{x_k}$ and the jump in potential vorticity between contours is given by Π_k. Once the velocity field for the (discretised) contours has been computed numerically, each contour is advected using a standard 4th-order Runge-Kutta scheme. Since the computational speed of this algorithm increases with the square of the number of discretisation points,

Dritschel [1989] further employs 'surgery', where small filaments (which do not contribute much to the dynamics) are systematically removed from the main contour. After each advective step, the discrete contours are re-noded in such a way that the resolution is proportional to the local curvature. For our particular problem involving a fixed boundary, we must modify (3.18) to account for contributions from image contours, as well as from the source itself. The contribution from each of these terms is analysed in more detail for a uniform PV outflow in Southwick et al. [2017]. Below, we present results from an initial-value problem where the source is impulsively switched on at $t = 0$, and the outflow has a uniform velocity profile $Q'(x) = 1/2$. Simulations must begin with an initial contour, for which we use a thin half-ellipse lying in the source region. Results are insensitive to the choice of initial contour, provided it is sufficiently smooth and covers the entire source.

Figure 3.5 shows a contour dynamic (CD) run for a competitive outflow in coastal current mode. The parameters are: $a = 0.8$, $Q_+ = 0.7$ and $\Pi^{\mathrm{R}} = -2$, and results are shown at, from top to bottom, $t = 15$, 30, 45. The half-width of the outflow is 3, so the long-wave parameter $\epsilon = 1/3$. The plume is shaded, with the LPVF hatched darker. Red dashed curves in the source region show the steady long-wave profiles from §3.2, which are in excellent agreement with the numerical results. The coastal current develops quickly: it is almost entirely set-up by $t = 15$ and by $t = 45$ has extended to $x = 15$. At all times the plume is led by a rarefaction consisting only of LPVF, the shape of which is derived below in §3.4.1 and plotted as a dashed red line. Between the rarefaction and the steady current there is an eruption of fluid from the coastal current into the ocean. The eruption initially grows offshore, before later curling up into an eddy that propagates downstream. In (b) and (c), the plume boundary can no longer be written as a single-valued function of x and the analytical results break down. However the cause of the eruption and its initial development can be be qualitatively understood through long-wave theory, and this is done in §3.4.2. The volume of fluid contained within the eruption increases, and eventually the eruption is strong enough that it retains all of the HPVF (and some of the LPVF) that leaves the source after a certain time. Far away from the site of the eruption the plume is unaffected, so the coastal current and rarefaction are stable features of the plume's evolution.

Figure 3.6 shows a CD run that tests the applicability of the long-wave theory to the full QG problem by using a narrow source. The parameters are the same as for figure 3.5(b), but with $\epsilon = 2$. The overall plume shape appears to be largely unaffected by using a larger value of ϵ, and

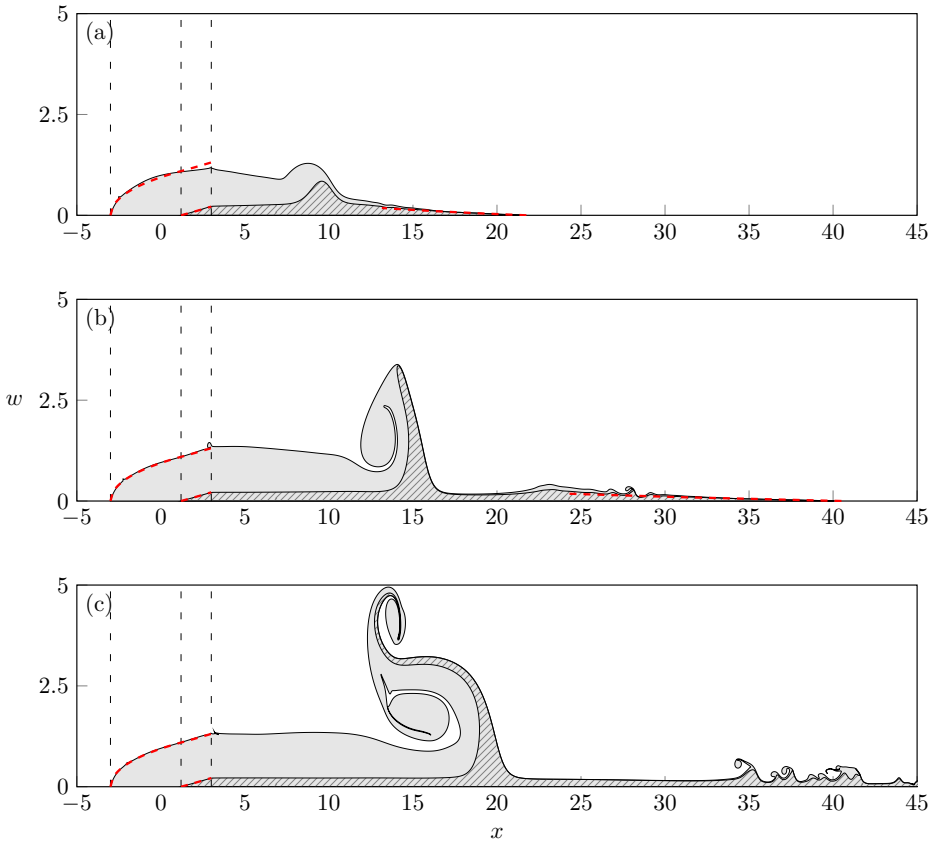

Figure 3.5: Contour dynamic results for a competitive QG outflow in coastal current mode. The speed ratio $a = 0.8$, the fraction of the outflow that has positive vorticity is $Q_+ = 0.7$ and the PV anomaly of the negative vorticity region is $\Pi^{\mathrm{R}} = -2$. The half-width of the outflow is 3, and results are shown at, from top to bottom, $t = 15$, 30, 45. In this and all subsequent figures showing contour dynamics the river plume is shaded, and the LPVF is hatched. Vertical dashed lines mark the source region and x_S, the point where the source vorticity changes sign. The red dashed lines in the source show the steady long-wave solutions from §3.2, and those at the head of the plume in (a) and (b) show the rarefaction computed in §3.4.1.

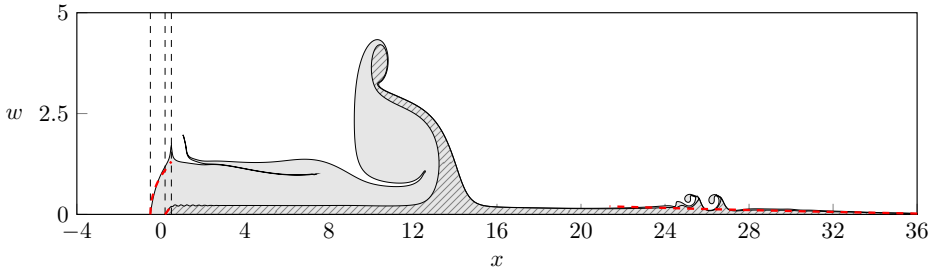

Figure 3.6: As in figure 3.5(b) but for a narrow source with half-width 0.5.

the analytic results still match the numerics very well.

Figure 3.7 shows a CD run for an outflow with an antisymmetric

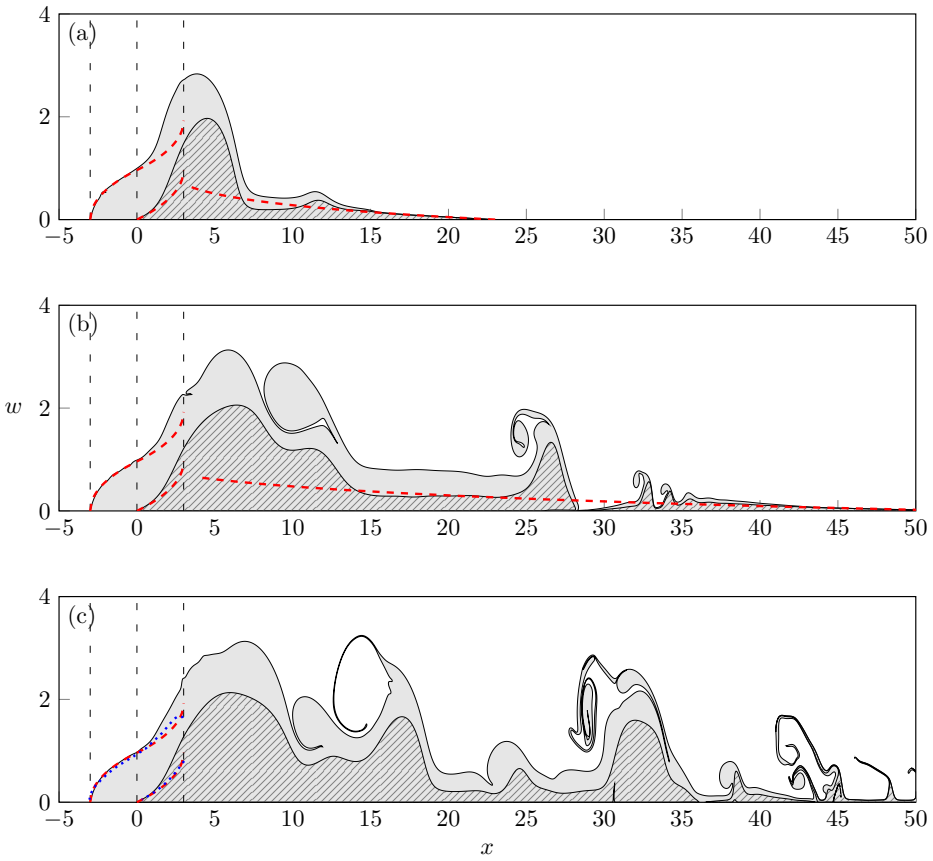

Figure 3.7: As in figure 3.5, but for an antisymmetric outflow vorticity profile. The parameters are: $a = 1$, $Q_+ = 0.5$, $\Pi^{\mathrm{R}} = -2$ and the flow is shown at $t = 20$, 50, 60. Dotted blue curves in (c) show numerically computed steady solutions to the full problem.

vorticity profile. The net contribution from the source vorticity is zero, and the condition (3.14) is at equality. The steady profile predicted by the long-wave theory is only in partial agreement with the numerics, and no constant-width current occurs. For this set of parameters, the flow immediately downstream of the source is quasi-steady, and there is a bulge of LPVF which appears trapped to the coast. At the head of the plume the rarefaction and the speed of propagation are well-captured by the long-wave theory, but nonlinear, non-periodic waves develop between the head and the bulge at later times. The antisymmetric source vorticity profile is closest to the experiments of Horner-Devine et al. [2006], where the outflow introduces an equal amount of positive and negative vorticity, so it is interesting that this is the only vorticity profile for which we observe a quasi-steady bulge downstream of the source, as is commonly seen in laboratory experiments. Figure 3.8 plots the vorticity contours at $t = 40$. The bulge has strong negative vorticity, and there is a thin

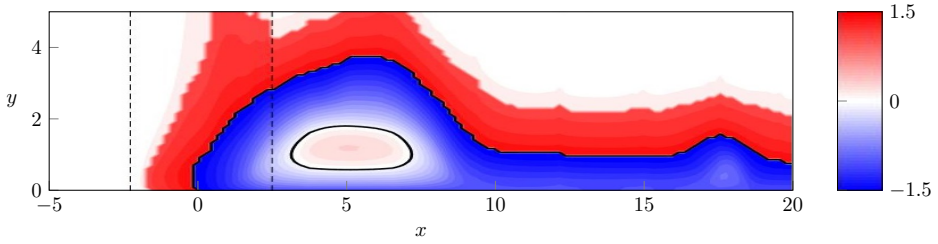

Figure 3.8: Vorticity contours for the antisymmetric outflow at $t = 40$. Black contours show $\zeta = 0$.

layer of positive vorticity around the outside. This structure is in good qualitative agreement with previous experimental results (c.f. figure 2 of Horner-Devine et al. [2006]). We note that the steep sections of the plume boundary (for example, at $x \approx 7$ in figure 3.7(a)) are in fact transient features that quickly either erupt into filaments or dissipate, and in general the plume boundary (excluding filaments) does not have steep gradients $\partial w/\partial x$.

To investigate the extent to which the long-wave approximation is responsible for discrepancies between theory and numerics, we ran two further experiments using the same antisymmetric outflow profile. First we conducted another CD run (not shown) with $\epsilon = 0.1$. The quasi-steady bulge is still present, although the steady profile agrees with the numerical results over more of the source region. We also used the iterative method described in Southwick et al. [2017] to numerically compute steady solutions to the full problem (i.e. without the long-wave approximation). These are shown as dotted blue curves in (c) and confirm that steady solutions to the full problem do exist. The stability of these solutions is discussed in the following section.

Figure 3.9 shows CD results for a competitive outflow that doesn't meet the vorticity integral condition (3.15), and so by the long-wave theory the coastal current mode is not possible. At early times fluid is directed mainly offshore (figure 3.9(a)), causing the rarefaction to narrow and eventually pinch off from the bulk. The combined effect of the Kelvin-wave flow and the image of the HPVF is not sufficient to overcome the anticyclonic part of the outflow, and the plume detaches from the coast (as in Stern and Whitehead [1990]). A similar cycle of pinch-off and re-attachment was observed by Horner-Devine et al. [2006] (their figure 14) in experiments with a low density contrast between the outflow and the ambient.

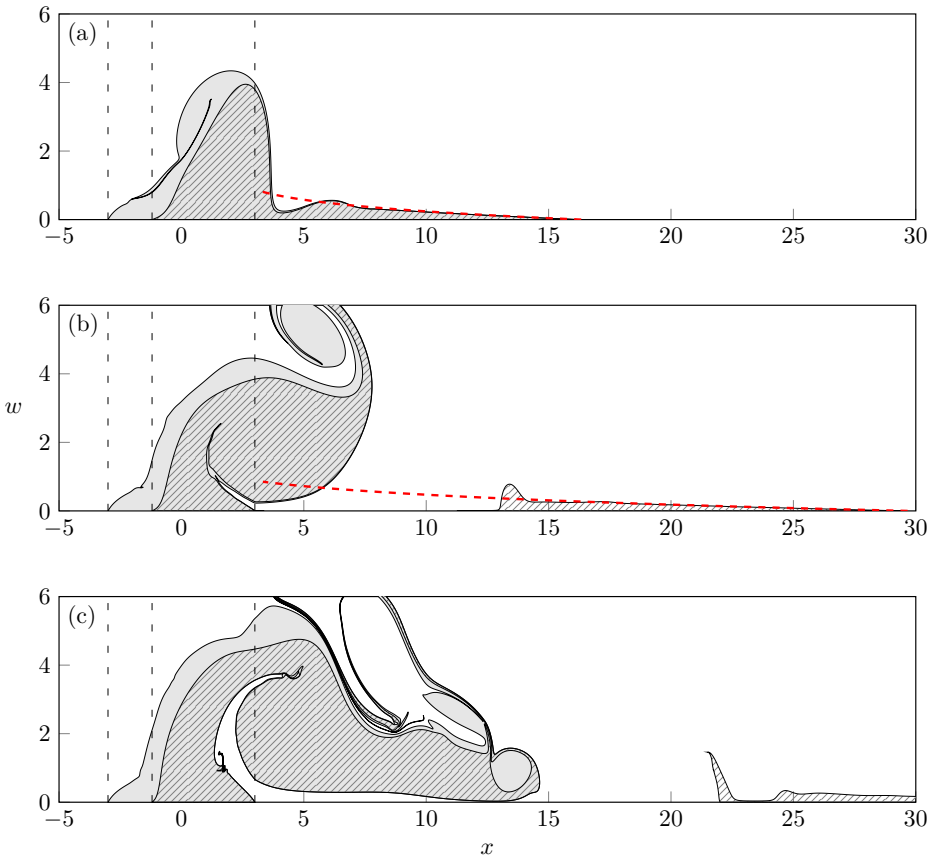

Figure 3.9: As in figure 3.5, but for an outflow where the net contribution of the source vorticity is negative. The parameters are: $a = 1.5$, $Q_+ = 0.3$, $\Pi^{\mathrm{R}} = -1$ and the flow is shown at $t = 20,\ 40,\ 60$.

3.4 Unsteady flow features

In this section, we use properties of the time-dependent long-wave equations to give a qualitative explanation for the eruptions seen in the CD results, as well as a description of the rarefaction at the plume nose. The general form of the variable coefficients in the streamfunction (3.7) is

$$\begin{aligned} A &= a^2(\Pi^{\mathrm{R}} - 1) + a^2 \cosh\left[(w_1 - w_2)/a\right] + Q_e \mathrm{e}^{-w_1/a}, \\ B &= a^2 \sinh\left[(w_1 - w_2)/a\right] - Q_e \mathrm{e}^{-w_1/a}, \\ Q_e &= Q + a^2\Pi^{\mathrm{R}} - a^2\left(\cosh\left(w_2/a\right) + (\Pi^{\mathrm{R}} - 1)\cosh\left(w_1/a\right)\right). \end{aligned}$$

The interface locations w_1 and w_2 can be found using the kinematic boundary condition

$$v = \frac{\partial w_i}{\partial t} + u\frac{\partial w_i}{\partial x} \quad \text{on } y = w_i(x,t), \tag{3.19}$$

for $i = 1, 2$. Using the fact that ψ is a streamfunction, this becomes

$$\frac{\partial w_i}{\partial t} = \frac{\partial \psi}{\partial x} + \frac{\partial \psi}{\partial y}\frac{\partial w_i}{\partial x} = \frac{\partial}{\partial x}\psi(x, w_i(x,t)), \tag{3.20}$$

where

$$\psi(x, w_1) = -a^2 + a^2 \cosh\left[(w_1 - w_2)/a\right] + Q_e \mathrm{e}^{-w_1/a}, \tag{3.21}$$

$$\psi(x, w_2) = Q_e. \tag{3.22}$$

The pair of equations (3.20) give a first-order, nonlinear hyperbolic system that is forced in the source region by the outflow velocity $Q'(x)$. In both the rarefaction and the initial development of the eruption, the system reduces to a single equation with a well-defined wave-speed that allows for a simple interpretation of the CD results.

3.4.1 Leading rarefaction

For all parameter values, there is a region of the plume close to the nose that consists only of LPVF (the 'head' region). Here there is no layer of HPVF between the LPVF and the ambient ocean so we may define $w = w_2 = w_1$. The system (3.20) reduces to a single equation for w:

$$\frac{\partial w}{\partial t} + C_R(w)\frac{\partial w}{\partial x} = 0, \tag{3.23}$$

where the wave-speed in the head region is

$$C_R(w) = \left(1/a + a\Pi^{\mathrm{R}}(1 - \mathrm{e}^{-w/a})\right)\mathrm{e}^{-w/a}. \tag{3.24}$$

At early stages the downstream plume has $\partial w/\partial x < 0$, so a self-similar rarefaction develops if $C_R'(w) < 0$ and small values of w travel faster than larger values. In fact C_R is a decreasing function for relevant values of w (i.e. between zero and the width of the coastal current) so that, as in the negative PV outflows of JSM and §2, a rarefaction always forms. The nose of the plume moves at speed $C_R(0) = 1/a$, which is just the speed of the Kelvin-wave flow. At any time t, the rarefaction shape is given by

$$x - 1 = C_R(w)(t - t_c(w)), \tag{3.25}$$

where $t_c(w)$ is the time at which the characteristic carrying that value of w emerges from the source region. JSM show that, for the special case of a uniform outflow velocity $Q'(x) = 1/2$, the crossing time $t_c = 2a(\exp(w/a) - 1)$, and so (3.25) becomes an implicit equation for w. The rarefaction solution is plotted as a red dashed line in figures 3.5 - 3.9. There is good agreement in the head region, and the nose always

propagates at the predicted speed $1/a$. Note that the preceding discussion does not require the outflow to be in coastal current mode, and indeed the long-wave theory is accurate near the nose even for the unsteady plume shown in figure 3.9.

3.4.2 Eruption from the coastal current

The long-wave theory can also be used to explain eruptions of coastal fluid into the ambient. Although eruptions are seen in all CD runs, they have different characteristics that broadly coincide with whether the net contribution of the source vorticity is positive, zero or negative. For outflows that have net positive source vorticity, the eruption propagates downstream and ejects a filament of river water into the ocean. In figure 3.7, where the source vorticity is antisymmetric, the eruption is bounded and a bulge of LPVF is retained near the source. Finally, if the net contribution from the source vorticity is negative and outflows are not in coastal current mode, then the eruption occurs within the source region. During the early stages of eruption (for example in figure 3.5(a)) w_1 and w_2 are displaced by approximately the same amount, so as a first approximation we may consider the characteristic equations (3.20) with $w_2 = w_1 + w_0$, where the constant w_0 is given by the steady profile (3.9) as

$$w_0 = a\,\mathrm{acosh}\left(1 + Q_+/a^2\right). \tag{3.26}$$

With this substitution, the wave-speed is

$$C_E(w_1) = \frac{1}{a}\Big(1 + a^2\Pi^{\mathrm{R}}(1 - \mathrm{e}^{-w_1/a}) \\ +(\sqrt{Q_+(2a^2 + Q_+)} - Q_+)\mathrm{e}^{-w_1/a}\Big)\,\mathrm{e}^{-w_1/a}, \tag{3.27}$$

which is similar to (3.24) apart from an extra term due to interaction between LPVF and HPVF. Since values of w_1 are conserved along curves moving at speed $\mathrm{d}x/\,\mathrm{d}t = C_E(w_1)$, the initial movement of the eruption is downstream if C_E is positive. For antisymmetric outflows where $Q_+ = 1/2$ and $\Pi^{\mathrm{R}} = -1 - 1/a^2$, the wave-speed C_E vanishes at the downstream edge of the source causing disturbances to become trapped. A similar situation is discussed in Johnson and Clarke [1999] in the context of hydraulic control, where they show that a vanishing wave-speed leads to a build up of momentum and prevents steady long-wave profiles from being realised in the CD simulations. This can be understood by considering a small perturbation $\delta(x,t)$ to the steady flow w_1^S. To first order, the kinematic boundary condition (3.20) becomes

$$\delta_t = \left[\psi(w_1^S) - C_E(w_1^S)\delta\right]_x = -\left(C_E(w_1^S)\delta\right)_x, \tag{3.28}$$

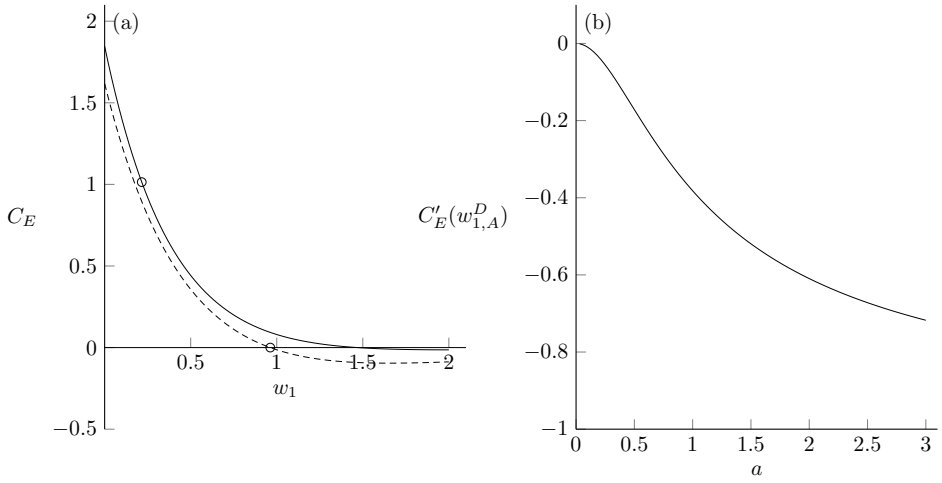

Figure 3.10: (a) The long-wave speed (3.27) during the early stages of an eruption. The solid line uses the same parameters as the coastal current mode of figure 3.5; and the dashed line uses the same as the antisymmetric profile of figure 3.7. Circles mark the downstream width of the steady profile. (b) The slope of C_E at the downstream width $w^D_{1,A}$ for antisymmetric profiles, as a function of a.

using the fact that in steady flow $\psi(w_1^S) = Q_+$ is constant. Multiplying (3.28) by C_E shows that the perturbation momentum $C_E\delta$ is conserved and so as $C_E \to 0$ the amplitude δ becomes arbitrarily large. Therefore, in an outflow where the net contribution of the source vorticity is zero, the steady long-wave profiles of §3.2 are unstable to small perturbations and so will never be seen in the initial value problem.

Figure 3.10(a) shows two representative examples of $C_E(w_1)$ corresponding to the CD runs presented in §3.3, with the coastal current mode of figure 3.5 shown as a solid curve and the antisymmetric outflow of figure 3.7 as a dashed curve. The maximum width of w_1^S is marked with a circle. Both curves have a negative gradient, so any perturbation to steady flow will steepen on the upstream side as smaller values of w_1 move faster. However note that for the antisymmetric profile the curve flattens as w_1 increases, so $\partial w_1/\partial x$ remains $O(1)$ and the eruption in figure 3.7 is bounded. On the other hand the solid curve corresponding to figure 3.5 is positive at the downstream edge and has a steeper gradient, so the eruption propagates downstream and is relatively strong, as is discussed in Stern [1986]. To further examine bulge formation in antisymmetric outflows, figure 3.10(b) plots the slope of C_E at the downstream edge of the source. As a increases and vorticity becomes more dominant, $|C'_E(w_{1,A})|$ is larger and nonlinear wave steepening is stronger, so that the eruption is no longer bounded. Thus, in the QG model, it seems that quasi-steady bulges can only exist in antisymmetric outflows where vortical effects are relatively weak.

We briefly consider the behaviour of the outflow in figure 3.9, where the net contribution from the source vorticity is negative and the coastal current mode is not possible. Instead, the profile given by equation (3.13) is only valid over part of the source region, with the radical vanishing and $F(Q)$ becoming complex at $Q = 0.73$. Differentiating (3.13) gives

$$\frac{\partial w_1}{\partial x} = \frac{a\ Q'(x)}{\sqrt{(Q^2 + 2a^2(\Pi^{\mathrm{R}}(Q - Q_+) + Q_+))}}, \tag{3.29}$$

so that the loss of the steady solution is associated with an infinite gradient in the profile and, as in Stern [1986], a strong eruption of coastal fluid that here detaches completely from the coast.

3.5 Discussion

Numerical and theoretical results for coastal outflows have been discussed in terms of a quasi-geostrophic model which allows for complete control over the source vorticity profile by specifying the PV distribution of the expelled fluid. This is the key feature of the model, as it gives insight into the relationship between the vorticity of the outflow and the resulting plume structure. In particular, we are interested in the case of a 'competitive outflow', where negative vorticity is on the right of the source and positive vorticity is on the left, as in this situation the image effect imparts a tendency for cyclones and anticyclones to pass through each other. Analytical steady solutions to the long-wave equations have been derived, and it is shown in §3.2 that the coastal current mode is only possible if the net contribution of the source vorticity (the integral of ζ with respect to the streamfunction ψ over competitive regions of the outflow) is positive. It is encouraging that the results from Kubokawa [1991] agree with our, more general, condition on the outflow. Kubokawa's results do not depend on the long-wave approximation and so this suggests that the source vorticity condition is applicable even when $\epsilon = O(1)$.

The numerical results of §3.3 confirm that when the region of cyclonic vorticity is dominant all fluid turns to the right after leaving the source (figure 3.5) and a stable coastal current develops. The plume nose consists entirely of LPVF and propagates at the speed of the Kelvin-wave driven flow, Q_0/L_{R} (where Q_0 is the area flux of the outflow). The head of the intrusion is a self-similar rarefaction, which can be described by long-wave theory. If the net contribution of source vorticity is negative, the anticyclonic region is dominant and the coastal current mode is not possible. The plume cannot remain attached, and separates from the

coast as it leaves the source (figure 3.9). The transition case, where the cyclonic and anticyclonic contributions cancel, is closest to the laboratory experiments of Avicola and Huq [2003b] and Horner-Devine et al. [2006]. A steady long-wave profile exists but it is unstable to small perturbations and, depending on the value of a, the plume can develop a quasi-steady bulge just downstream of the source (figure 3.7). The bulge forms due to the accumulation of short-wave energy, and appears to reduce the downstream transport of LPVF. It is notable that these features are only seen in runs where the net vorticity is zero.

3.5.1 Oceanographic context

Avicola and Huq [2003b] and Chen [2014] show that fluid from the right-hand side of the outflow tends to gather in the bulge, so that both the sign and the distribution of source vorticity play a role in the initial development of the plume and therefore contribute to the overall structure. In situ measurements of plume vorticity are rare, particularly in the source region, although there is much evidence that where bulges exist they are anticyclonic (for example figure 5 of Chant et al. [2008]). The work in this chapter has therefore been guided by laboratory plumes and, despite the simplicity of the model, has reproduced many of their qualitative features, with a bulge core that consists of negative vorticity and a thin layer of positive vorticity at the plume boundary and in the coastal current (figure 3.8). While laboratory outflows can be assumed to be competitive, the same may not always be true in the real oceans. For example, Münchow and Garvine [1993b] show that the source velocity profile of the Delaware river features landward flow on the left-hand side of the estuary, so that the vorticity is cyclonic throughout. (The Delaware plume forms a coastal current, which is consistent with a cyclonic outflow.)

In the present model, the coast is a vertical wall and so topography has no effect on the behaviour of the plume. In the real oceans, the slope of the continental shelf plays a role in determining whether a bulge forms or not. Yankovsky and Chapman [1997] shows that plumes are 'surface-advected' (and hence little-affected by topography) when $2WVf/g' > H_s$, where V is a scale for the outflow velocity. In bottom-advected plumes, i.e. those that do not satisfy this inequality, topography induces further stretching of fluid columns and thus increases transport to the coastal current. Vorticity generated by topographic stretching increases the net vorticity of the outflow and could in principle be incorporated into the right-hand side of (3.15), although this would be complicated by the fact

that the contribution from topographic stretching depends on the off-shore location of the plume boundary. As in most numerical and laboratory studies, we have modelled the river mouth as a rectangular opening normal to the coast. Garvine [2001] and Avicola and Huq [2003b] explore the effect of varying the geometry of the inlet, and find that bulge formation can be suppressed by angling the inlet so that fluid is directed downstream, or by increasing the radius of curvature at the inlet corners. Both of these results can be understood by considering the plume path as an inertial circle which is able to remain attached to the coast when guided to do so by the geometry. However this inertial framework ignores vortex effects and predicts that a gyre will always form when the corners of the river mouth are sharp. The QG model is in the alternative limit, where the inertial radius V/f is small compared to the chosen length-scale and vorticity dynamics are dominant. A more nuanced theoretical treatment of the problem, which includes contributions from both inertia and vorticity, is an important avenue for future work.

Chapter 4

The potential-vorticity dynamics of coastal fronts

This chapter studies the propagation of free, long waves on a potential vorticity front in the presence of a vertical coast, using a uniform-PV, QG model introduced by Pratt and Stern [1986]. PV fronts have been used to model the centre-line of a thin ocean jet [Nycander et al., 1993, Cushman-Roisin et al., 1993], as well as Western Boundary Currents such as the Gulf Stream [Pratt et al., 1991, Sasaki and Schneider, 2011a]. We also have in mind topographic PV gradients, and this will be explored further in the following chapter. Although Pratt and Stern developed the present model in a general form that includes a coast, the specific examples that they present are mostly concerned with free fronts (i.e. those without a coast) in which the only wave is the Rossby wave. The purpose here is to highlight how waves on PV fronts are affected by coastal dynamics; i.e. Kelvin-wave flow and image vorticity (see §4.1.1 for a further discussion of how the present model relates to Pratt and Stern's). We show that the richest behaviour, which includes compound-wave structures and kink solitons, occurs in the regime where vortical effects are dominant. We further extend Pratt and Stern's work by using a recently-developed analytical technique known as 'dispersive shock-fitting' [El, 2005] to classify and interpret the behaviour of the model when first-order dispersive effects are included. The dynamics of the resulting equation are similar to those of the modified KdV, a connection that has previously been noted in theoretical studies

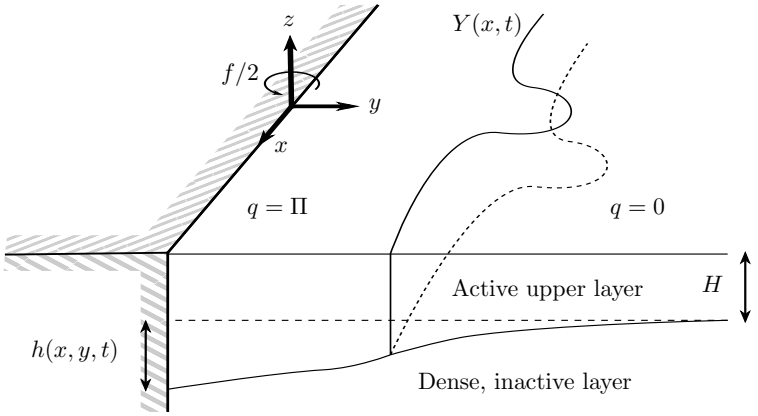

Figure 4.1: A coastal current occupies the region $0 < y < Y(x,t)$. The current has uniform potential vorticity, $q = \Pi$, and the ambient upper layer has uniform potential vorticity $q = 0$. Both the current and the upper layer lie above a deep, inactive, denser layer. Variables are non-dimensional, with the relevant scales defined below.

of free fronts [Nycander et al., 1993]. Contour-dynamic simulations show that the dispersive long-wave theory captures the behaviour of the full quasi-geostrophic system to a high degree of accuracy.

Section 4.1 develops the mathematical model and the governing equations in the long-wave limit; §§4.2, 4.3 discuss the leading-order and first-order long-wave equations respectively, including the application of the dispersive shock-fitting algorithm in §4.3; §4.4 presents numerical results to both the long-wave and full quasi-geostrophic equations, and considers dispersive compound-wave structures, and §4.5 discusses applications of the model, and compares results with previous studies.

4.1 Model and governing equations

Consider flow in the half-space $y > 0$, with a vertical, impermeable wall at $y = 0$. The flow is described by a Cartesian co-ordinate system $Oxyz$, which is fixed in a frame of reference that rotates at speed $f/2 > 0$ about the vertical axis Oz. The flow consists of an upper layer of density ρ_1, lying below a rigid top at $z = 0$ and above an inactive, infinitely-deep layer of density ρ_2, with $\rho_1 < \rho_2$ and the difference sufficiently small that the Boussinesq approximation applies. The perturbation of the interface about the mean depth H is denoted $h(x,y,t)$. A schematic of this set-up is shown in figure 4.1. If $h \ll H$, then the flow can be described by the quasi-geostrophic equation for the conservation of potential vorticity:

$$\frac{\mathrm{D}}{\mathrm{D}t}\left(\nabla^2\psi - \frac{1}{L_{\mathrm{R}}^2}\psi\right) = 0. \tag{4.1}$$

Here, $L_{\mathrm{R}} = \sqrt{(g'H)}/f$ is the Rossby radius of deformation for the upper layer, g' is the reduced gravity, and the streamfunction $\psi = g'h/f$ is related to the velocity by $(u, v) = (-\psi_y, \psi_x)$. The conserved quantity in (4.1) is q, the quasi-geostrophic PV (i.e. the perturbation potential vorticity due to the departure from the mean value f/H, multiplied by H). In the present model q is taken to be piecewise constant, with $q = \Pi_0$ in the coastal current and $q = 0$ in the ambient fluid. The front that separates the coastal current from the ambient is a material contour $\Gamma(t)$, knowledge of which is sufficient to determine the entire flow-field at that time.

The no-flux boundary condition at $y = 0$ requires that

$$\psi(x, 0, t) = Q_0 \tag{4.2a}$$

is constant, while in the far-field the fluid is stationary:

$$\psi \to 0 \text{ as } y \to \infty. \tag{4.2b}$$

Thus the net flux in the upper layer is $Q_0 H$. If $Q_0 > 0$, the net flux is rightwards (facing seawards) and the interface is deeper at the coast than far offshore, as in an outflow plume. Although in the remainder of this chapter we assume that $Q_0 > 0$, the alternative setting with a net leftward flux and a shallower interface at the coast may be obtained through the transformation

$$\psi \to -\psi, \quad x \to -x, \quad \Pi \to -\Pi. \tag{4.3}$$

The interaction between coastal currents with $Q_0 < 0$ and shelf waves is the topic of §5. The third possibility with $Q_0 = 0$ is not considered here but is discussed briefly in Pratt and Stern [1986]. As in §3 the boundary condition (4.2a) with $Q_0 > 0$ also represents the signature of the Kelvin wave in the QG limit, which we will refer to simply as the 'Kelvin-wave flow'.

We will briefly assess the relevance of the quasi-geostrophic limit to the present problem (although note that the interaction between coastal phenomenon and Rossby-wave dynamics that is fundamental to this work also applies in the full shallow-water equations [Nycander et al., 1993]). For the quasi-geostrophic limit to apply, we require that $h \ll H$, $\mathrm{Ro} \ll 1$ and consequently L is not orders of magnitude larger than L_{R}, where L is the chosen length scale for the problem. The first of these restricts us to currents where the displacement of the upper layer from its mean value is on the order of metres. Below we will non-dimensionalise horizontal lengths with L_{V}, so that the length-scale restriction imposes $a = O(1)$. Following the estimates given in §1.4 this requires that the velocity scale U is $O(0.1 - 1\mathrm{m\,s^{-1}})$, which is reasonable for most coastal currents.

4.1.1 Scaling of horizontal lengths

As pictured in figure 4.1, the problem of a coastal PV front has four relevant horizontal length-scales. These are: L_{R}, the Rossby radius of deformation; Y_∞, the mean distance of the PV front from the coast; λ, the typical wavelength of a frontal meander; and $L_{\mathrm{V}} = (Q_0/|\Pi_0|)^{1/2}$, which is the so-called vortical length-scale. The latter of these is the appropriate scaling for a current of flux Q_0 and relative vorticity $|\Pi_0|$ in two-dimensional flow [Johnson and McDonald, 2006]. The quasi-geostrophic model used for numerical simulations below assumes that all four lengths are of order unity, while the long-wave limit in which the analysis is performed formally requires

$$\lambda \gg (Y_\infty, L_{\mathrm{R}}, L_{\mathrm{V}}), \tag{4.4}$$

with Y_∞, L_{R} and L_{V} all of the same order. By contrast, the free-front problem (i.e. without a coast) considered by Pratt [1988] and Nycander et al. [1993] assumes that

$$Y_\infty \gg \lambda \gg (L_{\mathrm{R}}, L_{\mathrm{V}}). \tag{4.5}$$

Thus the present model explores a different asymptotic regime to that considered by Pratt [1988] and Nycander et al. [1993], one in which $Y_\infty \sim L_{\mathrm{R}}$ and coastal effects enter at leading order. Some examples of PV fronts in the real oceans that may fall into this regime include the flow down Barrow Canyon [Pickart et al., 2005], the Kuroshio south of Japan [Tsujino et al., 2006], and the Western Arctic shelfbreak jet [Spall et al., 2008]. Further discussion of the oceanographic context for this model is given in §§4.5-6.

Horizontal lengths are non-dimensionalised on L_{V}. This introduces the non-dimensional Rossby radius $a = L_{\mathrm{R}}/L_{\mathrm{V}}$, which measures the relative strengths of the Kelvin-wave flow and image vorticity and plays an important role in what follows. When $a < 1$ the flow is Kelvin-wave dominated, while $a > 1$ corresponds to vorticity-dominated flow. The parameter Q_0, which represents the net flux in the upper layer, can be scaled out by replacing ψ with $Q_0\psi$. Speeds are non-dimensionalised by Q_0/L_{V}, and time t on the advective scale L_{V}^2/Q_0. With these choices, the natural scaling for Π_0 is $Q_0/L_{\mathrm{V}}^2 = |\Pi_0|$ so that the non-dimensional PV in the coastal current is $q = \mathrm{sign}\,(\Pi_0)$, which we will denote Π. We therefore categorise the coastal current according to the sign of its PV anomaly (PVa), with $\Pi = 1$ (positive PVa) meaning that the coastal current is of higher PV than the ambient and $\Pi = -1$ (negative PVa) meaning that the coastal current has lower PV. In currents with positive PVa, the

image effect reinforces the Kelvin-wave driven flow, while in currents with negative PVa the two effects oppose each other. In the analysis below we assume that $\Gamma(t)$ does not overturn, and so we may introduce $y = Y(x,t)$ as the location of the PV front. With these scalings and this assumption, the governing equation is:

$$\nabla^2\psi - \psi/a^2 = \begin{cases} 0 & y > Y(x,t), \\ \Pi & 0 < y < Y(x,t). \end{cases} \tag{4.6}$$

Thus the model contains two free parameters: the non-dimensional Rossby radius a, which is assumed to be $O(1)$, and $\Pi = \pm 1$ which indicates the sign of the PV gradient. The system (4.6) is closed by the kinematic boundary condition,

$$\frac{\mathrm{D}}{\mathrm{Dt}}(y - Y) = 0 \quad \text{at } y = Y, \tag{4.7a}$$

or, using the fact that ψ is a streamfunction,

$$Y_t = \left[\psi(x, Y(x,t))\right]_x, \tag{4.7b}$$

so that all of the dynamics can be described by a scalar equation (4.7b) for $Y(x,t)$.

4.1.2 The long-wave limit

The fully nonlinear, free-boundary problem (4.1) can be solved numerically using the method of contour dynamics [Dritschel, 1988]. This is done below in §4.4.4, where dispersive shock-waves (DSWs) and compound-wave structures are shown to occur in simulations where the initial frontal displacement $Y(x,0)$ is a smoothed step (although DSWs can arise from a wide variety of initial conditions – see figure 5 of Pratt [1988]). In order to analyse these structures, we will now assume that the flow is slowly-varying in the along-shore direction. That is, we formally re-scale x and t by $\epsilon = \lambda^{-1}$, where $\lambda \gg 1$ is a typical wavelength for the front. As we will see later, the long-wave theory accurately predicts the behaviour of the full system even for the most extreme case of the Riemann problem, where the initial condition is discontinuous. We expand ψ as a power-series in ϵ:

$$\psi(X, y, T) = \psi^0 + \epsilon^2\psi^1 + O(\epsilon^4), \tag{4.8}$$

where $X = \epsilon x$ and $T = \epsilon t$ are the long-wave variables. The field equation for the leading-order term ψ^0 is

$$\psi^0_{yy} - (1/a^2)\psi^0 = \begin{cases} 0 & y > Y(X,T), \\ \Pi & 0 < y < Y(X,T), \end{cases} \tag{4.9}$$

which is to be solved subject to the boundary conditions (4.2) and the requirement that ψ and u are continuous at the front $y = Y$. The solution is

$$\psi^0(X,y,T) = \begin{cases} (1+a^2\Pi)\mathrm{e}^{-y/a} - \dfrac{a^2\Pi}{2}\left[\mathrm{e}^{(Y-y)/a} + \mathrm{e}^{-(y+Y)/a}\right] & y > Y, \\ -a^2\Pi + (1+a^2\Pi)\mathrm{e}^{-y/a} & \\ \qquad + \dfrac{a^2\Pi}{2}\left[\mathrm{e}^{(y-Y)/a} - \mathrm{e}^{-(y+Y)/a}\right] & 0 < y < Y. \end{cases} \tag{4.10}$$

The ratio y/a that appears in (4.10) and elsewhere is, in dimensional terms, y^*/L_R where y^* is the dimensional co-ordinate. Thus as usual the Rossby radius L_R is the intrinsic decay scale in the problem. At $Y(X,T)$ we have

$$\psi^0(X,Y,T) = Q_e(X,T) = -\frac{a^2}{2}\Pi + (1+a^2\Pi)\mathrm{e}^{-Y/a} - \frac{a^2}{2}\Pi\mathrm{e}^{-2Y/a}, \tag{4.11}$$

where $Q_e(X,T)$ gives the net transport of ocean fluid at any station X, and thus $1 - Q_e$ is the transport in the coastal current. Note that (4.7b) is written in flux form so that, in the language of scalar conservation laws, $-Q_e$ is the flux function for the long-wave equation.

The evolution of the front is governed by the kinematic boundary condition (4.7) which, using (4.11), is:

$$Y_T + \left[\left(\frac{1}{a} + a\Pi\right)\mathrm{e}^{-Y/a} - a\Pi\mathrm{e}^{-2Y/a}\right] Y_X = 0. \tag{4.12}$$

Equation (4.12) is an unforced nonlinear wave equation that governs the leading-order behaviour of long waves on a coastal PV front. By analogy with open-channel flow, we call this the 'hydraulic limit' [Pratt and Whitehead, 2008]. In general, smooth initial conditions may develop shocks at finite time, so that the long-wave assumption no longer holds. This is resolved by introducing a next-order, dispersive correction to the field equation (4.9). The hydraulic limit is discussed further in §4.2.

4.1.3 Dispersive effects

At the next order in ϵ, the field equation is

$$\psi^1_{yy} - (1/a^2)\psi^1 = -\psi^0_{XX}. \tag{4.13}$$

The solution to (4.13) that satisfies the far-field condition (4.2b) and the boundary condition $\psi^1(X,0,T) = 0$ may be written

$$\psi^1(X,y,T) = \begin{cases} \left(\dfrac{ay}{2}\left[Q_e\mathrm{e}^{Y/a}\right]_{XX} + A\right)\mathrm{e}^{-y/a} & y > Y, \\ -\dfrac{a^3 y}{4}\Pi\left[\mathrm{e}^{-Y/a}\right]_{XX}\left(\mathrm{e}^{y/a} + \mathrm{e}^{-y/a}\right) & \\ \qquad + B\sinh(y/a) & 0 < y < Y, \end{cases} \tag{4.14}$$

where $A(X,T)$ and $B(X,T)$ are determined by continuity of ψ^1 and u^1 at $y = Y$ to be

$$\begin{aligned} B(X,T) &= \frac{a^2}{2}\left[Q_e \mathrm{e}^{Y/a}\right]_{XX} \mathrm{e}^{-2Y/a} + \frac{a^4}{4}\Pi\left(1 + \frac{2Y}{a} + \mathrm{e}^{-2Y/a}\right)\left[\mathrm{e}^{-Y/a}\right]_{XX} \\ &= \frac{a}{2}\Pi \mathrm{e}^{-Y/a}\left(YY_X^2 - a(a+Y)Y_{XX}\right), \end{aligned} \tag{4.15}$$

$$A(X,T) = \frac{a}{2}\Pi\left(aYY_{XX}\cosh\left(Y/a\right) + \left(YY_X^2 - a^2 Y_{XX}\right)\sinh\left(Y/a\right)\right). \tag{4.16}$$

Thus the dispersive correction to (4.11) is (c.f. §2.2.2 in Johnson et al. [2017]):

$$\psi^1(X,Y,T) = \frac{-a^3}{4}\Pi Y_{XX} + \left(\frac{a^2}{2}\Pi Y Y_{XX} + \frac{a^3}{4}\Pi Y_{XX} - \frac{a}{2}\Pi Y Y_X^2\right)\mathrm{e}^{-2Y/a}, \tag{4.17}$$

and the kinematic boundary condition governing the evolution of the PV front is

$$\begin{aligned} &Y_t + \left[(1/a + a\Pi)\exp\left(-Y/a\right) - a\Pi\exp\left(-2Y/a\right)\right]Y_x + \frac{a^3}{4}\Pi Y_{xxx} \\ &- \Pi\left(\left(Y - \frac{a}{2}\right)(Y_x)^3 + \frac{a^3}{4}Y_{xxx} + \frac{a^2}{2}YY_{xxx} - 2aYY_xY_{xx}\right)\mathrm{e}^{-2Y/a} = 0, \end{aligned} \tag{4.18}$$

where for convenience we have returned to the original variables x and t. The study of the third-order, dispersive, nonlinear wave equation (4.18) is the main focus of this chapter. The fact that ϵ does not appear explicitly in these equations is typical [Johnson and Clarke, 1999], although formally (4.18) requires that variations in x are slow. In practice, however, we find that the dispersive long-wave equation captures much of the behaviour of the full problem (4.1). This is shown below in §4.4.4.

Multiplying (4.18) through by Y, one obtains the following conservation law, which will be necessary later for the treatment of the Riemann problem:

$$\begin{aligned} &\left(\frac{Y^2}{2}\right)_t + \left[\frac{a^2\Pi}{4}(2Y+a)\mathrm{e}^{-2Y/a} - (Y+a)(1+a^2\Pi)\mathrm{e}^{-Y/a}\right]_x \\ &+ \frac{a^3\Pi}{8}\left[(Y_x^2 - 2YY_{xx})\left(\left(1 + \frac{2Y}{a}\right)\mathrm{e}^{-2Y/a} - 1\right) + \left(\frac{2Y}{a}Y_x\right)^2\mathrm{e}^{-2Y/a}\right]_x \\ &= 0. \end{aligned} \tag{4.19}$$

Note that the square-bracketed terms in (4.19) are grouped according to whether they are derived from ψ^0 or ψ^1— that is, according to their asymptotic order in ϵ.

4.2 The hydraulic equation

Here, we discuss solutions to the hydraulic equation (4.12) using the particular example of the Riemann problem. The classification and description of the range of behaviours should be viewed as a paradigm for the evolution of the front from more general initial conditions.

In the hydraulic limit, the evolution of the front is governed by the nonlinear wave equation (4.12). Values of Y are conserved on characteristic curves satisfying $\mathrm{d}x/\mathrm{d}t = C(Y)$, where the long-wave speed $C(Y)$ is given by

$$C(Y) = \left(\frac{1}{a} + a\Pi\right)\mathrm{e}^{-Y/a} - a\Pi\mathrm{e}^{-2Y/a}. \tag{4.20}$$

Note that $C(Y)$ is negative if

$$Y < Y_1 = a\log\left(\frac{a^2}{a^2+\Pi}\right), \tag{4.21}$$

where $Y_1 > 0$ only if $a > 1$ and $\Pi = -1$. Thus disturbances can only propagate upstream if the current has negative PVa and image vorticity dominates the Kelvin-wave flow.

As in Pratt and Stern [1986], long-wave disturbances to a free front are stationary ($C(Y) \to 0$ as $Y \to \infty$). Therefore $C(Y)$ has no contribution from vortex induction, and in the hydraulic limit the only relevant effects are the Kelvin-wave flow and image vorticity. When $a > 1$ the long-wave speed $C(Y)$ is non-monotonic, with a turning point at

$$Y_2 = a\log\left(\frac{2a^2}{a^2+\Pi}\right), \tag{4.22}$$

which is thus also the inflection point for the flux function Q_e. Compound-wave structures (shock-rarefactions) are therefore possible when $a > 1$, and the vortically-dominated regime contains the richest behaviour.

4.2.1 The Riemann problem for the hydraulic equation

In the Riemann problem, the initial conditions are given by the step

$$Y(x,0) = \begin{cases} Y_- & x < 0, \\ Y_+ & x > 0. \end{cases} \tag{4.23}$$

First, suppose that the interval of the initial step does not contain Y_2. The step is resolved by a 'simple-wave structure'; that is, a shock or a rarefaction. If $C(Y_+) > C(Y_-)$, characteristic curves separate and the space

between them in the (x,t)-plane is filled by an expansion fan (rarefaction). The rarefaction is given by

$$\frac{x}{t} = C(Y) \quad \text{for} \quad C_- < \frac{x}{t} < C_+, \tag{4.24}$$

where we have defined $C_\pm = C(Y_\pm)$. The rarefaction connects smoothly to the far-field solution $Y = Y_\pm$.

If the initial step (4.23) has $C_+ < C_-$, characteristic curves collide and a shock forms. The speed of the shock, V_s, is given by the Rankine-Hugoniot condition for (4.7b):

$$V_\mathrm{s}(Y_+, Y_-) = \frac{Q_e(Y_-) - Q_e(Y_+)}{Y_+ - Y_-}. \tag{4.25}$$

Characteristic curves must transfer information into the shock from both sides, so that V_s is required to satisfy the 'entropy' condition

$$C_+ \le V_\mathrm{s} \le C_-. \tag{4.26}$$

The geometric interpretation of this restriction is that V_s is the slope of the chord connecting $Q_e(Y_\pm)$ and, since $C(Y) = -Q_e'(Y)$, the entropy condition requires that the chord does not intersect the graph of Q_e. The entropy condition is satisfied if Q_e is convex over the interval containing $Y_\pm$, i.e. the interval does not contain Y_2. If the entropy condition is not satisfied, then the initial step is resolved through a compound shock-rarefaction in which the two far-field states $Y_\pm$ are connected through an intermediate value Y_M. The details of this depend on which of the inequalities in (4.26) fails to hold.

1. If $V_\mathrm{s} > C_-$, a shock connects Y_+ to Y_M, where Y_M is chosen so that $V_\mathrm{s}(Y_+, Y_M) = C(Y_M)$. Since $C(Y_M) > C_-$, these two levels may be connected by a rarefaction.

2. If $V_\mathrm{s} < C_+$, the shock connects Y_- to Y_M, where $V_\mathrm{s}(Y_M, Y_-) = C(Y_M)$. A rarefaction connects Y_M and Y_+.

Initial steps where $C_+ > C_-$ but Y_2 lies within the interval containing $Y_\pm$ are resolved similarly.

Figure 4.2 shows a numerical simulation of the hydraulic equation (4.12) with $a = 1.25$, $\Pi = -1$ and an initial step chosen so that the entropy condition (4.26) is not satisfied. Starting from a smoothed step, the equation is integrated from $t = 0$ using the Lax–Wendroff method with Neumann boundary conditions at either end of the computational domain. The solution Y is plotted at $t = 1000$ as the solid curve in figure 4.2(b). The dashed curve shows the initial step, translated in x by $1000V_\mathrm{s}$ for

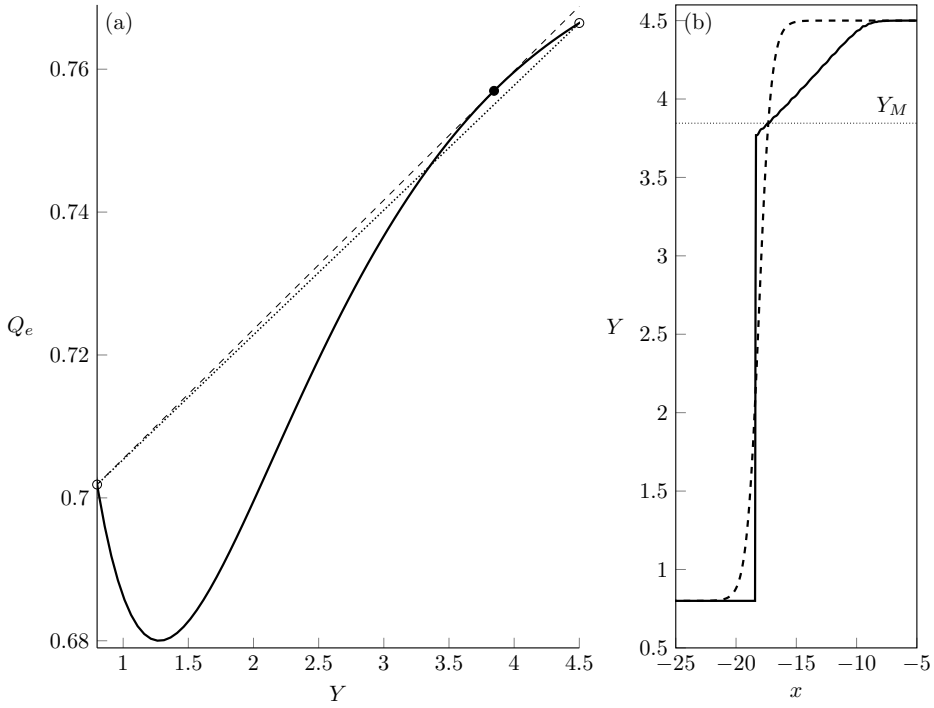

Figure 4.2: A compound-wave solution to the Riemann problem in the hydraulic limit. The parameters are $a = 1.25$, $\Pi = -1$, and the initial step goes from $Y_- = 0.8$ to $Y_+ = 4.5$. (a): The flux function $Q_e(Y)$. Open dots show $Y_\pm$, and the filled dot is Y_M. The dashed line is the chord joining Y_- to Y_M, and the dotted line is the chord joining Y_- to Y_+, which intersects the curve and does not satisfy the entropy condition (4.26). (b): The location of the front, Y, at $t = 1000$ (solid curve) and the initial condition (dashed curve) translated in x for ease of comparison.

ease of comparison. The shock-rarefaction structure is clear, with the front steepening for $Y < Y_M$ and relaxing to a rarefaction for $Y > Y_M$, where $Y_M = 3.85$ is given by the horizontal dotted line. The geometric viewpoint is illustrated in figure 4.2(a), which shows the flux function $Q_e(Y)$. The dotted line represents a shock propagating at $V_s(Y_+, Y_-)$, and intersects the curve $Q_e(Y)$ at $Y \approx 3.5$. This shock would therefore fail to satisfy the entropy condition (4.26). Instead the solution develops a shock that joins Y_- with the intermediate value Y_M, chosen so that the shock speed $V_s(Y_M, Y_-)$ (dashed line in (a)) is tangential to Q_e at Y_M. Thus, Y_M is the maximum off-shore distance of a front that can connect to $Y_- = 0.8$ via a shock.

Figure 4.3 shows the classification diagram for the resolution of an initial step in terms of the parameters Y_+ and Y_-. Shaded regions of the diagram correspond to initial steps that are resolved by a shock, white regions to steps that are resolved by a rarefaction, and striped regions

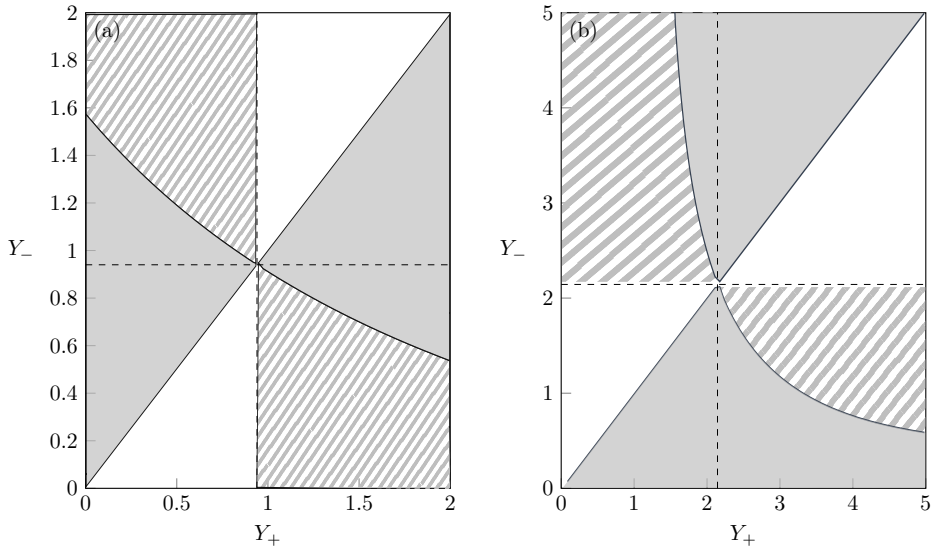

Figure 4.3: Diagram showing the resolution of the Riemann problem for (a) $a = 2$, $\Pi = 1$ and (b) $a = 1.25$, $\Pi = -1$. In both cases, the dashed lines mark Y_2. Shaded regions show where the initial step is resolved by a shock, white regions correspond to a rarefaction, and striped regions to a shock-rarefaction.

to a shock-rarefaction. Dashed lines show Y_2, the inflection point for Q_e, which divides the classification diagram into four quadrants. Note that the quadrant with $Y_\pm < Y_2$ displays the opposite behaviour to the quadrant with $Y_\pm > Y_2$. The qualitative structure of the classification diagram is the same for any $a > 1$, although we note that as $a \to 1^+$, $Y_2 \to \infty$ if $\Pi = -1$, but $Y_2 \to 0$ if $\Pi = 1$. If $a < 1$ the flow is dominated by the Kelvin wave, which is stronger at the coast and so shocks occur when $Y_+ > Y_-$. Figure 4.3 also shows that shock-rarefactions require $|Y_+ - Y_-|$ to be finite. Indeed if one takes the weakly nonlinear limit of (4.18), with $Y = Y_\infty + \Delta$ and $|\Delta| \ll 1$, the resulting equation is the KdV equation unless $Y_\infty = Y_2$, in which case (at next order in Δ) one obtains the modified KdV. Thus compound-wave structures are necessarily a finite-amplitude effect.

Although we have focused on the Riemann problem, the classification diagrams in figure 4.3 can be used to interpret a wide range of initial conditions $Y(x, 0)$. By considering the sign of $\partial Y/\partial x$, one may place the initial condition just above or below the line $Y_+ = Y_-$ and then, by considering the value of Y, identify which regions of the front will steepen into a shock, and which regions will lengthen into a rarefaction. Any front that crosses $Y = Y_2$ will form a compound-wave structure. If the flow remains smooth and Q_e is convex, then adding higher-order terms to the hydraulic equation (4.12) makes little difference, and so figure 4.3 is also useful for understanding the behaviour of some fronts in the full QG system

(4.1). However in the case of a front that steepens, the gradient $\partial Y/\partial x$ increases and so higher-order dispersive terms become important.

4.3 The dispersive equation

Here, we consider the dispersive equation (4.18). We first discuss travelling wave solutions, including the special cases of solitons, kinks and intrusions. These serve as a preliminary to applying El's technique of 'dispersive shock-fitting' [El, 2005], which allows the Riemann problem to be classified.

4.3.1 Travelling-wave solutions to the dispersive equation

When higher-order dispersive terms are added to the hydraulic equation (4.12), shocks no longer form. Instead, wave-steepening leads to 'dispersive shock waves' (DSWs; also called undular bores in the context of water waves) which are a canonical and important structure in nonlinear dispersive wave dynamics [Hoefer and Ablowitz, 2009]. For the purposes of this work we need only note that a DSW is an expanding, slowly-modulated waveform, with a linear wave-train at one end and a solitary wave at the other. Thus to understand shock resolution in the dispersive equation it is necessary to understand the behaviour of both linear waves and solitary waves, which motivates the following, more general, discussion of travelling-wave solutions to (4.18).

First, we write (4.18) in potential form:

$$\begin{aligned}(Y')^2 &= \frac{2}{a^2}\,\frac{a^3\mathrm{e}^{-2Y/a} - 4a(\Pi + a^2)\mathrm{e}^{-Y/a} + 2\Pi s Y^2 + \alpha Y + E}{a - (a+2Y)\mathrm{e}^{-2Y/a}},\\ &= \frac{2}{a^2}\,\frac{\mathcal{V}(Y;s,\alpha,E)}{\mathcal{G}(Y)}.\end{aligned} \tag{4.27}$$

Here, primes ($'$) denote differentiation with respect to the moving co-ordinate $\xi = x - st$, s is the speed of the travelling wave and α and E are constants of integration (with E the 'energy' of the orbit). Note that $\mathcal{G} \geq 0$, so that travelling wave solutions exist whenever $\mathcal{V} \geq 0$ and we may often ignore $\mathcal{G}$ in our analysis.

Figure 4.4 shows four representative examples of (4.27). Figure 4.4(a) shows the general case, where the numerator $\mathcal{V}$ has four roots. Double roots of $\mathcal{V}$ at $Y = Y_\infty$ correspond to linear or solitary waves propagating on the background Y_∞ depending on whether they are maxima or minima of $\mathcal{V}$ respectively. Figure 4.4(b) shows a solitary wave of depression propagating on the background $Y_\infty = 1.5$. There are two special configurations of $\mathcal{V}$: if $\mathcal{V}$ has two double roots then the travelling wave is a so-called kink soliton,

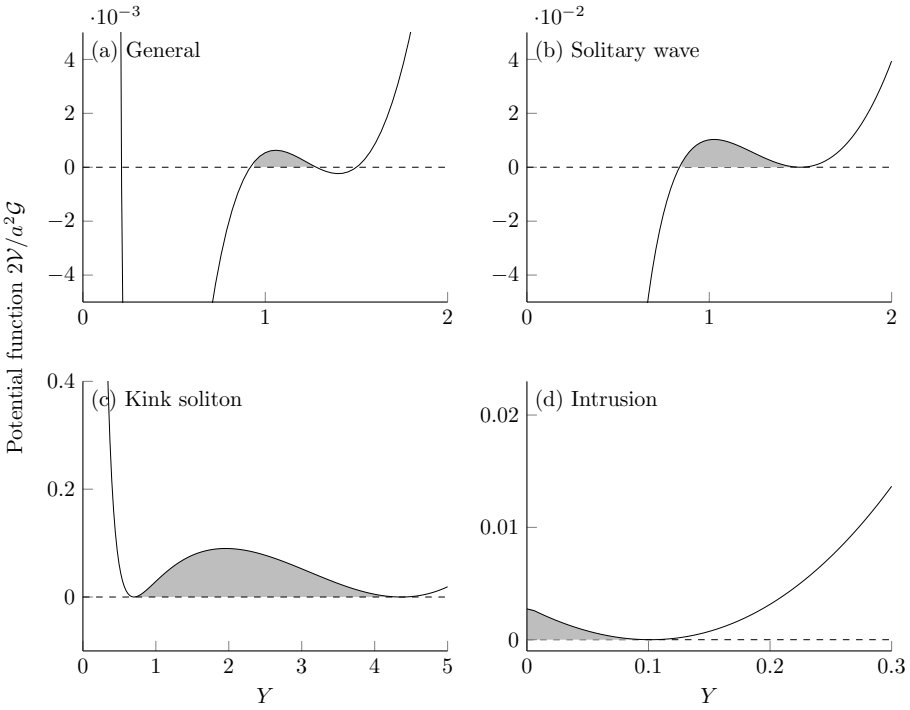

Figure 4.4: Configurations of the potential function (4.27). (a) The general case, (b) Solitary wave case with a local minimum, (c) Kink with two double roots, (d) Intrusion. In each case, travelling waves exist in the shaded region.

as in figure 4.4(c), while if $\mathcal{V}(0) \geq 0$ and there exists a double root in $Y > 0$, as in figure 4.4(d), then the solution is a model for a coastal intrusion (i.e. a constant-width current with a 'nose'). These special cases are discussed below in §4.3.1.3.

4.3.1.1 Linear waves

Consider a small disturbance proportional to $\exp[i(kx - \omega t)]$, propagating on a background Y_∞. By making this ansatz in (4.18) we obtain the dispersion relation

$$\omega = C(Y_\infty)k - \frac{a^2}{4}\Pi\mathcal{G}(Y_\infty)k^3, \tag{4.28a}$$

and the phase speed

$$c_{\mathrm{P}} = \frac{\omega}{k} = C(Y_\infty) - \frac{a^2}{4}\Pi\mathcal{G}(Y_\infty)k^2, \tag{4.28b}$$

which corresponds to advection by the background flow and a dispersive term with sign $-\Pi$. In §4.5, we compare (4.28) with other dispersion relations that have previously been derived for long frontal waves.

4.3.1.2 Solitary waves

The potential equation (4.27) admits solitary-wave solutions for certain values of the parameters s, α and E. It is convenient to ignore $\mathcal{G}$, and seek the range of speeds s for which solitary waves exist.

Thus, consider a solitary wave propagating on the background Y_∞. Then $\mathcal{V}(Y_\infty) = 0$ and $\mathcal{V}'(Y_\infty) = 0$, which sets E and α as functions of Y_∞ and s in (4.27). Further, $\mathcal{V}(Y_\infty)$ must be a local minimum. This requires

$$\begin{aligned} s &> C(Y_\infty) \quad \text{when } \Pi = 1, \\ s &< C(Y_\infty) \quad \text{when } \Pi = -1, \end{aligned} \tag{4.29}$$

which, as expected, sets the minimum (maximum) speed for solitary waves on a current with positive (negative) PVa to be the long-wave speed $C(Y_\infty)$. A solitary wave of depression occurs if $\mathcal{V}$ has a root, say Y_S, in $[0, Y_\infty)$. Thus a depression wave occurs if, in addition to (4.29), $\mathcal{V}(0) \leq 0$ or

$$\begin{aligned} s &< s_0 \quad \text{when } \Pi = 1, \\ s &> s_0 \quad \text{when } \Pi = -1, \end{aligned} \tag{4.30a}$$

where we have introduced the critical speed

$$s_0 = Y_\infty^{-2} \left[2a + \frac{3a^3\Pi}{2} - 2(1 + a^2\Pi)(a + Y_\infty)\mathrm{e}^{-Y_\infty/a} + \frac{a^2\Pi}{2}(a + 2Y_\infty)\mathrm{e}^{-2Y_\infty/a} \right]. \tag{4.30b}$$

The amplitude of the wave is $Y_\infty - Y_\mathrm{S}$. A solitary wave that travels close to speed s_0 extends from Y_∞ to $Y = 0^+$. For s beyond s_0, $\mathcal{V}(0) > 0$ and, provided there is no other root in $[0, Y_\infty)$, the corresponding travelling-wave solution extends to the coast and can be used to model a coastal intrusion, as in figure 4.4(d).

Next, note that a solitary wave of elevation occurs if $\mathcal{V}$ has a root Y_S in (Y_∞, ∞). As $Y \to \infty$, $\mathcal{V} \sim s\Pi Y^2$, so that a sufficient condition for an elevation wave is $\Pi s < 0$. However elevation waves may also exist for $\Pi s > 0$, provided Y_S exists. The limiting case for the existence of the additional root occurs when $\mathcal{V}'(Y_\mathrm{S}) = 0$, so that $\mathcal{V}$ has two double roots and the corresponding travelling-wave solution is a kink soliton. Given a, Π and Y_∞, we seek a pair (s_K, Y_K) such that $V(Y_K) = V'(Y_K) = 0$, with $Y_K > Y_\infty$. The kink soliton connects the phase-plane equilibria Y_∞ and Y_K, and travels at speed s_K. Since the kink is the limiting case of an elevation wave, Y_K is an upper bound on the soliton amplitude and s_K is the maximum (minimum) speed for a solitary wave of elevation on a current with positive (negative) PVa.

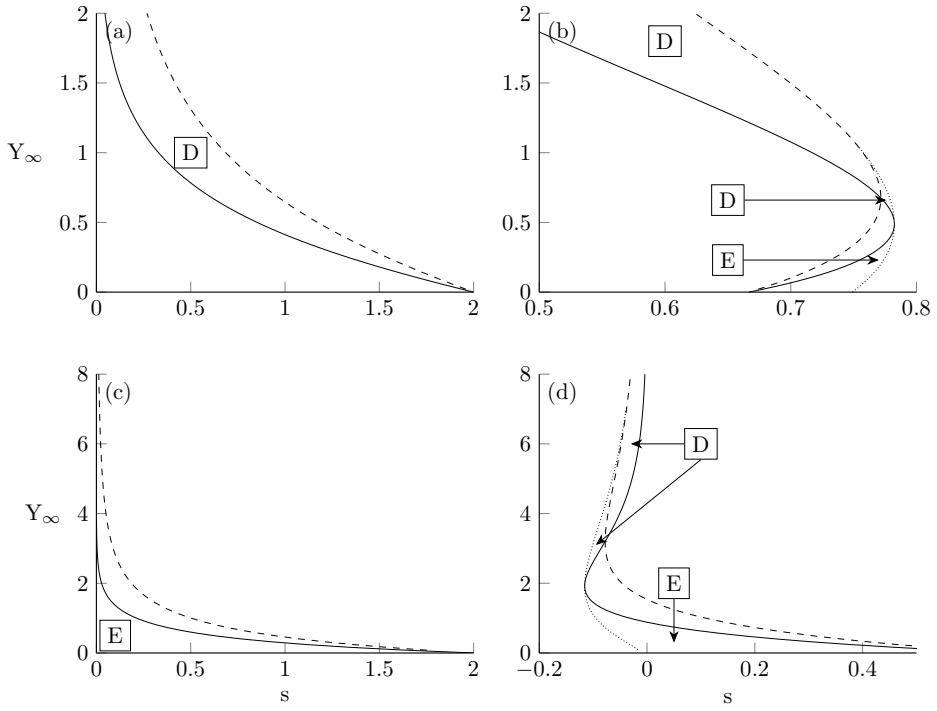

Figure 4.5: Possible solitary wave speeds s, as a function of the background Y_∞. The solid, dashed and dotted curves are C, s_0 and s_K respectively. Waves of elevation exist in regions marked E, and waves of depression exist in regions marked D. The parameters a and Π are chosen so that each plot shows a different regime. (a) $\Pi = 1$, $a = 0.5$, (b) $\Pi = 1$, $a = 1.5$, (c) $\Pi = -1$, $a = 0.5$, (d) $\Pi = -1$, $a = 1.5$.

By combining all of the above, we may determine the range of allowed solitary wave-speeds s as a function of Π, a and the background state Y_∞. We find that there are four regimes, depending on the value of Π and a. An example of each regime is shown in figure 4.5, where the limiting values C, s_0 and s_K are plotted as functions of Y_∞ as the solid, dashed and dotted curves respectively. Depression waves exist in regions of the (s, Y_∞)-plane marked D, and elevation waves exist in regions marked E. The solitary waves are of vanishing amplitude close to the solid curve $C(Y_\infty)$, and reach maximum amplitude at the dashed or dotted curve (or at $s = 0$ in the case of figure 4.5(c), where the solitary wave has infinite amplitude). For small a, the curves s_0 and C do not intersect and only one type of solitary wave is possible (figure 4.5 (a) and (c)). For a sufficiently large, the two curves intersect and so both elevation and depression waves (as well as kinks) exist, with depression waves existing for $Y_\infty > Y_2$ (figure 4.5 (b) or (d)). The intersection between s_0 and C occurs for the first time when $a = 1$ if $\Pi = 1$, and when $a = 2/\sqrt{3}$ if $\Pi = -1$. (The critical value of a when $\Pi = -1$ can be determined by considering the sign of $s_0 - C$ for large Y_∞.)

4.3.1.3 Special cases

We now discuss the two special cases mentioned above: the kink soliton and the coastal intrusion. Kink solitons require that $\mathcal{V}$ has two double roots, say Y_∞ and Y_K, which correspond to the two far-field states connected by the travelling wave. It turns out that this configuration is only possible if a is sufficiently large ($a > 1$ when $\Pi = 1$, and $a > 2/\sqrt{3}$ when $\Pi = -1$). The propagation speed $s_K(Y_\infty)$ is plotted as a dotted curve in figure 4.5(b) and (d). We find that $s_K(Y_\infty)$ has a turning point at Y_2, the turning point for the long-wave speed $C(Y)$. Each s_K is associated with two background states, one on either side of Y_2, and the kink soliton connects these two states. Thus the kink is a result of the non-convexity of the flux function Q_e, as in the modified KdV equation. Kink solitons are of particular interest because they are travelling-wave solutions that connect two different far-field states, and thus are analogous to shock-wave solutions to the hydraulic equation. However, s_K does not lie between $C(Y_\infty)$ and $C(Y_K)$, so the propagation speed does not satisfy the entropy condition (4.26). The kink soliton is therefore sometimes referred to as a non-classical or under-compressive shock wave [El et al., 2017]. Kinks will later be shown to play an important role in the Riemann problem when the initial step crosses Y_2.

Figure 4.6 shows the kink soliton solution propagating on the background $Y_\infty = 0.7$ with $\Pi = -1$ and $a = 1.5$, which are the values used for the potential function in figure 4.4(c). The phase portrait for travelling-wave solutions propagating at speed $s_K = -0.076$ is shown in figure 4.6(a). There are saddle points at Y_∞ and $Y_K = 4.37$, and a centre at $Y \approx 2$. The kink soliton is represented by the heteroclinic orbit connecting the two saddle points, which is shown dashed. Closed orbits inside the dashed curve correspond to lower-energy periodic waves. Figure 4.6(b) shows a numerical solution to the dispersive long-wave equation (4.18) when the kink soliton is used as an initial condition (solid curve). The dashed and dash-dotted curves show the solution at $t = 500$ and $t = 1\,000$ respectively, and confirm that the kink propagates at constant speed s_K.

Here and elsewhere numerical results are obtained using a pseudo-spectral method, where the equation is Fourier-transformed in x and then advanced in time using an adaptive fourth-order Runge–Kutta scheme. The domain is truncated at some large value of x, and a corresponding step down from Y_K to Y_∞ is introduced to enforce the periodicity required by the spectral method. The domain is taken large enough so that the two steps do not interfere with each other. The equation is solved using

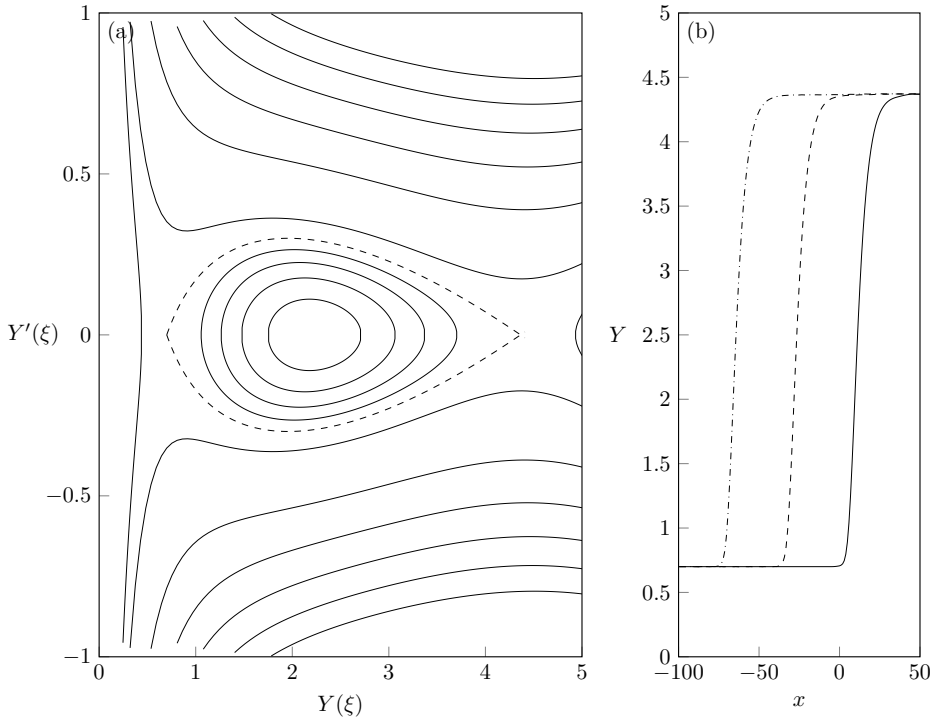

Figure 4.6: Kink soliton connecting $Y_\infty = 0.7$ and $Y_K = 4.41$, with $a = 1.5$, $\Pi = -1$. (a) The phase portrait with $s = s_K = -0.076$. The dashed curve is the kink orbit, with curves inside corresponding to periodic waves. (b) Propagation of the kink soliton in the equation (4.18). The solid, dashed and dash-dotted curves show the solution at $t = 0$, 500, 1 000 respectively.

the long-wave co-ordinates X and T, but results are plotted in the original co-ordinates x and t. In all results shown, the long-wave parameter $\epsilon = 0.1$.

If the condition (4.30) is not satisfied, the corresponding travelling-wave solution reaches $Y = 0$ and may be joined to a constant-width current to give a model for a coastal intrusion of permanent form. Letting $Y \to 0$ in (4.27) we see that the nose of the intrusion meets the coast at right angles unless $\mathcal{V}$ has a double root at zero; that is, unless the intrusion is a kink soliton with background $Y_\infty = 0$. In this case, the front meets the coast with

$$(Y')^2 = \frac{2\Pi(as_K - 1)}{a^2}. \tag{4.31}$$

Such an intrusion is shown in figure 4.7, for $\Pi = 1$ and $a = 1.05$, which are the values used for figure 4.4(d). The phase portrait in figure 4.7(a) has a saddle point at $Y_K = 0.101$, but since $\mathcal{G}(0)$ is infinite, the double root in $\mathcal{V}$ does not lead to a saddle point at $Y = 0$. Figure 4.7(b) shows the evolution of the intrusion at $t = 0$, 500, 1 000 (solid, dashed and dash-dotted curves respectively). We performed other numerical experiments (not shown) using a solitary wave intrusion that meets the coast at right-

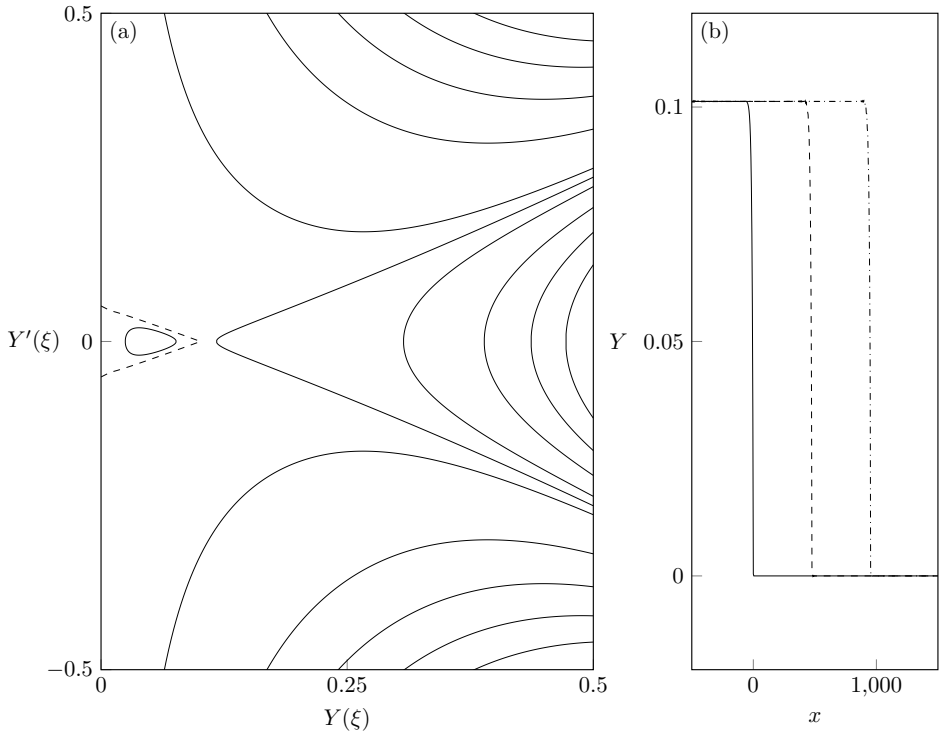

Figure 4.7: Coastal intrusion of permanent form, with $a = 1.05$ and $\Pi = 1$. (a) The phase portrait with $s = s_K = 0.95$. The dashed curve is the intrusion orbit, with the curve inside corresponding to a periodic travelling wave. (b) Propagation of the intrusion, with the solution shown at $t = 0, 500, 1\ 000$ (solid, dashed and dash-dotted curves respectively).

angles. The infinite gradient at $Y = 0$ led to a build-up of spurious short waves, which quickly grew and disturbed the intrusion.

The intrusion of a PV front is discussed at length for a dam-break scenario in Stern and Helfrich [2002]. The authors seek similarity solutions to the long-wave equations and hence the intrusion is always a rarefaction, a result that is supported by numerical and laboratory experiments. Johnson et al. [2017] also find that PV intrusions driven by a uniform source either rarefy or form shocks. Thus although intrusions of permanent form are valid solutions to the long-wave QG equations, it is not clear what initial conditions would give rise to one.

4.3.2 The Riemann problem for the dispersive equation

El's technique of dispersive shock-fitting is based on the GP [Gurevich and Pitaevskii, 1973] approach to solving the Riemann problem for the KdV equation, but generalised to deal with a wider class of (non-integrable) equations. The key idea in the GP approach is that the Whitham equations

(i.e. the period-averaged equations) governing the modulation of the DSW can be matched naturally to the hydraulic equation in the far field. Provided that the equation under consideration satisfies certain conditions, El's technique allows one to obtain the propagation speeds of the DSW edges, the wavenumber at the linear edge and the conjugate wavenumber (i.e. the inverse half-width) and amplitude at the soliton edge. El [2005] gives a full explanation of the theory and the derivation of the necessary conditions, and Kamchatnov [2019] and Maiden et al. [2020] adapt El's technique to other initial conditions.

4.3.2.1 Applicability of El's technique

For El's technique to apply, the dispersive equation (4.18) must satisfy the following conditions:

1. It admits a dispersionless (hydraulic) limit obtained by introducing the slow variables $X = \epsilon x$ and $T = \epsilon t$. By construction, this is true.

2. The linear dispersion relation $\omega(k)$ is real-valued. This was shown in (4.28a).

3. It possesses at least two conservation laws. This is required so that the Whitham system of averaged conservation laws can be formulated in principal, although El's technique is designed to avoid this. These may be taken as the kinematic boundary condition (4.7b) and equation (4.19).

4. It supports periodic travelling-wave solutions, parameterised by three independent variables. These can be taken to be the constants of integration s, α and E in the potential (4.27). The potential function must have at least three real zeros (in general (4.27) has four, as in figure 4.4(a)), and must exhibit quadratic behaviour in the linear and solitary-wave limits. This condition allows the Whitham equations to be matched with the hydraulic equation at the edges of the DSW. The necessary quadratic behaviour is shown below.

5. The Whitham system corresponding to the two averaged conservation laws plus the wavenumber conservation law $k_t + \omega_x = 0$ is hyperbolic. Hyperbolicity cannot be checked without directly solving the Whitham system so this condition should be verified by, for example, comparison of theoretical results with numerical simulations. However, non-convexity of the flux function Q_e implies that (4.18) is not genuinely nonlinear (the characteristic velocity C is not monotonic), and in many cases this leads to non-strict hyperbolicity [El et al.,

2017]. The compound-wave structures discussed in §4.2.1 carry over to the Whitham equations, and lead to richer behaviour than in the simple-wave case, where the solution is a DSW. El's technique should therefore only be applied to initial steps that do not straddle Y_2, so that the flux function is convex. The effects of non-convexity are discussed in §4.4.2.

It remains to show that the potential function (4.27) displays quadratic behaviour in the linear and solitary-wave limits. Essentially, we would like to show that in these limits

$$\frac{2}{a^2}\,\frac{\mathcal{V}(Y;s,\alpha,E)}{\mathcal{G}(Y)} \sim (Y-Y_\infty)^2\Phi(Y), \tag{4.32}$$

where Y_∞ is the solitary or linear-wave background, and $\Phi(Y) = O(1)$ for $|Y - Y_\infty| \ll 1$. In both limits, α and E may be written as functions of s and Y_∞, so may be taken as fixed. Unless $Y_\infty \ll 1$ and the front is close to the coast, $\mathcal{G} = O(1)$ and it is sufficient to check the behaviour of $\mathcal{V}(Y;s,Y_\infty)$. Since Y_∞ is a double root of $\mathcal{V}$, the potential function displays the quadratic behaviour (4.32) provided $\mathcal{V}''(Y_\infty)$ is non-zero, i.e. by (4.29) s is sufficiently far from the long-wave speed $C(Y_\infty)$.

4.3.2.2 Dispersive shock-fitting

With these caveats about non-convexity and distance from the coast in mind, El's technique proceeds as follows. The wavenumber and conjugate wavenumber at the linear and solitary-wave edges of the DSW are found by solving the ordinary differential-equations (ODEs)

$$\begin{aligned}\frac{\mathrm{d}k}{\mathrm{d}Y} &= \frac{\partial\omega/\partial Y}{C(Y)-\partial\omega/\partial k},\\ \frac{\mathrm{d}\widetilde{k}}{\mathrm{d}Y} &= \frac{\partial\widetilde{\omega}/\partial Y}{C(Y)-\partial\widetilde{\omega}/\partial\widetilde{k}}.\end{aligned} \tag{4.33}$$

Here, $\widetilde{k}$ is the conjugate wavenumber and $\widetilde{\omega} = -\mathrm{i}\omega(Y,\mathrm{i}\widetilde{k})$ is the conjugate dispersion relation for solitary waves. The fact that the solitary-wave propagation speed can be described by linear-wave dynamics can be seen by considering the exponential tail. If the tail is proportional to $\exp(\widetilde{k}x - \widetilde{\omega}t)$ then it obeys a linear dispersion relation $\widetilde{\omega}$ as defined above, with propagation speed $s = \widetilde{\omega}/\widetilde{k}$ [Kamchatnov, 2019]. The ODEs (4.33) are derived in El [2005] using the ansatz $k = k(Y)$ in the wavenumber conservation law, combined with the hydraulic equation (4.12) which is assumed to apply at the edge of the DSW. The general solutions to (4.33)

are

$$k^2(Y) = \frac{8\Pi}{3a^2\mathcal{G}(Y)^{2/3}} \int^{Y} \frac{C'(\xi)}{\mathcal{G}(\xi)^{1/3}}\, \mathrm{d}\xi,$$
$$\widetilde{k}^2(Y) = \frac{-8\Pi}{3a^2\mathcal{G}(Y)^{2/3}} \int^{Y} \frac{C'(\xi)}{\mathcal{G}(\xi)^{1/3}}\, \mathrm{d}\xi. \tag{4.34}$$

To connect (4.34) with the far-field solution, we apply the boundary conditions $k = 0$ at the soliton edge of the DSW, and $\widetilde{k} = 0$ at the linear-wave end. Then we may obtain $k_\pm$ and $\widetilde{k}_\mp$, the wavenumber and conjugate wavenumber at the leading/trailing edge of the DSW, by evaluating (4.34) at $Y_\pm$. Bearing in mind the form of the dispersion relation (4.28a) and the restriction on soliton speed (4.29) it is clear that DSWs have solitary waves on the right when $\Pi = 1$, and on the left when $\Pi = -1$. Thus if $\Pi = 1$ we have

$$k_-^2 = \frac{8}{3a^2\mathcal{G}(Y_-)^{2/3}} \int_{Y_+}^{Y_-} \frac{C'(Y)}{\mathcal{G}(Y)^{1/3}}\, \mathrm{d}Y,$$
$$\widetilde{k}_+^2 = \frac{8}{3a^2\mathcal{G}(Y_+)^{2/3}} \int_{Y_+}^{Y_-} \frac{C'(Y)}{\mathcal{G}(Y)^{1/3}}\, \mathrm{d}Y, \tag{4.35a}$$

for the trailing linear and leading solitary wavenumbers, while if $\Pi = -1$ we have

$$k_+^2 = \frac{8}{3a^2\mathcal{G}(Y_+)^{2/3}} \int_{Y_+}^{Y_-} \frac{C'(Y)}{\mathcal{G}(Y)^{1/3}}\, \mathrm{d}Y,$$
$$\widetilde{k}_-^2 = \frac{8}{3a^2\mathcal{G}(Y_-)^{2/3}} \int_{Y_+}^{Y_-} \frac{C'(Y)}{\mathcal{G}(Y)^{1/3}}\, \mathrm{d}Y, \tag{4.35b}$$

for the trailing solitary and leading linear wavenumbers. Note that since El's method is restricted to initial steps that do not cross Y_2, $C'(Y)$ is single-signed and (4.35) is real provided $Y_\pm$ are taken from the shaded region in figure 4.3, i.e. provided that the corresponding step in the hydraulic equation leads to a shock rather than a rarefaction.

The propagation speeds of the solitary and linear-wave ends of the DSW are

$$s_\pm = \frac{\widetilde{\omega}(Y_\pm, \widetilde{k}_\pm)}{\widetilde{k}_\pm}, \quad s_\mp = \left.\frac{\partial\omega}{\partial k}\right|_{Y_\mp, k_\mp}, \tag{4.36}$$

when $\Pi = \pm 1$. Finally, the following inequalities must be verified:

$$s_- < C_-, \quad s_+ > C_+, \quad s_+ > s_-. \tag{4.37}$$

The first two of these conditions are analogous to the entropy condition (4.26), and ensure that characteristics from the external, hydraulic solution transfer information into the DSW. In fact, they are trivially satisfied by

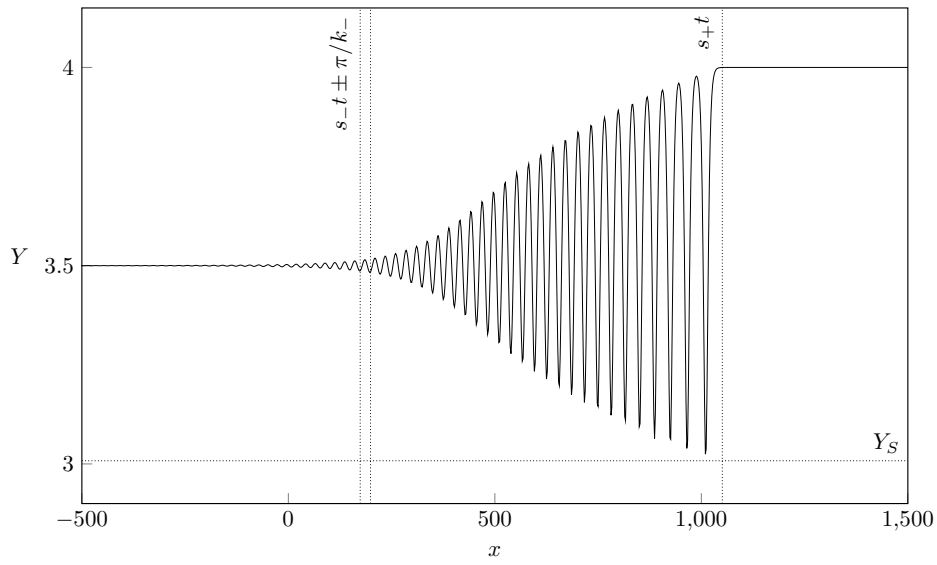

Figure 4.8: Numerical solution to the Riemann problem for the dispersive equation (4.18). The parameters are $a = 0.9$, $\Pi = 1$ and the smoothed initial step is from $Y_- = 3.5$ to $Y_+ = 4$. The solution is shown at $t = 30\,000$. Dotted lines correspond to theoretical predictions from §4.3.2.2.

(4.36). The third condition checks that the DSW has positive width. We must also check that the solitary wave speed given by El's technique is valid according to the discussion of §4.3.1.2, where we identify the background Y_∞ with $Y_\pm$ when $\Pi = \pm 1$.

4.4 Numerical results

Here, we present numerical solutions to the dispersive long-wave equation (4.18) and the full QG equation (4.1). The former are compared with predictions for propagation speed and solitary-wave amplitude that were derived in §4.3.2.2 using El's technique, while the QG equations are used to test the validity of the long-wave approximation.

4.4.1 Verification of El's technique

We begin with numerical simulations of the dispersive equation. All computations are carried out using the pseudo-spectral method described in §4.3.1.3, and use $\epsilon = 0.1$.

Figure 4.8 shows the result for a current with positive PVa and $a = 0.9$. The Riemann problem is initialised with a smoothed step from $Y_- = 3.5$ to $Y_+ = 4$, and the solution is shown at $t = 30\,000$. From §4.3.2.2 currents with positive PVa are led by a solitary wave, and from figure 4.5 the only

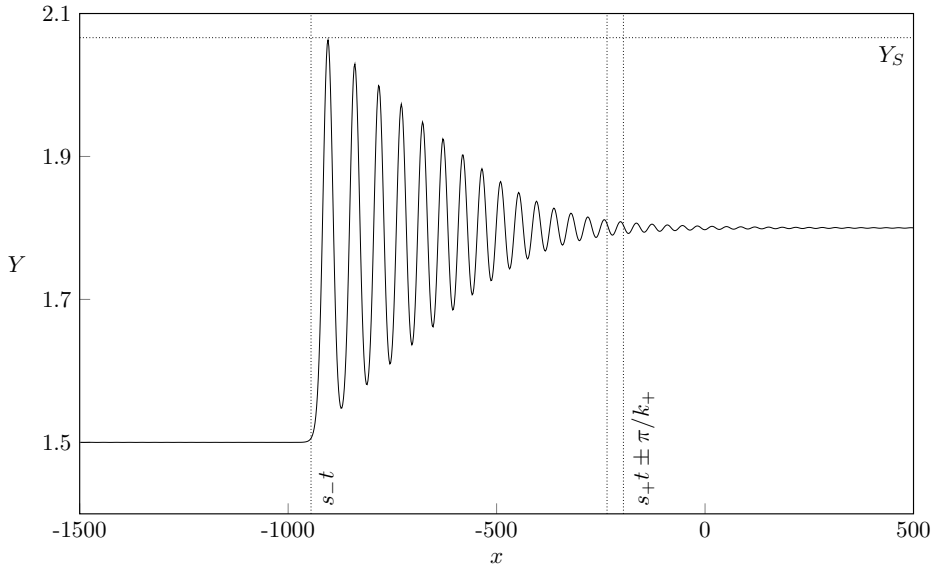

Figure 4.9: As figure 4.8, but for a current with negative PVa and $a = 1.25$. The initial step is from $Y_- = 1.5$ to $Y_+ = 1.8$ and the solution is shown at $t = 30\ 000$.

solitary waves that exist when $a < 1$ and $\Pi = 1$ are depression waves. We thus expect the step to be resolved by a DSW$^-$ (a depression DSW) with the solitary-wave end on the right. This is clearly visible in figure 4.8, along with the slowly-modulated internal structure of the DSW. Dotted lines show predictions from El's technique. The horizontal line at $Y = Y_\mathrm{S}$ and the vertical line at $x = s_+t$ show good agreement between theory and numerics at the solitary-wave edge of the DSW. The left two vertical lines are at $x = s_-t \pm \pi/k_-$ and therefore span one wavelength at the trailing edge of the DSW. The numerical solution has a small-amplitude wave of the correct wavelength at $x = s_-t$ but, as is typical in simulations of such problems, the amplitude is clearly non-zero for $x < s_-t$. The amplitude discrepancy is likely due to higher order (numerical) dispersive effects [Congy et al., 2019]. The integration in figure 4.8 was continued until $t = 50\ 000$. At the point at which the integration was halted, the minimum value of Y was still decreasing, but at a rate of $O(10^{-6})$ so that the DSW was, for all intents and purposes, fully developed. The minimum value of Y and the mean propagation speed of the leading solitary wave agree with the theoretical predictions for Y_S and s_+ to three decimal places.

Figure 4.9 shows a current with negative PVa and $a = 2$, with the initial step connecting $Y_- = 1.5$ and $Y_+ = 1.8$. As predicted for currents with negative PVa, the DSW has a solitary wave on the left. Only elevation waves exist for the background $Y_\infty = Y_- < Y_2$, so the step is resolved by a DSW$^+$ (elevation DSW). The solution is shown at $t = 30\ 000$, and

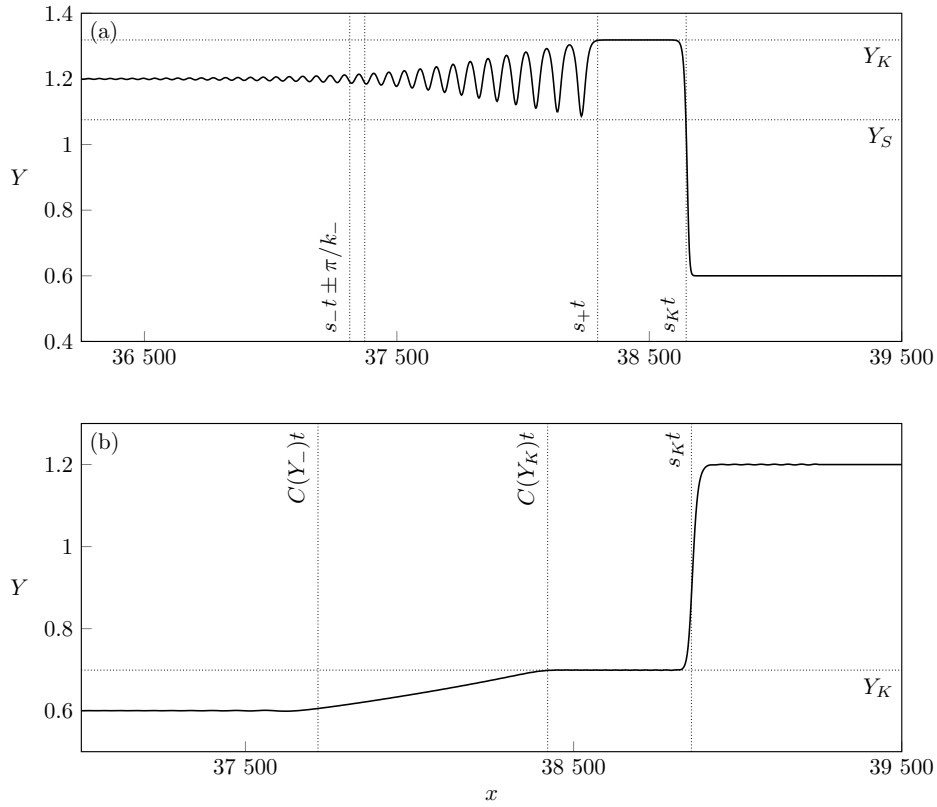

Figure 4.10: As figure 4.8, but for an initial step that crosses the inflection point Y_2. The parameters are $a = 2$, $\Pi = 1$ and the solution is shown at $t = 50\ 000$. (a) Initial step down from $Y_- = 1.2$ to $Y_+ = 0.6$, (b) initial step up from $Y_- = 0.6$ to $Y_+ = 1.2$. In both cases, the step is resolved by a compound-wave structure involving a kink soliton (see text).

the integration was continued until $t = 50\ 000$. Again, the solitary-wave amplitude and propagation speed agree with theoretical predictions to three decimal places while at the linear end of the DSW there is good agreement in wavenumber k_+ and, as above, small waves in $x > s_+t$.

4.4.2 Effects of non-convexity

If the initial step crosses the inflection point Y_2 the flux function Q_e is non-convex, so the hydraulic limit is not genuinely nonlinear and El's technique cannot be directly applied. In this case, numerical results show that the Riemann problem is resolved by a compound-wave structure, as discussed for the modified KdV equation in El et al. [2017] and the Miyata–Camassa–Choi equations in Esler and Pearce [2011].

Figure 4.10 shows two examples of compound-wave structures in a current with $a = 2$ and $\Pi = 1$. In both cases, the initial step is resolved by a combination of a kink soliton and a simple wave (DSW or rarefaction), with

an expanding constant-width region that connects the two. For currents with positive PVa, the kink is faster than any solitary wave or rarefaction and so must be on the right. Thus in both cases the kink connects Y_+ to the (uniquely determined) intermediate value Y_K. The right-most vertical line gives the predicted location of the kink, $x = s_K t$. As in Esler and Pearce [2011], it seems that the simple-wave structure can be understood by applying El's technique to the 'secondary' Riemann problem with an initial step from Y_- to Y_K. In figure 4.10(a), where $Y_K > Y_- > Y_2$, we would expect this secondary step to be resolved by a DSW$^-$. This is indeed the case, and El's technique captures the amplitude and speed at the leading edge of the DSW, as well as the wavenumber at the trailing edge. In figure 4.10(b), $Y_- < Y_K < Y_2$ so that the secondary step is resolved by a rarefaction over the region $C(Y_-) < x/t < C(Y_K)$.

Note that, in both cases shown in figure 4.10, the step 'splits' into a steadily-propagating kink, which crosses the inflection point, and a secondary, simple-wave structure that lies within the convex region of the flux function. Thus the kink can be thought of as removing the non-convexity from the initial step. For the present equation the kink soliton exists provided the background state (here Y_+) is less than some critical value (see the termination of the dotted curve s_K in figure 4.5(b) and (d)). It is not clear how the initial step should be resolved if Y_+ is greater than the critical value. Numerical simulations suggest that the solution passes through $Y = 0$, which is clearly unphysical. El et al. [2017] introduce a new type of DSW, the so-called contact DSW, to resolve the Riemann problem in the modified KdV for steps where the kink does not exist, but the treatment of this case appears to involve solving the Whitham system and so is not pursued here. It is notable that, unlike for the modified KdV, the existence of the kink in the present model does not depend on the sign of the dispersion.

4.4.3 Classification of the dispersive Riemann problem

Figure 4.11 classifies the resolution of the initial step $Y_\pm$ for the particular choice of parameters $a = 2$, $\Pi = 1$ (figure 4.11(a)) and $a = 1.5$, $\Pi = -1$ (figure 4.11(b)). Hatched regions of the diagram show where the initial step cannot be classified using El's technique. We have labelled the diagram following the notation of El et al. [2017], whereby K, R and DSW$^\pm$ correspond to kinks, rarefactions and DSWs of elevation/depression respectively. Compound-wave structures are denoted by a vertical bar (|) and should be read from left to right so that, for example, K|DSW$^+$ means

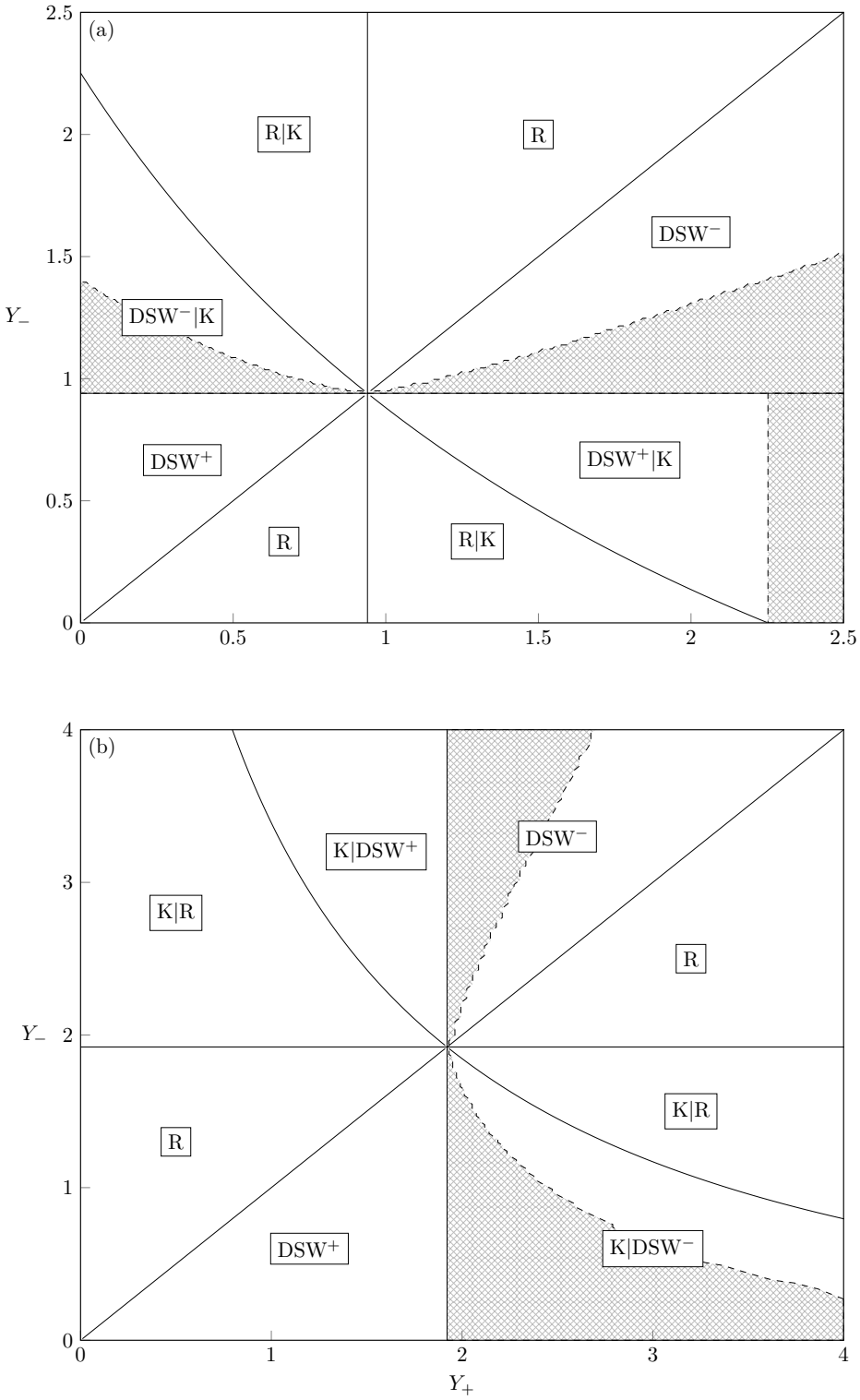

Figure 4.11: Diagram showing the resolution of the dispersive Riemann problem for (a) $a = 2$, $\Pi = 1$, and (b) $a = 1.5$, $\Pi = -1$. Labels correspond to kinks, rarefactions and dispersive shock waves, with the superscript DSW$^{\pm}$ signifying elevation or depression solitary waves. The hatched regions of the diagram cannot be classified using El's technique.

that the initial step is resolved by a kink from Y_- to Y_K, and a DSW with a solitary wave of elevation connecting Y_K to Y_+. As discussed in §4.3.2.2, DSWs that form on currents with positive PVa have solitary waves on the right, while those on negative-PVa currents have solitary waves on the left.

As in the hydraulic classification diagram in figure 4.3, for vortically-dominated currents with $a > 1$ the $Y_\pm$ parameter space is split into four quadrants by the inflection point Y_2. Kelvin-wave dominated flows with $a < 1$ behave like the top-right (bottom-left) quadrant when the current has positive (negative) PVa, and so in both cases the step is resolved by a DSW when $Y_+ > Y_-$. Steps that cross Y_2 are resolved by compound-wave structures like those in figure 4.10. If the step is such that a kink soliton exists then this leads (trails) the transition region for currents with positive (negative) PVa and connects the far-field states via the intermediate level Y_K. The kink creates a secondary step, which is resolved by a simple-wave structure connecting Y_K to Y_- when $\Pi = 1$, and Y_K to Y_+ when $\Pi = -1$. For example, consider a step in the upper-left quadrant of figure 4.11(a). The kink soliton connects $Y_+ < Y_2$ to a unique $Y_K > Y_2$, and then the secondary step from Y_K to $Y_- > Y_2$ is resolved by a rarefaction if $Y_- > Y_K$ (the region labelled R|K) or by a DSW$^-$ if $Y_- < Y_K$ (the region labelled DSW$^-$|K). Thus the dividing line in the upper-left quadrant is $Y_- = Y_K(Y_+)$. If the kink soliton does not exist then numerical simulations suggest that Y tries to pass through the coast. We did not investigate the behaviour of the front any further in this case, and so this region has not been classified (rectangular hatched region with $Y_+ > 2.2$ in figure 4.11(a)). Finally, we note that El's technique does not always produce a valid solution. That is, the value of s predicted by (4.36) can lie outside the permitted range of solitary-wave speeds. This seems to only occur for larger initial steps (or secondary steps) that result in a depression DSW, and these regions are hatched in figure 4.11. Numerical simulations show that the step is still resolved by an expanding modulated wave-train.

4.4.4 The full problem

The fully nonlinear free-boundary QG system (4.1) can be solved numerically to a high level of accuracy using the method of contour dynamics with surgery [Dritschel, 1988]. We performed several simulations based on the adaptation of Dritschel's algorithm discussed in §3.3.

Figure 4.12 shows three contour dynamic simulations initialised using a smoothed step. Figure 4.12(a) shows a run using the same parameters as figure 4.8, with the solution plotted at $t = 650$. The initial step has

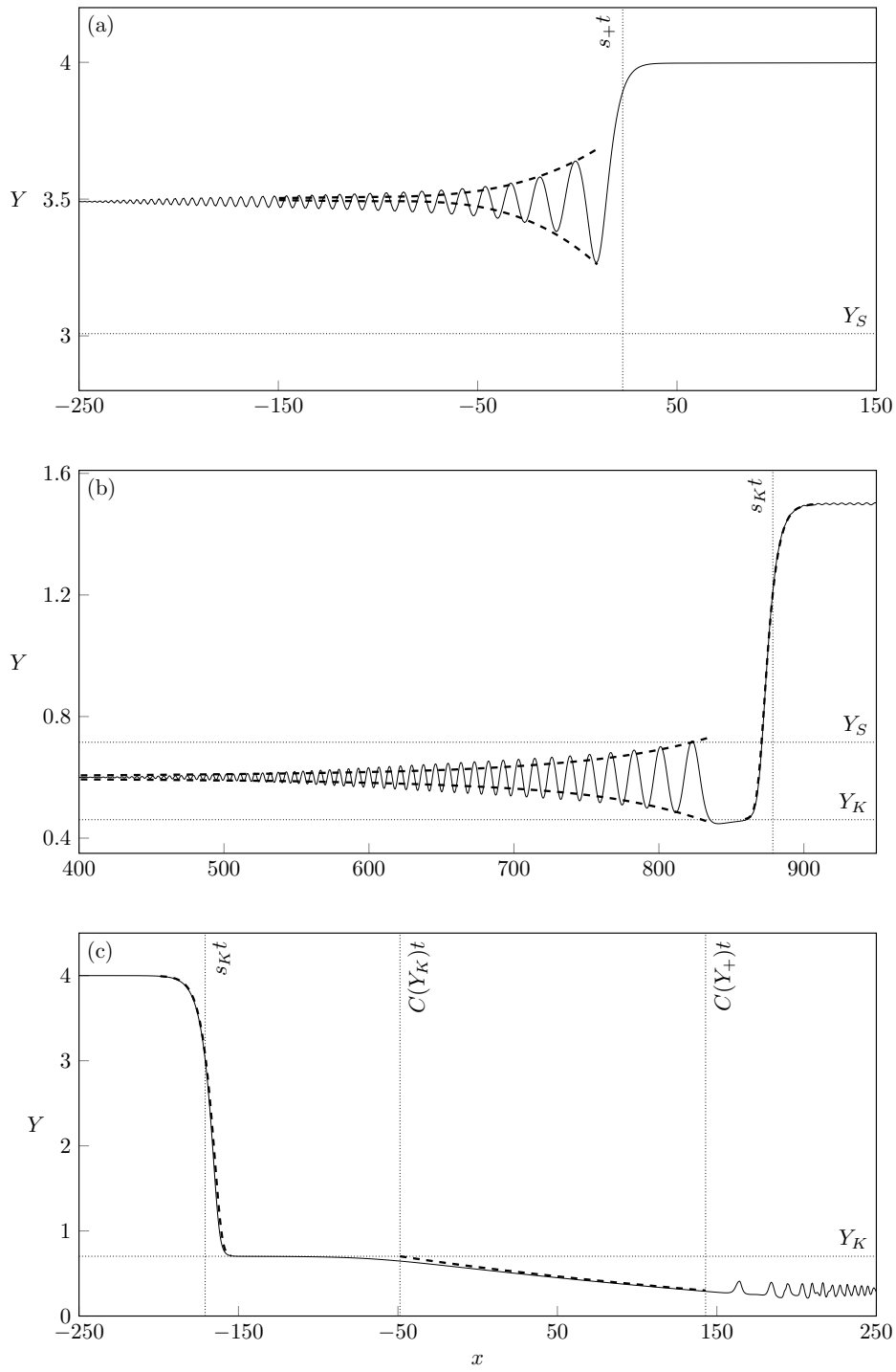

Figure 4.12: Contour dynamic simulations of the Riemann problem in the full QG system (4.1). Dotted lines show predictions of DSW parameters from El's technique, and heavy dashed curves show the DSW envelope from the dispersive long-wave equation in (a) and (b), and kink and rarefaction profiles in (b) and (c). The parameters in (a) are the same as in figure 4.8 (DSW$^-$), with the solution shown at $t = 650$. In (b), $a = 2$ and $\Pi = 1$ with the initial step from $Y_- = 0.6$ to $Y_+ = 1.5$ (DSW$^+$|K). The solution is shown at $t = 1150$. In (c), $a = 2$ and $\Pi = -1$ with the initial step from $Y_- = 4$ to $Y_+ = 0.3$ (K|R). The solution is shown at $t = 750$.

clearly begun to evolve into a DSW$^-$, with the leading edge located at approximately s_+t (vertical dotted line). The dashed curves give the envelope of the solution to the dispersive equation at $t = 650$, and show that agreement with the long-wave theory is better at the solitary-wave end than at the linear end, supporting the hypothesis that higher-order dispersive effects are important here. The lateral extent of the DSW is also much greater than predicted by the long-wave theory, where El's technique gives $s_-t = 4$. The contour dynamics algorithm places more resolution in regions of higher curvature, so that the presence of many small-amplitude waves (and the longer extent of the DSW) means that integrating the full QG equations for the same length of time as the dispersive equations is prohibitively expensive. As the long-wave theory predicts that the DSW develops over tens of thousands of time units, we were not able to continue any of our simulations for long enough to observe whether the leading solitary wave reaches the predicted amplitude Y_{S}. However, the amplitude of the wave was still increasing when integration was stopped.

Figure 4.12(b) shows a run with $a = 2$ and $\Pi = 1$, with the solution plotted at $t = 1150$. As predicted by the long-wave theory the initial step evolves into a DSW$^+$|K, where the kink soliton connects $Y_K = 0.46$ to $Y_+ = 1.5$. Both the kink and solitary-wave amplitude are captured well by the long-wave theory (horizontal dotted lines), as is the propagation speed s_K (vertical dotted line). The DSW envelope from the dispersive equation again shows better agreement at the solitary wave end, and the kink profile computed by solving the potential form (4.27) matches the QG solution almost perfectly (right-most dashed curve). Thus the long-wave theory accurately predicts the existence and form of steadily-propagating kink solitons in the full QG system. Note that the small-amplitude ripples in $x > 900$ are a numerical artefact that arises due to the finite length of the contour.

Figure 4.12(c) shows an example of a kink-rarefaction with $a = 2$ and $\Pi = -1$, with the solution plotted at $t = 750$. Again there is excellent agreement between contour dynamics and the long-wave predictions for the shape and speed of the kink and rarefaction (dashed curves above and below $Y_K = 0.7$ respectively). The effect of higher-order terms that are absent from the dispersive equation (4.18) is to smooth the transition between the two simple-wave structures, as can be seen at the trailing end of the rarefaction near $x = -50$. The wave-train in $x > 150$ is a transient remnant of the initial start-up and does not affect the kink-rarefaction.

In all of the cases presented here, the long-time behaviour of the full QG system closely follows the long-wave theory. That this holds for the most

stringent test of the Riemann problem, where the initial condition violates the long-wave assumption, reflects the fact that the initial tendency of the frontal displacement—whether to lengthen or steepen—is due to the interaction between Kelvin-wave flow and vorticity dynamics, which does not rely on the assumption of a slowly-varying current. Once a disturbance has begun to develop, its intrinsic length-scale increases and the long-wave theory becomes an appropriate model [Esler and Pearce, 2011, p. 5].

4.5 Discussion

A fully nonlinear, dispersive long-wave model has been used to study the dynamics of PV fronts near a vertical coast in the QG limit. The model is the same as that developed by Pratt and Stern [1986], but the focus here is on fronts that are sufficiently close to the coast that they feel the effects of the Kelvin-wave flow and image vorticity. When vortical effects are dominant, the flux function in the leading-order long-wave (hydraulic) equation is non-convex and compound-wave structures (shock-rarefactions) exist. An example of this is shown in figure 4.2, and the qualitative behaviour of unforced long waves is completely described in figure 4.3. When higher-order dispersive terms are added to the hydraulic equation, shocks are replaced by dispersive shock waves. We have used El's technique of dispersive shock-fitting [El, 2005] to find certain key parameters of DSWs that arise from an initial step, namely the propagation speed and wavenumber at either end of the DSW. El's technique is valid only for initial steps that do not cross the inflection point Y_2, but we find that in fact it can also be used to describe 'secondary' DSWs arising as part of a compound-wave structure (see figure 4.10). In the dispersive equation, these compound-wave structures combine either DSWs or rarefactions with a kink soliton. The Riemann problem for the dispersive equation is partially classified in figure 4.11. Section 4.4.4 compares the dispersive long-wave theory with contour dynamic simulations of the full QG system, and shows that the long-wave theory describes the long-time evolution of the Riemann problem well.

The influence of the coastal boundary on the propagation of long waves becomes apparent on considering the linear wave-speed (4.28). In general, the phase speed of a long linear wave on a PV front is

$$c = Ak^2 - B, \tag{4.38}$$

for some dimensional constants A and B. In the present model, these are

$$A_{\mathrm{W}} = -\frac{L_{\mathrm{R}}^3 \Pi_0 H}{4} + \frac{L_{\mathrm{R}}^2 \Pi_0 H}{4} \left(L_{\mathrm{R}} + 2Y_\infty\right) \mathrm{e}^{-2Y_\infty/L_{\mathrm{R}}},$$
$$B_{\mathrm{W}} = L_{\mathrm{R}} \Pi_0 H \left(\mathrm{e}^{-2Y_\infty/L_{\mathrm{R}}} - \mathrm{e}^{-Y_\infty/L_{\mathrm{R}}}\right) - \frac{Q_0}{L_{\mathrm{R}}} \mathrm{e}^{-Y_\infty/L_{\mathrm{R}}}. \tag{4.39}$$

A similar equation for a free front in the full shallow-water equations has been derived separately by Cushman-Roisin et al. [1993] and Nycander et al. [1993], but with A and B given by

$$A_{\mathrm{F}} = \frac{\sqrt{(g'h_2)}^3 - \sqrt{(g'h_1)}^3}{6f_0^2},$$
$$B_{\mathrm{F}} = \frac{g'^2(h_1 + h_2)\beta}{2f_0^2}. \tag{4.40}$$

Here, the Coriolis parameter $f = f_0 + \beta y$ is allowed to vary with latitude, and the front connects two far-field states of depth h_1 and h_2. In the quasi-geostrophic limit $h_1 \to h_2$, A_{F} reduces to the constant term in A_{W}. Comparing (4.39) and (4.40) shows the effect of the coastal boundary on frontal waves, and the difference between the asymptotic regimes (4.4) and (4.5). When the ratio Y_∞/L_{R} is order unity, the coastal boundary decreases the magnitude of the dispersive term A significantly through the addition of the exponential term in A_{W}, which is driven by the image effect. The boundary also gives rise to a background flow B that is otherwise absent when $\beta = 0$, and contains contributions from both the Kelvin-wave driven flow and image vorticity. The treatment of boundary-influenced PV fronts in the full shallow-water equations is an important avenue for future work.

As discussed in §4.3.2.2, the dispersion relation $\omega(k)$ for linear waves can be transformed into a conjugate dispersion relation $\widetilde{\omega}(\widetilde{k})$ for solitary waves by assuming that the solitary wave has an exponential tail. In (4.38), this amounts to replacing

$$A \to -A, \quad k \to \widetilde{k}, \tag{4.41}$$

where $\widetilde{k}$ is the conjugate wavenumber, or inverse half-width, of the solitary wave. The propagation of finite-amplitude waves can therefore be understood using the same framework as linear dynamics. This result may be of interest to researchers who wish to obtain dispersion relations for meanders in a Western boundary current, as was done for the Gulf Stream in Lee and Cornillon [1996] and for the Kuroshio Extension in Tracey et al. [2012]. We also note that Pratt and Stern [1986] model the evolution of Gulf Stream meanders starting from a 'top-hat' frontal profile, which in the present model could be treated analytically using the adaptation of El's technique described in Maiden et al. [2020].

Chapter 5

Hydraulic control of continental shelf waves

This chapter is concerned with barotropic coastal-trapped waves (continental shelf waves, CSWs) generated when a boundary-intensified geostrophic current interacts with an order-one change in shelf width. We extend the coastal front model of the previous chapter to include an idealised continental shelf (a constant-height step of variable offshore extent), which is similar to the rigid-lid channel model studied by Haynes et al. [1993] and Johnson and Clarke [1999]. Recently, Zhang and Lentz [2017] showed that alongshore variation in the continental shelf profile can lead to hydraulic control of coastal-trapped waves when the background flow opposes the direction of phase propagation (see figure 1.3). Here we use the idealised long-wave model to explore the parameter space in greater detail, identify the necessary conditions for control, and analyse the transition from hydraulically-controlled flow to the far-field state including the leading-order effects of dispersion. Contour-dynamic simulations again show that the dispersive long-wave theory captures much of the behaviour of the full quasi-geostrophic system. In the present model the dynamics are driven by the PV jump at the edge of the step and the Burger number $S = 0$. Martell and Allen [1979] study hydraulic control in a similar model, but their analysis is restricted to small deviations in shelf width. The alternative limit, where $S \gg 1$ and the controlling mode is the internal Kelvin wave, is explored in the uniform-PV models of Gill and Schumann [1979] and Dale

and Barth [2001].

Section 5.1 develops the model and governing equations, §§5.2-5.3 analyse the hydraulic and long-wave dispersive equations respectively, including conditions for critical control and the form of the transition between controlled and far-field flow. In the dispersive equation, some transitions are resolved by a DSW and these are analysed in §5.3 using dispersive shock-fitting. Section 5.4 compares theoretical results with numerical simulations of both the dispersive long-wave equation and the full QG system. Discussion and oceanographic context are given in §5.5.

5.1 Model and governing equations

The equation for QG PV conservation over variable topography $b(x, y)$ is

$$\frac{\mathrm{D}}{\mathrm{D}t}\left(\nabla^2\psi - \frac{\psi}{L_\mathrm{R}^2} + \frac{fb}{H}\right) = 0, \tag{5.1}$$

where $L_\mathrm{R} = \sqrt{gH}/f$ is the Rossby radius of deformation, ψ is the QG streamfunction and H is the mean fluid depth far from the shelf. In contrast to previous chapters the present model is barotropic, although the exact same results apply when a lighter, infinitely-deep, quiescent layer is included in $z > H$ (for example, as a $1\frac{1}{2}$-layer atmospheric model). An important difference from previous chapters is that H is now the depth scale for the ocean rather than the active upper layer (say 1000m as opposed to 10m, with L_R correspondingly larger).

Fluid occupies the half-plane $y > 0$, with a vertical coast at $y = 0$ and a flat continental shelf of width $Y_h(x)$ which we write

$$b = \begin{cases} \Pi_0 H/f & 0 < y < Y_h(x), \\ 0 & y > Y_h(x), \end{cases} \tag{5.2}$$

for some $\Pi_0 > 0$. The extension to include a linear continental slope is conceptually straightforward but will not be considered here. We will focus on the case where the shelf-width Y_h is a slowly-varying function of x, and is constant apart from a localised perturbation around $x = 0$. That is, $Y_h(x) = Y_0 - f(x)$, where $f(x) \to 0$ as $|x| \to \infty$ and has its maximum magnitude, Δ, at the origin. In all numerical simulations that follow we will use the particular choice $f(x) = \Delta\,\mathrm{sech}\,(x/W)^2$, where W is a non-dimensional parameter that measures the width of the topographic forcing region and in the long-wave limit required for the analysis is formally large compared to L_R. We place no restriction on the magnitude of Δ. Figure 5.1 shows a schematic of the flow and identifies the geometric parameters.

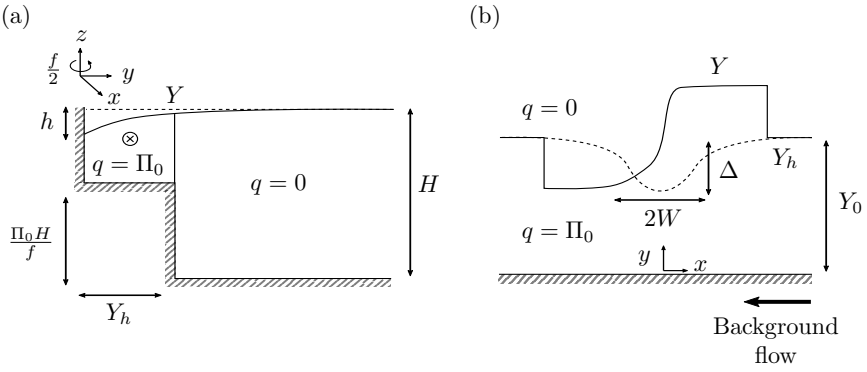

Figure 5.1: A flat continental shelf occupies the region $0 < y < Y_h(x)$, with a vertical coast at $y = 0$. The model ocean is barotropic, with two regions of uniform PV separated by an interface at $y = Y(x,t)$. Motion is driven by a coastal-intensified background current, in this case from right to left. (a) Side view. (b) Plan view; the dashed curve is Y_h and the solid curve is Y.

We will consider the initial-value problem where the fluid starts at rest, so that the initial distribution of PV is

$$q = \begin{cases} \Pi_0 & 0 < y < Y_h(x) \\ 0 & Y_h(x) < y. \end{cases} \tag{5.3}$$

The PV gradient is therefore entirely due to the topography rather than any internal variation of vorticity. With no background flow, $\psi \equiv 0$ and the steady state (5.3) persists for all time. Thus consider a background flow which starts impulsively at $t = 0$, and displaces the PV interface to some $y = Y(x,t)$. This situation can be written compactly as

$$\nabla^2\psi - \frac{\psi}{L_{\mathrm{R}}^2} + \Pi_0 \left(H(Y_h - y) - H(Y - y)\right) = 0, \tag{5.4}$$

where H is the Heaviside function. The PV interface $Y(x,t)$ evolves according to the kinematic boundary condition

$$\frac{\partial Y}{\partial t} = \frac{\mathrm{d}}{\mathrm{d}x}\psi(x, Y(x,t), t), \tag{5.5}$$

so that given a closed expression for $\psi(x, Y, t)$ the entire flow field can be tracked by solving the scalar equation (5.5). In writing (5.5) we have assumed that the interface is at all times a single-valued function of x. This assumption will later be verified through numerical simulations of the full QG system (5.1).

For simplicity we shall restrict discussion to a background flow profile that is monotonically decaying with offshore distance. The appropriate

boundary conditions are

$$\psi = Q_0 \quad \text{on} \quad y = 0, \tag{5.6a}$$

$$\psi \to 0 \quad \text{as} \quad y \to \infty, \tag{5.6b}$$

along with the requirement that ψ and $u = -\psi_y$ are continuous everywhere. In many oceanographic applications it may be more suitable to choose a background flow that is intensified at the shelf-break, and (5.6a) should be modified accordingly. Note that the system (5.1) and boundary conditions (5.6) are symmetric under the following transformation

$$\psi \to -\psi, \quad x \to -x, \quad b \to -b, \quad Q_0 \to -Q_0, \tag{5.7}$$

so that the problem is equivalent to that of a trench of depth b against a vertical wall.

We non-dimensionalise ψ with $|Q_0|$ and horizontal lengths with L_R. While in previous chapters we have scaled horizontal lengths on $L_\mathrm{V} = \sqrt{(|Q_0|/\Pi_0)}$ in order to study vortical effects, here the ratio of the shelf width to Rossby radius is also important and so we have chosen to scale on L_R, noting that L_R is very large in the barotropic model and thus the non-dimensional parameter $a = L_\mathrm{R}/L_\mathrm{V}$ (which appears now in the forcing term rather than the exponent) is expected to satisfy $a \gg 1$ in the real oceans. The choice of L_R as a horizontal length scale also turns out to drastically simplify the analysis that follows. With this scaling, the boundary condition (5.6a) becomes $\psi = Q = \pm 1$ depending on whether the basic flow is to the right ($Q = +1$) or the left ($Q = -1$). For the analytic work below, we also introduce the long-wave co-ordinate $X = x/W$ and slow time $T = t/W$.

5.1.1 The long-wave limit

Expanding ψ in terms of $\epsilon = 1/W$, the field equation (5.4) becomes at leading order

$$\frac{\partial^2 \psi^0}{\partial y^2} - \psi^0 + a^2 \left(H(Y_h - y) - H(Y - y) \right) = 0. \tag{5.8}$$

The solution to (5.8) depends on whether the PV front is on the shelf ($Y < Y_h$) or off the shelf ($Y > Y_h$). For the case where the front is on the shelf,

$$\psi^0(x, y, t) = \begin{cases} Q\mathrm{e}^{-y} + a^2 \sinh(y) \left(\mathrm{e}^{-Y} - \mathrm{e}^{-Y_h} \right), & 0 < y < Y, \\ Q\mathrm{e}^{-y} + a^2 \left[1 - \sinh(y)\mathrm{e}^{-Y_h} - \cosh(Y)\mathrm{e}^{-y} \right], & Y < y < Y_h, \\ Q\mathrm{e}^{-y} + a^2 \left(\cosh(Y_h) - \cosh(Y) \right) \mathrm{e}^{-y}, & y > Y_h, \end{cases} \tag{5.9}$$

while when the front is off the shelf,

$$\psi^0(x,y,t) = \begin{cases} Q\mathrm{e}^{-y} + a^2 \sinh(y)\left(\mathrm{e}^{-Y} - \mathrm{e}^{-Y_h}\right), & 0 < y < Y_h, \\ Q\mathrm{e}^{-y} + a^2\left[-1 + \sinh(y)\mathrm{e}^{-Y} + \cosh(Y_h)\mathrm{e}^{-y}\right], & Y_h < y < Y, \\ Q\mathrm{e}^{-y} + a^2\left(\cosh(Y_h) - \cosh(Y)\right)\mathrm{e}^{-y}, & y > Y, \end{cases} \tag{5.10}$$

upon enforcing continuity of ψ and u at $y = Y$ and $Y = Y_h$, as well as the boundary conditions (5.6). We introduce the index $j = \mathrm{sign}(Y_h - Y)$ to differentiate between the two cases, and write

$$\begin{aligned} \psi^0(x,Y,t) &= Q\mathrm{e}^{-Y} + \frac{a^2}{2}\left[\mathrm{e}^{-(Y+Y_h)} - \mathrm{e}^{-2Y} + j\left(1 - \mathrm{e}^{j(Y-Y_h)}\right)\right] \\ &= Q_e(Y, Y_h), \end{aligned} \tag{5.11}$$

where $Q - Q_e$ is the net along-shore flux of shelf water.

In the hydraulic limit the kinematic boundary condition (5.5) becomes

$$\frac{\partial Y}{\partial t} + C(Y,Y_h)\frac{\partial Y}{\partial x} = \frac{a^2}{2}\left(\mathrm{e}^{j(Y-Y_h)} - \mathrm{e}^{-(Y+Y_h)}\right)\frac{\partial Y_h}{\partial x}, \tag{5.12}$$

a forced nonlinear wave equation with long-wave speed

$$C(Y,Y_h) = -\left.\frac{\partial \psi^0}{\partial y}\right|_{y=Y} = Q\mathrm{e}^{-Y} + \frac{a^2}{2}\left[\mathrm{e}^{-(Y+Y_h)} - 2\mathrm{e}^{-2Y} + \mathrm{e}^{j(Y-Y_h)}\right]. \tag{5.13}$$

As in previous chapters we have reverted to using x and t for ease of notation. From left to right, the terms in (5.13) can be identified as the relative contributions of: background flow, image vorticity due the shelfbreak, image vorticity due to the PV front, and stretching/squashing generated by off- or on-shelf movement of the front. Much of the qualitative behaviour of the hydraulic equation can be understood through C. In particular if $Y > Y_h$ then C is not a monotonic function of Y, with a unique maximum at

$$Y = Y_2 = -\log\left(\frac{Q + a^2\cosh(Y_h)}{2a^2}\right). \tag{5.14}$$

Thus the flux function Q_e may be non-convex when the front is off-shelf. Note that $Y_2 > Y_h$ only when $Q < a^2$ and

$$Y_h < Y_{2,\mathrm{M}} = \log\left(\frac{\sqrt{(1+3a^4)} - Q}{a^2}\right). \tag{5.15}$$

Thus when $Q = 1$ and the background current is in the same direction as CTW phase propagation, compound-wave structures exist when the flow

is dominated by vorticity ($a > 1$), as in §4. However when $Q = -1$ and the background current opposes CTW propagation compound-wave structures exist for all a, provided the shelfbreak Y_h is sufficiently close to the coast. Note also that C_Y is discontinuous at the shelfbreak and, for the case where $Q = -1$, changes sign if $Y_h > Y_{2,\mathrm{M}}$. Thus compound-wave solutions can also occur in the Riemann problem when the front crosses the shelfbreak; although this situation does not arise in the initial-value problem (5.3).

5.1.2 Dispersive effects

At next order in ϵ, the streamfunction correction $\psi^1(x, y, t)$ satisfies

$$\frac{\partial^2 \psi^1}{\partial y^2} - \psi^1 = -\frac{\partial^2 \psi^0}{\partial x^2}, \tag{5.16}$$

which is to be solved subject to continuity of ψ^1 and u^1 at Y and Y_h, and no normal flow at the coast. After some algebra, we find:

$$\begin{aligned}\psi^1(x, Y, t) = &-\frac{a^2}{4} Y'' + \frac{a^2}{4} \mathrm{e}^{-2Y} \left(Y'' - 2Y(Y'^2 - Y'') \right) \\ &+ \frac{a^2}{4} \mathrm{e}^{-(Y+Y_h)} \left(Y(Y_h'^2 - Y_h'') + Y_h Y_h'^2 - Y_h''(1 + Y_h) \right) \\ &+ \frac{a^2}{4} \mathrm{e}^{j(Y-Y_h)} \left(Y(Y_h'^2 - jY_h'') - Y_h Y_h'^2 + Y_h''(1 + jY_h) \right),\end{aligned} \tag{5.17}$$

where primes ($'$) denote differentiation with respect to x. Note that outside the region of topographic forcing, Y_h is constant and (5.17) reverts to (4.17). The conservation law corresponding to (4.19) is

$$\begin{aligned}&\left(\frac{Y^2}{2} \right)_t + \left[Q(Y + 1)\mathrm{e}^{-Y} \right]_x \\ &\quad + \left[\frac{a^2}{2} \left((Y + 1)\mathrm{e}^{-(Y+Y_h)} - \left(Y + \frac{1}{2} \right) \mathrm{e}^{-2Y} + (1 - jY)\mathrm{e}^{j(Y-Y_h)} \right) \right]_x \\ &\quad + \left[\frac{a^2}{2} Y^2 Y_x^2 \mathrm{e}^{-2Y} + \frac{a^2}{8} (Y_x^2 - 2YY_{xx}) \left(-1 + (1 + 2Y)\mathrm{e}^{-2Y} \right) \right]_x \\ &\quad = 0.\end{aligned} \tag{5.18}$$

5.2 The hydraulic equation

Here, we classify the different behaviours of the hydraulic initial-value problem (5.12) in terms of Δ, the shelfbreak perturbation magnitude, and F, a Froude number which is defined below. In addition to the usual steady subcritical, supercritical and critically controlled regimes [Pratt and

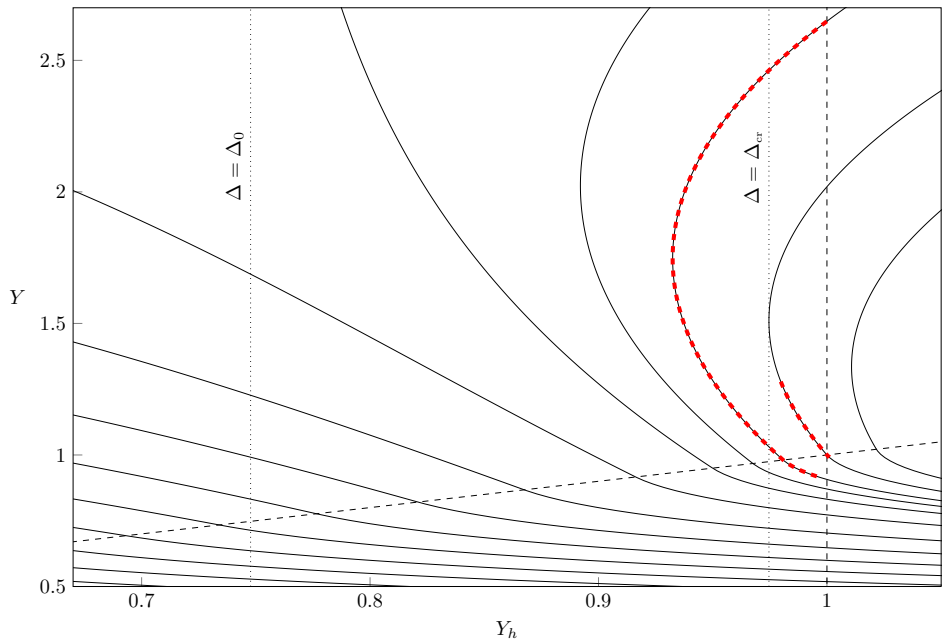

Figure 5.2: Contours of the hydraulic function $Q_e(Y, Y_h)$, for $Q = -1$ and $a = 0.8795$. Steady solutions must lie on a single contour. The dashed lines are $Y = Y_h$ and $Y_h = 1$, and dotted lines show critical values of Δ at which the solution changes type when $Y_0 = 1$. Red dashed curves show examples of supercritical and critically-controlled solutions.

Whitehead, 2008] there is a fourth, unsteady, response that we call an 'offshore plume'.

5.2.1 Steady solutions

Steady solutions to the hydraulic equation (5.12) satisfy

$$Q_e(Y, Y_h) = \Psi, \tag{5.19}$$

for some constant Ψ. Contours of Q_e for the particular choice of parameters $Q = -1$ and $a = 0.8795$ are shown in figure 5.2. For a given value of Ψ and Y_h, there are up to two possible values of Y that satisfy (5.19). Steady solutions must lie on a single contour, and the highlighted (red dashed) contours show examples of the steady solutions selected by the initial-value problem when $Y_0 = 1$, for two different values of Δ.

For small $\Delta < \Delta_{\rm cr}$ the flow evolves to become steady in the forcing region, and the steady state is entirely sub- or supercritical. Transient disturbances thus propagate away from the forcing region in one direction only and the initial condition $Y = Y_0$ persists on the other side so that

$$\Psi = Q_e(Y_0, Y_0) = -\mathrm{e}^{-Y_0}. \tag{5.20}$$

The right-most dashed contour in figure 5.2 shows an example of steady supercritical flow when $Y_0 = 1$ and $\Delta = 0.025$. The solution starts at $(Y_h, Y) = (1, 1)$ and follows the contour (5.20) to the maximum perturbation $Y_h = 0.975$, before retracing the path to $(1, 1)$. The solution is therefore symmetric about the origin and the front is off-shelf ($Y > Y_h$) throughout.

If $\Delta > \Delta_{\rm cr}$ is sufficiently large then the contour through (Y_0, Y_0) does not extend to the maximum displacement $Y_h = Y_0 - \Delta$ (which we denote Y_Δ) and instead the steady solution selects the unique contour that satisfies

$$C(Y, Y_\Delta) = 0. \tag{5.21}$$

The long-wave speed vanishes at the maximum topographic displacement, which is thus a control point for the flow [Pratt and Whitehead, 2008]. An example with $\Delta = 0.05$ is shown as the left-most highlighted contour in figure 5.2. The solution traces the entire contour, so that Y is monotonic and asymmetric as a function of Y_h. Note that $Y \neq Y_0$ when $Y_h = Y_0$ so that critically controlled flow alters the far-field state both up- and downstream and information propagates away from the shelfbreak perturbation in both directions.

Now, for a small perturbation of the far-field state $Y = Y_h = Y_0$,

$$C \sim Q\mathrm{e}^{-Y_0} - \frac{a^2}{2}\mathrm{e}^{-2Y_0} + \frac{a^2}{2}. \tag{5.22}$$

Equation (5.22) vanishes when $F = 1$, where

$$F = \frac{-Q}{a^2 \sinh(Y_0)} \tag{5.23}$$

is the Froude number for this problem. The condition $F = 1$ can only be satisfied if $Q = -1$ and thus hydraulic control is only possible when the background current opposes CTW propagation. One can also show that control only occurs when the perturbation is a localised narrowing in shelf width ($\Delta > 0$) as follows. In order for disturbances to propagate away from the forcing region, the critically-controlled solution must have $C > 0$ for large positive x and $C < 0$ for large negative x. Since C is dominated by the the term due to the front moving on- or off the shelf, we can conclude that $Y > Y_h$ for large positive x (vortex stretching generates $C > 0$) and $Y < Y_h$ for large negative x, so that $Y_x > 0$ in controlled flow. Writing the steady version of (5.12) as

$$\frac{\partial Y}{\partial x} = \frac{Y_h'(x)}{C(Y, Y_h)} \frac{\partial Q_e}{\partial Y_h}, \tag{5.24}$$

and noting that $\partial Q_e/\partial Y_h$ is always positive, we see that in critically-controlled flow C and $Y_h'(x)$ have the same sign. That is, $Y_h'(x) > 0$ for x positive and the perturbation must be a local decrease in shelf width. From now on we will restrict our attention to $\Delta > 0$ and $Q = -1$ and describe $x > 0$ as 'upstream'. Critically-controlled flows are subcritical ($C > 0$, $F < 1$) upstream of the shelfbreak perturbation and supercritical ($C < 0$, $F > 1$) downstream. In completely supercritical flow with $C < 0$ everywhere, $Y_h'(x)$ and Y_x have opposite signs and the front is displaced off the shelf (see figure 5.2), while in subcritical flow the front is on the shelf.

Haynes et al. [1993] and Johnson and Clarke [1999] study the related problem of hydraulically-controlled flow in a stepped channel, and show that several other types of controlled solutions can occur. The fact that these do not appear in the present geometry suggests that they rely on an opposing wall to support their existence, as can be deduced by figure 2 of Johnson and Clarke [1999].

5.2.2 Offshore plumes

Assuming that the front is off-shelf at the control point, solving the criticality condition (5.21) gives

$$Y = -\log\left(\frac{-1}{a^2} + \cosh\left(Y_\Delta\right)\right). \tag{5.25}$$

This is the locus of turning points in the hydraulic contours of figure 5.2. For $a < 1$, the control point $Y \to \infty$ as $Y_\Delta \to \operatorname{acosh}(1/a^2)$ and the critical solution is no longer valid. Thus for $\Delta > \Delta_0 = Y_0 - \operatorname{acosh}(1/a^2)$ the contour through (Y_0, Y_0) does not reach Y_Δ, but there is no contour which has a turning point at $Y = Y_\Delta$ and so the solution never becomes steady in the source region. Instead, the flow develops into an ever-expanding 'offshore plume' similar to the growing solutions for coastal outflow plumes discussed in Johnson et al. [2017] and §2. As in Johnson et al. [2017], offshore plumes only exist when $a < 1$ and the flow induced by vortex stretching as shelf water crosses the shelfbreak is not sufficient to overcome the background current. Instead, the incoming flow is directed principally off shore, and Y grows indefinitely in the forcing region. Note however that due to the definition of L_R as the barotropic radius of deformation, a is likely to be large in the real ocean. Offshore plumes are nonetheless an interesting feature of the present model, having no equivalent in free-surface hydraulic flow which always becomes steady. They are somewhat related to the 'supercritical leap' of Haynes et al. [1993] in that the flow

attains two different supercritical states on either side of the topographic forcing region.

Numerical simulations performed using the same scheme as in §4 show that at large times the shape of the front in the source region is approximately constant. Thus we can obtain an approximate description of the offshore plume through the ansatz

$$Y(x,t) = Y_p(x) + g(t). \tag{5.26}$$

Ignoring terms proportional to $\exp(-2Y)$ in (5.12) and only considering regions where $Y > Y_h$ we have

$$Y_\Delta = \left[(1 - a^2\cosh(Y_h))Y_x + a^2\sinh(Y_h)Y_h'(x)\right]\mathrm{e}^{-Y}. \tag{5.27}$$

Substituting (5.26) gives the separable equation

$$\mathrm{e}^{g(t)}g'(t) = \left[(1 - a^2\cosh(Y_h))Y_p'(x) + a^2\sinh(Y_h)Y_h'(x)\right]\mathrm{e}^{-Y_p(x)}, \tag{5.28}$$

where the left-hand side is a function of t alone and the right-hand side is a function of x and so both are equal to α, a constant. Solving each side separately we find

$$g(t) = \log(t - t_0) + \log\alpha, \tag{5.29a}$$

and, via the substitution $h(x) = \exp(Y_p)/(-1 + a^2\cosh(Y_h))$,

$$Y_p(x) = \log\left[(-1 + a^2\cosh(Y_h))/(x - x_0)\right] - \log\alpha, \tag{5.29b}$$

so that the asymptotic evolution of the plume at late times is

$$Y(x,t) = \log\left[(-1 + a^2\cosh(Y_h))(t - t_0)/(x - x_0)\right]. \tag{5.30}$$

The solution must be bounded, so the numerator and denominator vanish at the same point and x_0 can be found by solving the equation

$$Y_h(x_0) = \operatorname{acosh}(1/a^2), \tag{5.31}$$

that is, $Y_h(x_0) = Y_0 - \Delta_0$.

Figure 5.3 shows an offshore plume at $t = 15000$. Contours of the streamfunction are plotted in (a), and show that there is a slow, broad recirculation of shelf water in the region of topographic forcing. The edge of the plume is shown as a thick black curve, and agrees well with the asymptotic solution (red dashed curve) in $x > x_0$. Figure 5.3(b) shows the magnitude of the alongshelf flux of shelf water. In $x > 130$ the flow is undisturbed and the flux of shelf water is $1 - \exp(-Y_0)$, while in $x < -20$ the flux is $1 - a^2/2$ (bottom dotted line) which is the asymptotic value of Q_e as $Y \to \infty$. Note that the choice of $\Delta = 0.7$ is somewhat unrealistic, but that by (5.25) off-shore plumes develop whenever $\Delta > Y_0 - \operatorname{acosh}(1/a^2)$.

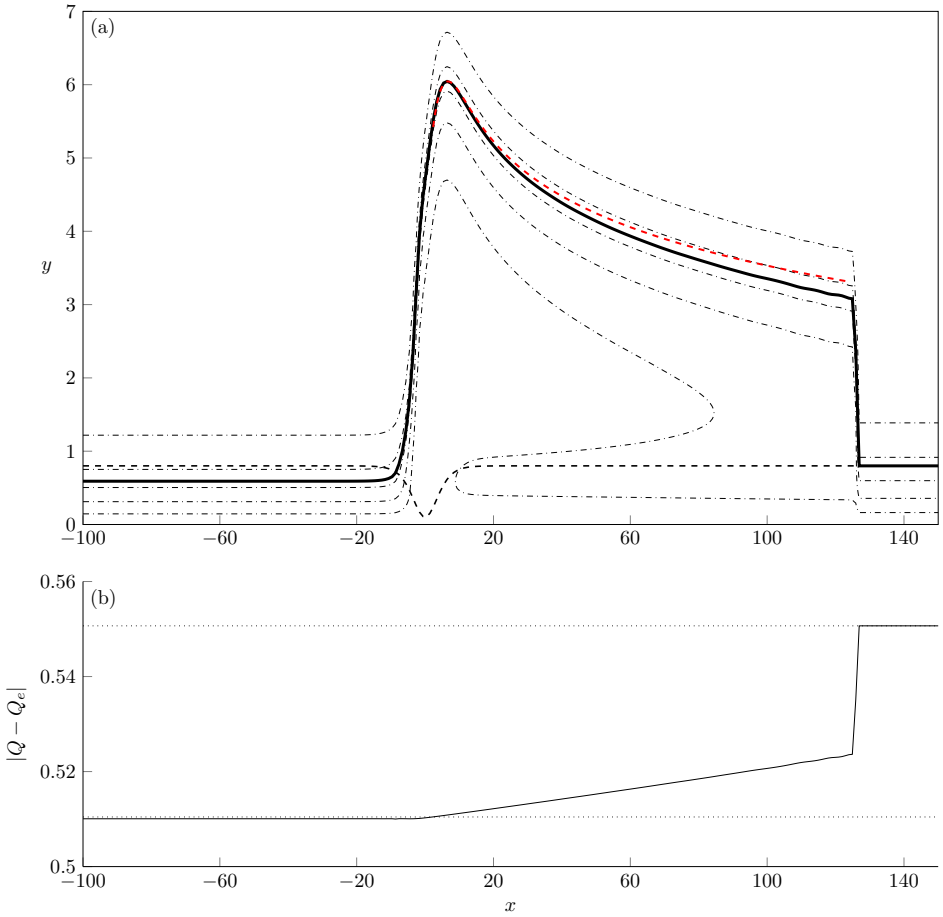

Figure 5.3: Offshore-plume solution to the hydraulic initial-value problem (5.12). (a) Contours of the streamfunction ψ^0 at $t = 15000$ (dash-dotted, contour interval is 0.15). The thick black curve is the frontal position Y, the red dashed curve is the asymptotic solution (5.30) and the black dashed curve is the topography $Y_h(x)$. (b) The magnitude of the alongshore flux of shelf water. The net flux is from right to left. Parameters are $Y_0 = 0.8$, $\Delta = 0.7$, $a = 0.9895$ and $w = 5$.

5.2.3 Conditions for critical control

In order to identify the regions of parameter space where the flow is critically controlled, it is convenient to discuss the problem in the (Δ, F)-plane. Given the far-field shelf-width Y_0 we seek the range of Froude numbers,

$$F_-(\Delta) < F < F_+(\Delta),$$

for which critical flow occurs. The curves $F_\pm$ mark the transition from critical to non-critical flow, and are derived by simultaneously solving the criticality condition (5.21) and the condition for steady, non-critical flow (5.20). These boundaries can also be posed in terms of the parameter a. We derive expressions for $F_\pm$ by treating Q_e and C as polynomials in

$Z = \exp(-Y)$.

First, suppose that the flow is critical. If the front lies off the shelf at the maximum constriction, then solving the criticality condition gives (5.25). We call this kind of flow, where the front is off-shelf at the control point Y_Δ, off-shelf controlled. In the alternative situation, where the flow is on-shelf controlled, Y is found by solving the following cubic equation in Z,

$$-a^2 Z^3 + \left(\frac{a^2}{2}\mathrm{e}^{-Y_\Delta} - 1\right) Z^2 + \frac{a^2}{2}\mathrm{e}^{-Y_\Delta} = 0, \tag{5.32}$$

which has at most one root in $Z > 0$. (The cubic polynomial $f(Z)$ defined by (5.32) is positive when $Z = 0$, and either $Z = 0$ is a local minimum or $f'(Z) < 0$ for all $Z > 0$.) The transition between (5.25) and (5.32) occurs when

$$Y_\Delta = Y_1 = \log\left(\frac{1 + \sqrt{1 + a^4}}{a^2}\right), \tag{5.33}$$

with off-shelf control occurring for $Y_\Delta < Y_1$.

To find the boundaries $F_\pm(\Delta)$, we solve the criticality condition (5.21) and the condition for non-critical steady flow (5.20) simultaneously. For each pair (Y_0, Y_Δ) this gives two values of a (equivalently the Froude number F) at which the flow transitions from being non-critical to critical. For off-shelf control,

$$a^2 = 2\frac{Z_\Delta^3 - 2Z_0 Z_\Delta^2 + Z_\Delta - 2Z_\Delta^2\left[2Z_0(\cosh(Y_0) - \cosh(Y_\Delta))\right]^{1/2}}{(Z_\Delta^2 - 1)^2}, \tag{5.34a}$$

where we have introduced $Z_\Delta = \exp(-Y_\Delta)$ and $Z_0 = \exp(-Y_0)$. For fixed Y_0, equation (5.34a) is used to give the supercritical boundary for controlled flow, $F_+(\Delta)$. For on-shelf control,

$$a^2 = \frac{2(Z_0 - Z)}{(1 - Z^2)(Z_\Delta/Z - 1)}, \tag{5.34b}$$

where Y is given by the solution to (5.32). This gives the subcritical boundary $F_-(\Delta)$.

For sufficiently wide shelves ($Z_0 < 1/2$), the supercritical boundary $F_+(\Delta)$ is non-monotonic with a maximum at Δ_0. Offshore plumes occur when $\Delta > \Delta_0$ and $F_\mathrm{G}(\Delta) < F < F_\mathrm{max}$, where

$$F_\mathrm{max} = \frac{1}{1 - Z_0^2}, \tag{5.35a}$$

$$F_\mathrm{G}(\Delta) = \frac{\cosh(Y_0 - \Delta)}{\sinh(Y_0)}. \tag{5.35b}$$

Figure 5.4 summarises the above discussion through representative examples of how the (Δ, F)-plane is divided for (a) a shelf where $Z_0 > 1/2$

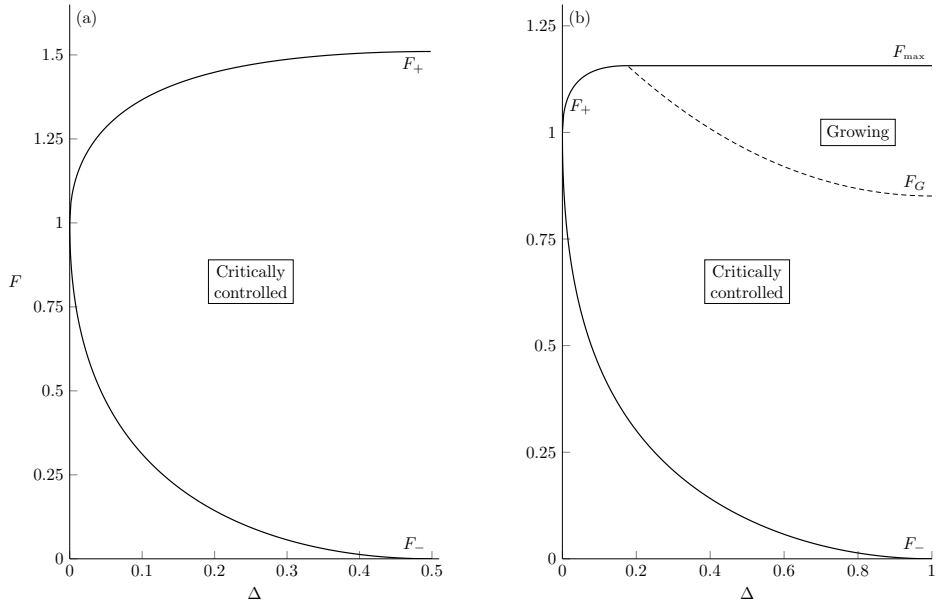

Figure 5.4: Regions of the (Δ, F)-plane where the flow is critically controlled. (a) The maximum shelf-width is $Y_0 = 0.5$. The flow is critically controlled when F lies between the solid curves $F_\pm(\Delta)$. (b) $Y_0 = 1$. The dashed curve is $F_{\rm G}(\Delta)$, and offshore plumes occur when $F_{\rm G} < F < F_{\max}$.

and offshore plumes do not exist, and (b) a shelf with $Z_0 < 1/2$. Solid curves show the boundaries of the regions of non-critical flow, and the dashed curve in (b) is $F_{\rm G}(\Delta)$, the boundary between critically-controlled flow and offshore plumes. For shelves where offshore plumes do not occur, the maximum Froude number for critically-controlled solutions is

$$F_{\max} = \frac{4Z_0}{1+Z_0}, \tag{5.36}$$

which occurs at $\Delta = Y_0$.

5.2.4 Transition to the far field solution

Outside the region of topographic forcing, the hydraulically-controlled flow displaces the PV front Y from its initial position Y_0 to a new, constant, location that we denote $Y_{\rm u/d}$ for $x > 0$ and $x < 0$ respectively. By the heuristic arguments of §5.2.1 we expect that controlled solutions are off-shelf upstream and on-shelf downstream, so that $Y_{\rm u} > Y_0$ and $Y_{\rm d} < Y_0$. If the flow is off-shelf controlled then

$$\begin{aligned} {\rm e}^{-Y_{\rm u}} = &-\frac{1}{a^2} + \cosh\left(Y_0\right) \\ &- \left[\left(\cosh\left(Y_0\right) - \cosh\left(Y_\Delta\right)\right)\left(\cosh\left(Y_0\right) + \cosh\left(Y_\Delta\right) - \frac{2}{a^2}\right)\right]^{1/2}. \end{aligned} \tag{5.37}$$

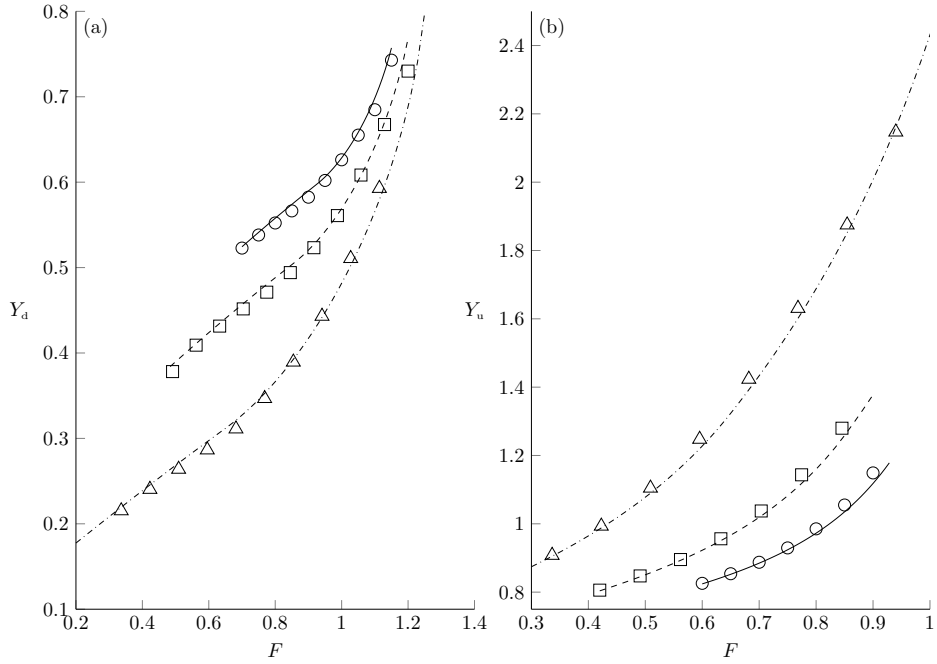

Figure 5.5: Adjusted frontal position in controlled flow (a) downstream and (b) upstream of the topographic perturbation, for $Y_0 = 0.8$ and various values of Froude number F and topographic perturbation magnitude Δ. Shown are the analytic solutions (curves) and numerical solutions to the dispersive long-wave equation (symbols). The solid curves and circles are for shelves with $\Delta = 0.05$, dashed curves and squares with $\Delta = 0.1$ and dash-dot curves and triangles with $\Delta = 0.25$.

To obtain Y_u in on-shelf controlled flow, or Y_d in either case, requires the solution of at least one cubic equation and yields an expression that is too complex to include here. The dependence of $Y_{u/d}$ on F and Δ, for the case where $Y_0 = 0.8$, is shown in figure 5.5. Increasing F moves the front offshore both downstream and upstream of the topographic perturbation, while increasing Δ leads to a more extreme displacement of the front relative to the shelfbreak (further offshore upstream, further onshore downstream).

The transition between the topographically-influenced state $Y_{u/d}$ and the undisturbed far-field value Y_0 may be accomplished in one of three ways, depending on the value of the long-wave speed $C(Y, Y_0)$ on either side of the transition. The three possible transitions are: shock, rarefaction, and shock-rarefaction. A shock that connects Y_0 to a value Y propagates at speed

$$V(Y) = \frac{Q_e(Y, Y_0) - Q_e(Y_0, Y_0)}{Y_0 - Y}. \tag{5.38}$$

First, consider the downstream transition. As noted above, $Y_d < Y_0$ and so C is a monotonic increasing function of Y. Thus the downstream transition is always resolved by a shock, with speed $V(Y_d) < 0$. Next,

consider the upstream transition. For $Y > Y_0$, C has a maximum at $Y = Y_2$ (given by (5.14) with $Y_h = Y_0$). If $Y_\mathrm{u} < Y_2$, C is monotonic increasing and the transition is again resolved by a shock with speed $V(Y_\mathrm{u})$. Since $Y_\mathrm{u} > Y_0$ and $V > 0$, rearranging (5.38) shows that $Q_e(Y_\mathrm{u}) < Q_e(Y_0)$ and the transport of shelf water in the controlled solution is reduced compared to the far-field background flow. Thus critical flow 'blocks' the background current by reducing the flow of shelf water towards the topographic perturbation (figure 5.3 shows that the same occurs in offshore plumes).

If $Y_0 > Y_2$ then C is monotonic decreasing and the transition is resolved by a rarefaction. This occurs when

$$F < F_\mathrm{R} = \frac{1 - 3Z_0^2}{1 - Z_0^2}, \tag{5.39}$$

so that, for F sufficiently small and $Z_0 < 1/\sqrt{3}$, critically-controlled flow is resolved upstream by a rarefaction. In the remaining case, where $Y_0 < Y_2 < Y_\mathrm{u}$, C has an interior maximum within the transition and there are three possibilities:

1. $C(Y_0, Y_0) > C(Y_\mathrm{u}, Y_0)$. A simple-wave rarefaction cannot connect Y_u and Y_0 because C has an interior extremum, so the transition is resolved by a shock-rarefaction.

2. $C(Y_0, Y_0) < C(Y_\mathrm{u}, Y_0)$ and $V(Y_\mathrm{u})$ satisfies the Lax entropy condition

$$C(Y_0, Y_0) < V(Y_\mathrm{u}) < C(Y_\mathrm{u}, Y_0).$$

   The transition is resolved by a simple shock.

3. $C(Y_0, Y_0) < C(Y_\mathrm{u}, Y_0)$ and $V(Y_\mathrm{u}) > C(Y_\mathrm{u}, Y_0)$. In this case, characteristic curves collide but a simple shock does not satisfy the Lax entropy condition so the transition is resolved by a shock-rarefaction. The intermediate value of Y at which the shock joins the rarefaction can be computed as in §4.2.

The boundary that determines whether the transition is resolved by a shock or a shock-rarefaction can be determined numerically by checking the conditions above. Figure 5.6 shows representative examples of each type of solution, all with $Y_0 = 0.8$. The solutions are presented in (Δ, F)-space in (a), following figure 5.4. The horizontal dotted line is F_R, and the dotted curve is the boundary between critical flows that are resolved upstream by a shock, and those resolved by a shock-rarefaction. An example of each type of solution is shown in (b)-(g). Subplots (d), (e) and (g) are critically

Subplot	Type	F	Δ	a	t
(b)	Supercritical	1.4	0.4	0.9	500
(c)	Offshore plume	1.2	0.6	0.97	2 000
(d)	Shock	0.9	0.1	1.12	1 200
(e)	Shock-rarefaction	0.9	0.4	1.12	1 200
(f)	Subcritical	0.2	0.1	2.37	40
(g)	Rarefaction	0.2	0.5	2.37	200

Table 5.1: Details of the different initial value problems displayed in figure 5.6. In all cases $Y_0 = 0.8$.

controlled, and are all resolved downstream by a shock (not visible in (d) or (e)). Subplot (c) shows an offshore plume, and subplots (b) and (f) are super- and sub-critical flows respectively. The parameters for each run are summarised in table 5.1.

5.3 The dispersive equation

5.3.1 Steady solutions

The dispersive evolution equation may be solved numerically using the same method as in §4.3, employed here with an artificial damping term at the edge of the domain to allow for longer integration times. As in the outflow problem of Johnson et al. [2017], the dispersive initial-value problem selects a different controlled solution to that predicted by hydraulic theory. Figure 5.5 shows that this discrepancy is generally small. In all cases, the difference between the hydraulic values of $Y_{\mathrm{u/d}}$ and those computed by the spectral method is less than 10% (in most cases it is much less) so that the hydraulic predictions may be used in the analysis of dispersive shock-waves below. However, the differences between the hydraulic and dispersive steady solutions can be resolved by modifying the criticality condition (5.21) to account for the effects of dispersion. The steady dispersive equation is

$$\psi^0 + \epsilon^2 \psi^1 = \Psi, \tag{5.40}$$

for some constant Ψ, where $\epsilon = 1/W$ is the long-wave parameter. Differentiating (5.40) with respect to x gives

$$\psi^0_x + \epsilon^2 \psi^1_x + Y'(x)\left(\psi^0_Y + \epsilon^2 \psi^1_Y\right) = 0, \tag{5.41}$$

where ψ_x vanishes at $x = 0$ for symmetric topography (as can be seen by direct computation using (5.17)). Anticipating that $Y'(0)$ is non-zero in

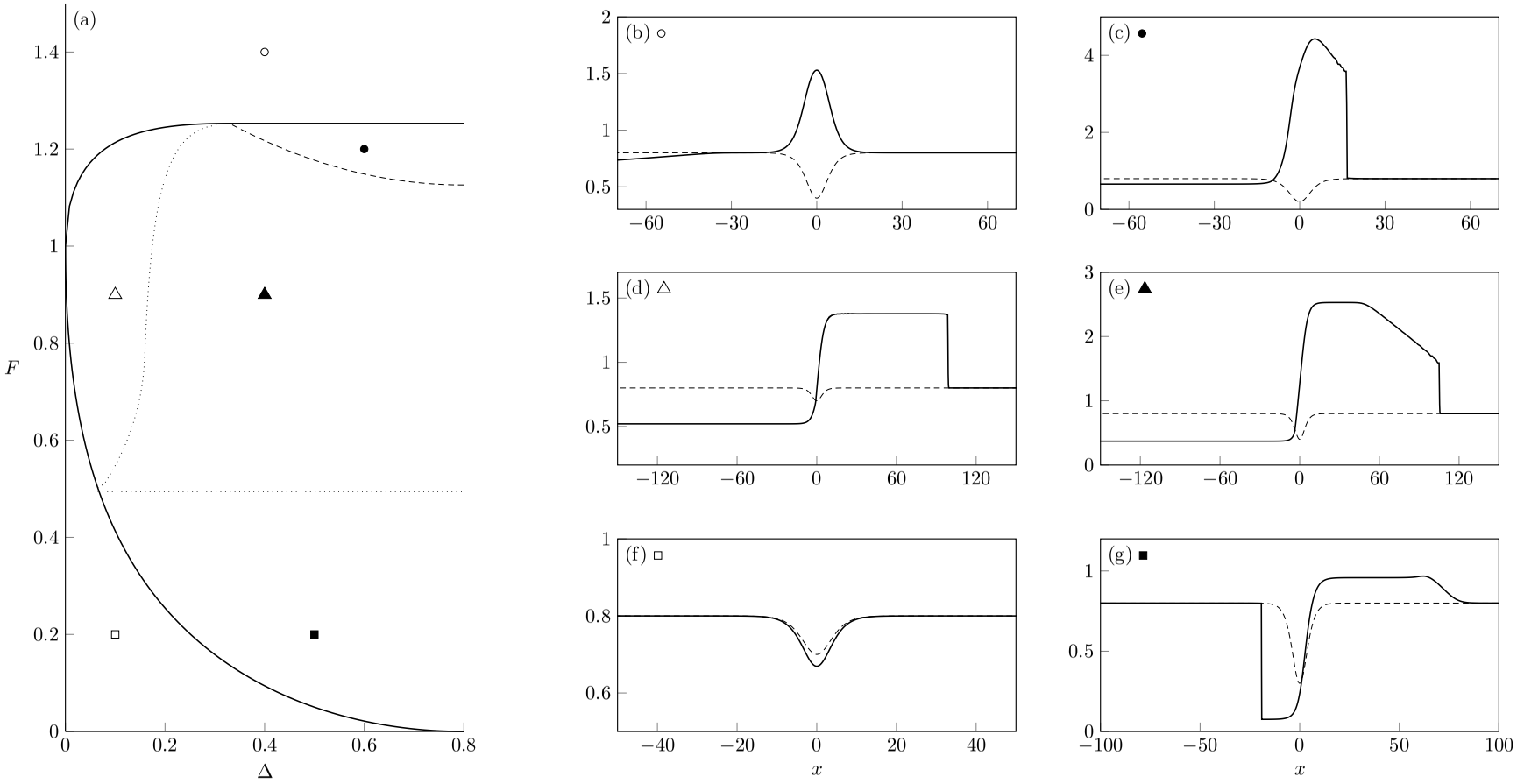

Figure 5.6: Representative examples of the initial value problem with $Y_0 = 0.8$. (a) Classification of the solution in (Δ, F)-space as in figure 5.4. The dotted curves show the boundaries where the upstream transition changes type. (b)-(g) Examples of each type of solution. The black dashed curve is the shelfbreak $Y_h(x)$ and the solid curve is the location of the front, $Y(x,t)$. Symbols correspond to the location of the solution in (Δ, F)-space, and full details are given in table 5.1.

critical flow, the criticality condition for the dispersive equation is

$$C^0 + \epsilon^2 C^1 \Big|_{x=0} = 0, \tag{5.42}$$

where $C^1 = -\psi^1_Y$ can be computed from (5.17) using

$$(Y'')_Y = Y'''/Y', \quad (Y')^2_Y = 2Y''.$$

Note that C^1 depends on Y''_h, so the dispersive critical solution depends on the curvature of the topography at $x = 0$ as well as the magnitude of the constriction.

The steady solution selected by the dispersive equation, and indeed in contour dynamic (CD) simulations of the full QG problem, satisfies (5.42). However following Johnson and Clarke [1999] it is simpler to solve the steady equation (5.40) without consideration of (5.42), and verify criticality afterwards. Numerical solutions of (5.40) are computed by truncating the domain at $x = \pm L$ for large L, and initially estimating $Y(L)$ as the hydraulic value $Y_{\rm u}$. This gives an initial guess for $\Psi = \psi^0(Y_{\rm u}, Y_0)$. Equation (5.40) is then integrated from $x = L$ to $x = 0$ with the boundary conditions $Y(L) = Y_{\rm u}$ and $Y'(L) = 0$, in order to give the subcritical flow and determine $Y(0)$. Since Ψ is known, the supercritical flow in $x < 0$ may be found by solving (5.40) as a boundary-value problem using the known value of $Y(0)$ and the boundary condition $Y'(-L) = 0$. The combined solution is necessarily continuous at the origin, but in general Y' is discontinuous. The value of $Y(L)$ (and hence Ψ) is iterated on using Newton's method until $Y'(0)$ is continuous. By (5.17), this also enforces continuity of $Y''(0)$. Figure 5.7 shows an example where the upstream hydraulic and dispersive states differ by 2%. The red dashed curve is the critical dispersive solution, while the black curves show numerical integrations of the full QG problem (solid curve) and the long-wave dispersive equation (dash-dotted curve) at $t = 1000$. The hydraulic steady solution is shown dotted for comparison. Apart from the presence of small-amplitude waves upstream in the time-dependent solutions all three curves with finite ϵ are identical, confirming that first-order dispersive effects are sufficient to capture the quantitative behaviour of the QG equation.

5.3.2 Transition to the far-field

In the full QG system, dispersion prevents shocks from forming. Instead, transitions between controlled flow and the far-field solution are resolved by a slowly modulated wave-train which can be accurately modelled by dispersive long-wave theory. In particular we may use dispersive

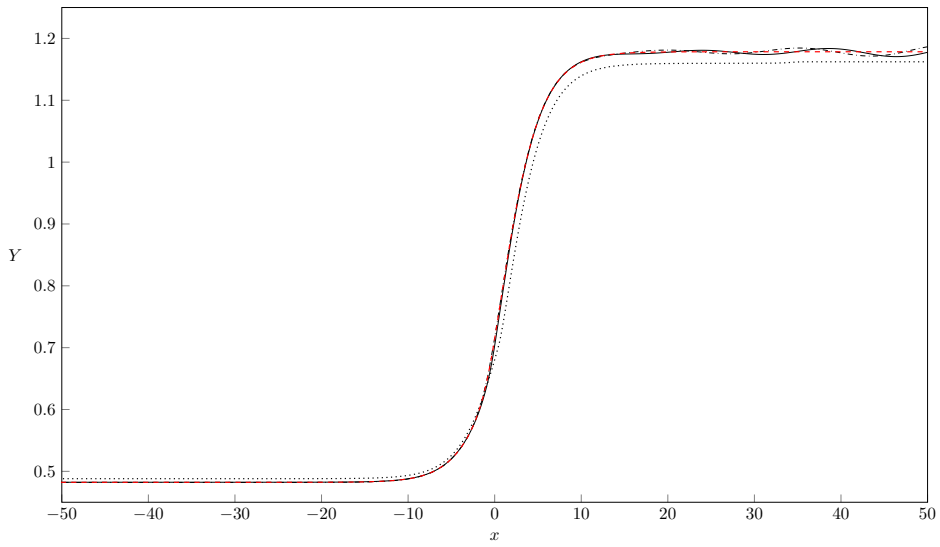

Figure 5.7: Dispersive critically-controlled solution with $Y_0 = 0.8$, $\Delta = 0.1$, $F = 0.8$ and $\epsilon = 0.2$. The solid and dash-dotted black curves show the solution at $t = 1000$ for the full QG and dispersive long-wave equations respectively, and the dashed red curve is the numerically computed steady dispersive solution. The critical hydraulic solution is shown dotted for comparison.

shock-fitting to extract the key parameters of the wavetrain under the assumption that it is a fully-formed DSW. The same technique also identifies the range of parameters for which transitions are resolved by 'partial DSWs', expanding modulated wave-trains which remain attached to the topographic perturbation much like the standing lee waves of Martell and Allen [1979] and Zhang and Lentz [2017].

5.3.2.1 Travelling wave solutions

We will first set out some basic properties of travelling wave solutions to the dispersive equation, applicable outside the forcing region where $Y_h \equiv Y_0$ is constant. The dispersion relation for linear waves of wavenumber k propagating on a background Y_∞ is

$$\omega = C(Y_\infty, Y_0)k - \mathcal{G}(Y_\infty)k^3, \tag{5.43}$$

where

$$\mathcal{G}(Y) = \frac{a^2}{4}\left[1 - \mathrm{e}^{-2Y}(1 + 2Y)\right] \tag{5.44}$$

is always positive (c.f. equation (4.28)). The soliton dispersion relation [Kamchatnov, 2019] is

$$\widetilde{\omega} = C(Y_\infty, Y_0)\widetilde{k} + \mathcal{G}(Y_\infty)\widetilde{k}^3, \tag{5.45}$$

for $\widetilde{k}$ the half-width of the solitary wave. Comparing soliton and linear phase speeds shows that DSWs are always oriented with linear waves on the left-hand side. In potential form, the dispersive long-wave equation is

$$\begin{aligned}\mathcal{G}(Y)(Y')^2 &= a^2\mathrm{e}^{-2Y} + 2(2 - a^2\mathrm{e}^{-Y_0})\mathrm{e}^{-Y} - 2a^2\mathrm{e}^{j(Y-Y_0)} \\ &\quad + 4a^2\min(Y, Y_0) + 2sY^2 + \alpha Y + E \\ &= \mathcal{V}(Y, Y_0; s, \alpha, E). \end{aligned} \tag{5.46}$$

Here primes ($'$) denote differentiation with respect to the moving co-ordinate $\xi = x - st$, s is the speed of the travelling wave and α and E are constants of integration. The behaviour of travelling-wave solutions is determined by the number and type of roots of the function $\mathcal{V}$, with solitary waves requiring that Y_∞ is a local minimum of $\mathcal{V}$. The potential function (5.46) can be analysed in much the same way as was done in §4.3.

5.3.2.2 Compound-wave transitions

When the upstream transition crosses the inflexion point Y_2, kink solitons appear on the right-hand side of the transition and connect $Y_0 < Y_2$ to a conjugate state $Y_K > Y_2$. Given a and Y_0 we seek the pair (s_K, Y_K) such that $\mathcal{V}(Y_K) = \mathcal{V}'(Y_K) = 0$, with α and E determined by the requirement that $Y_0 = Y_\infty$ is also a double-root of $\mathcal{V}$. The compound-wave structure is completed by a secondary transition from Y_K to Y_u. Since $Y_K, Y_\mathrm{u} > Y_2$, C is monotonic decreasing over this range and transitions with $Y_K < Y_\mathrm{u}$ are resolved by a rarefaction-kink (denoted R|K). Similarly, transitions with $Y_K > Y_\mathrm{u}$ are resolved by a depression DSW-kink (DSW$^-$|K).

A representative example of each type of compound-wave transition is shown in figure 5.8. In (a), the transition is resolved by a rarefaction-kink. The kink is at $x \approx 300$, and is connected to the rarefaction by a plateau at $Y = Y_K$ (horizontal dotted line). In (b), the kink connects to Y_u via a DSW$^-$. For this set of parameters, the difference between Y_K and Y_u is small so a zoom of this transition is shown in (c), where the upper and lower horizontal dotted lines show Y_K and Y_u respectively.

5.3.2.3 Dispersive shock-fitting

Following the same arguments as in §4, the Riemann problem in the dispersive long-wave equation is amenable to analysis via dispersive shock-fitting. Assuming that the time taken for the controlled solution to be established over the topography is much less than that required for the full development of a DSW, the same procedure may in principle be used to

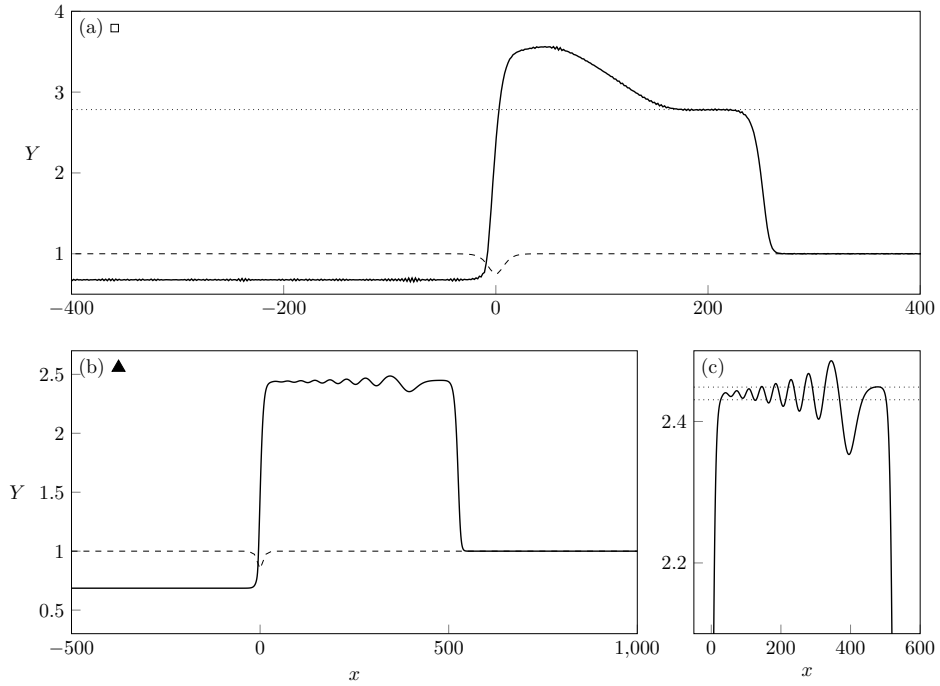

Figure 5.8: Compound-wave transitions in the dispersive equation. In both cases, $Y_0 = 1$ and $\epsilon = 0.1$. (a) The upstream transition is resolved by a R|K. The horizontal dotted line shows Y_K. (b) The upstream transition is resolved by a DSW$^-$|K. Horizontal dotted lines in the inset (c) show the hydraulic upstream state Y_u and kink level Y_K. Symbols in (a) and (b) correspond to figure 5.9(a), which shows the location of the solutions in the (Δ, F) plane. Full details are given in table 5.2.

Subplot	Type	F	Δ	a	ϵ	t
5.8(a)	R|K	1	0.25	0.93	0.1	10 000
5.8(b)	DSW$^-$|K	0.96	0.15	0.91	0.1	16 000
5.9(b)	Upstream attached	1	0.05	0.92	0.2	10 000
5.9(c)	Both detached	0.9	0.05	0.97	0.1	4 500
5.9(d)	Downstream attached	0.75	0.03	1.07	0.2	2 500

Table 5.2: Details of the initial value problems displayed in figures 5.8 and 5.9. In all cases $Y_0 = 1$.

predict the key parameters of DSWs that arise from transitions between critical and far-field flow in the present initial-value problem [El et al., 2009]. However we will show below that the downstream solitary wave speed has a local minimum at $F = F_\mathrm{cr}$, so that for $F < F_\mathrm{cr}$ the downstream wave-train cannot be described using dispersive shock-fitting.

DSWs develop upstream when the hydraulic equation predicts that the transition will be resolved by a simple shock. Thus for a given set of parameters $\{Y_0, Y_\Delta, F\}$ we apply El's technique with $Y_- = Y_\mathrm{u}$ and $Y_+ = Y_0$,

where $Y_\mathrm{u} > Y_0$ so that the leading solitary wave is one of elevation. The trailing linear and leading solitary wavenumbers are

$$k_\mathrm{u}^2 = \frac{2}{3\mathcal{G}(Y_\mathrm{u})^{2/3}} \int_{Y_0}^{Y_\mathrm{u}} \frac{C'(Y)}{\mathcal{G}(Y)^{1/3}}\,\mathrm{d}Y, \tag{5.47a}$$

$$\widetilde{k}_\mathrm{u}^2 = \frac{2}{3\mathcal{G}(Y_0)^{2/3}} \int_{Y_0}^{Y_\mathrm{u}} \frac{C'(Y)}{\mathcal{G}(Y)^{1/3}}\,\mathrm{d}Y, \tag{5.47b}$$

and the propagation speeds of the upstream DSW edges are

$$s_\mathrm{u} = \left.\frac{\partial\omega}{\partial k}\right|_{Y_\mathrm{u},\ k_\mathrm{u}}, \qquad \widetilde{s}_\mathrm{u} = \frac{\widetilde{\omega}(Y_0, \widetilde{k}_\mathrm{u})}{\widetilde{k}_\mathrm{u}} \tag{5.48}$$

respectively. In some cases, $s_\mathrm{u} < 0$ so that the linear end of the DSW is predicted to enter the region of topographic forcing. Numerical simulations show that in this case the upstream transition is resolved by a partial DSW, which remains attached to the topography and continuously generates waves at the upstream edge of the forcing region. Partial DSWs also occur in free-surface flow over an obstacle, as was shown for the Su-Gardner (dispersive shallow-water) equations by El et al. [2009]. When the upstream transitions is resolved by a DSW$^-$|K we may apply El's technique to a secondary Riemann problem with $Y_- = Y_\mathrm{u}$ and $Y_+ = Y_K$.

Assuming that the downstream transition is resolved by a DSW, we have

$$k_\mathrm{d}^2 = \frac{2}{3\mathcal{G}(Y_0)^{2/3}} \int_{Y_\mathrm{d}}^{Y_0} \frac{C'(Y)}{\mathcal{G}(Y)^{1/3}}\,\mathrm{d}Y, \tag{5.49a}$$

$$\widetilde{k}_\mathrm{d}^2 = \frac{2}{3\mathcal{G}(Y_\mathrm{d})^{2/3}} \int_{Y_\mathrm{d}}^{Y_0} \frac{C'(Y)}{\mathcal{G}(Y)^{1/3}}\,\mathrm{d}Y, \tag{5.49b}$$

and the corresponding speeds

$$s_\mathrm{d} = \left.\frac{\partial\omega}{\partial k}\right|_{Y_0,\ k_\mathrm{d}}, \qquad \widetilde{s}_\mathrm{d} = \frac{\widetilde{\omega}(Y_\mathrm{d}, \widetilde{k}_\mathrm{d})}{\widetilde{k}_\mathrm{d}}. \tag{5.50}$$

The downstream DSW is again one of elevation, with the linear waves on the left. If $\widetilde{s}_\mathrm{d} > 0$, the downstream DSW remains attached to the topographic perturbation and waves are continuously generated at the downstream edge of the forcing region.

Figure 5.9 shows a representative example of each type of simple-wave transition (attached downstream DSW, attached upstream DSW, both DSWs detached). The boundaries that divide (Δ, F)-space are plotted as dash-dotted curves in (a), which shows that over most of the parameter space both DSWs are detached from the topographic feature as in (c). If F is sufficiently large the upstream DSW can remain attached to the

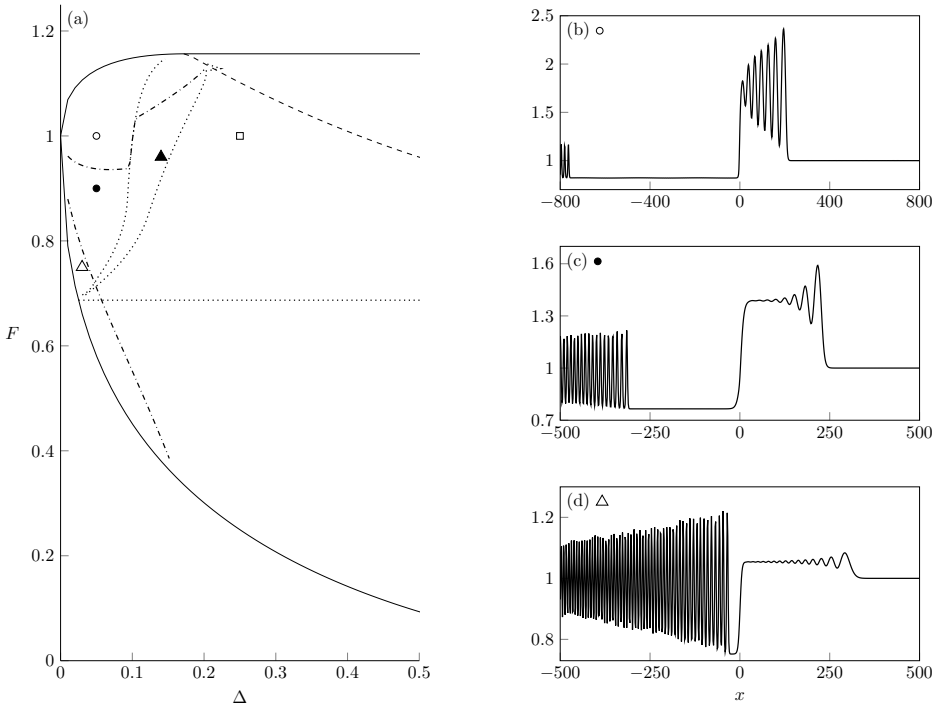

Figure 5.9: As in figure 5.6, but for the dispersive equation and with $Y_0 = 1$. The upper and lower dash-dotted curves in (a) mark the boundaries where the upstream and downstream DSWs, respectively, detach from the topography. Dotted curves mark where the upstream transition changes type, from DSW$^+$ to DSW$^-$|K (left-most dotted curve) and then to R|K (right-most dotted curve – see figure 5.8). Examples of attached and detached DSWs are shown in (b)-(d). Symbols correspond to the location of the solution in (Δ, F)-space, and full details are given in table 5.2.

topography as the background current is too strong to allow it to propagate away. An example of this is shown in (b). There is only a small region of parameter space where the downstream DSW remains attached to the topographic feature and in all cases the downstream wave-train spreads much faster than the upstream one, reflecting the fact that the background current and vortex squashing effects reinforce each other in the downstream controlled state. An example of a solution with an attached downstream DSW is shown in (d).

5.4 Comparison with numerical results

5.4.1 The dispersive long-wave equation

Figures 5.10-5.11 compare theoretical predictions for kink and solitary wave speed and amplitude with values extracted from numerical integrations of the dispersive long-wave equation. Due to the difficulties in resolving the

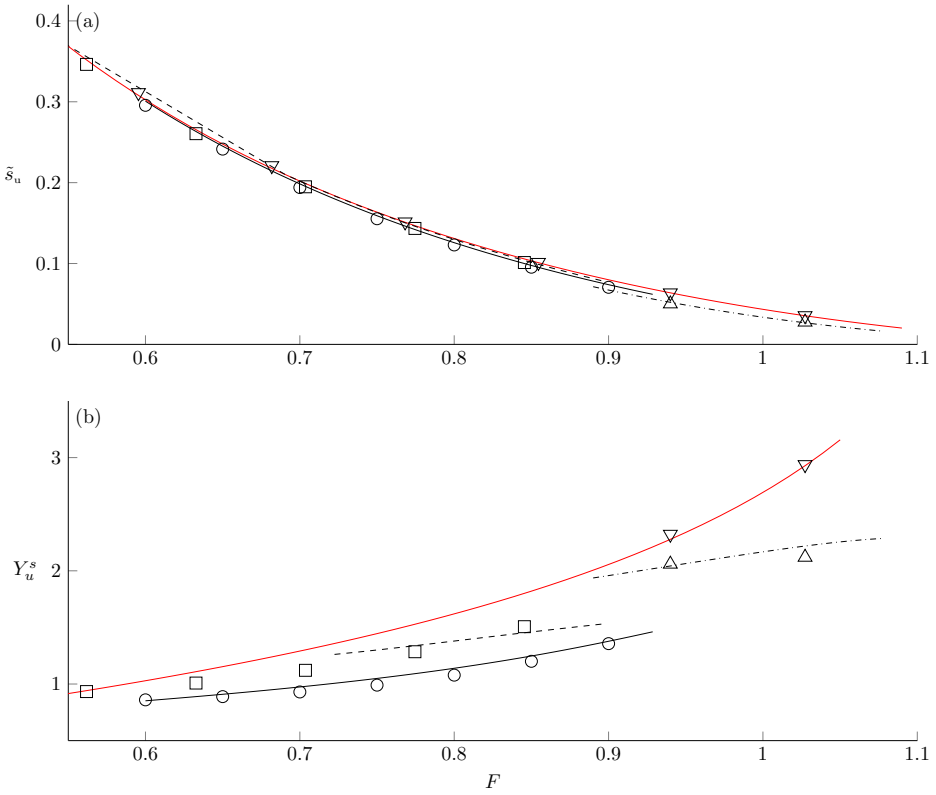

Figure 5.10: Solitary wave parameters in the upstream DSW, with $Y_0 = 0.8$ and $\epsilon = 0.2$. Black curves show the analytical predictions for (a) the speed of the leading solitary wave and (b) the value of Y at the peak of the wave. Curves and symbols are as in figure 5.5, with red curves and inverted triangles ($\triangledown$) showing the speed and amplitude of the kink soliton.

linear end of the DSW in numerical simulations, and thus of systematically identifying that end of the wave-train, no attempt was made to validate El's technique for the linear wavenumber and group velocity. In all of the data presented here $Y_0 = 0.8$ and $\epsilon = 0.2$, while F was varied across the full critical range for each Δ to validate the theory for all types of transition.

Figure 5.10 shows the key parameters of the leading solitary wave in the upstream transition. The speed and amplitude are shown in (a) and (b) respectively, and agreement between theory and numerics is in general very good. The upstream solitary wave speed depends only weakly on Δ, and for all Δ larger values of F correspond to slower, larger-amplitude solitons. The red curve in (a) shows the kink speed s_{K}, which is an upper bound on the solitary wave speed. For $\Delta = 0.1$ (dashed curve) and $F < 0.7$, El's technique predicts an invalid solution with $\widetilde{s}_{\mathrm{u}} > s_{\mathrm{K}}$ and thus amplitude predictions are only shown for $F > 0.7$. For $\Delta = 0.25$ (dash-dotted curve) all of the upstream transitions considered here are resolved by compound-wave solutions. The inverted triangles ($\triangledown$) in (a) show the kink speed, while

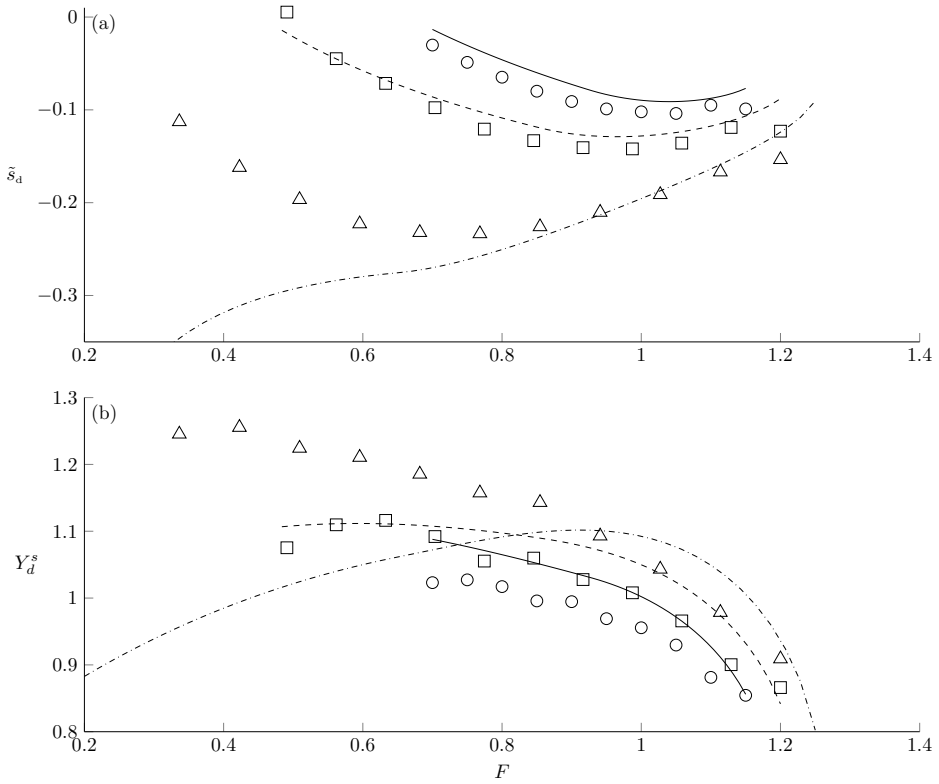

Figure 5.11: As in figure 5.10, but for the downstream solitary wave.

those in (b) show the kink amplitude for transitions which are resolved by a DSW$^-$|K. No attempt was made to systematically identify Y_K in transitions resolved by a R|K (those with $F < 0.9$).

Figure 5.11 shows (a) the speed and (b) the amplitude of the leading soliton in the downstream transition. For $\Delta = 0.05$ and 0.1 (solid curve and circles, dashed curve and squares respectively) agreement between theory and numerics is reasonable. Dispersive shock-fitting describes the DSW in the limit $t \to \infty$, and at the time when integration was stopped the amplitude of the downstream solitary wave was increasing slowly. It is expected that longer integrations would reduce the error in (b) in cases where the amplitude is less than the predicted value. However in some cases the amplitude is greater than the predicted value, and indeed the numerical results for $\Delta = 0.25$ (dash-dot curve and triangles) are qualitatively different from the theory. This may be due to the apparent minima in $\widetilde{s}_{\rm d}$ at $F = F_{\rm cr}(\Delta)$ seen in both the theory and numerics in (a). El et al. [2006] analyse the modulation equations for the Su-Gardner system and show that a minimum in s as a function of the initial jump amplitude in the Riemann problem corresponds to linear degeneracy in the Whitham system. Numerical simulations show that the DSW terminates at the point

of degeneracy, and the linear end is replaced by a finite-amplitude wavefront (their figure 7). As the initial jump amplitude increases beyond the critical value (which corresponds to $F < F_{\rm cr}$ in figure 5.11(a)) the terminal point of the DSW moves closer to the solitary-wave end. The parameters (5.47)-(5.50) are derived assuming that the DSW is fully formed, and thus El's technique cannot formally be applied when $F < F_{\rm cr}$.

5.4.2 Quasi-geostrophic equations

Figure 5.12 compares CD simulations of the full QG problem with predictions from the dispersive long-wave model for critically-controlled flow. Red dashed curves show the dispersive controlled solution computed as in §5.3.1, which agrees excellently with the solution to the full problem over the forcing region. The horizontal dotted line in (a) is the amplitude prediction for the upstream leading solitary wave, and is greater than the maximum amplitude obtained in the CD simulation. In fact in the CD simulation the amplitude of the leading wave reaches a maximum value around $t = 200$ and then decreases slowly from there, suggesting that higher-order dispersion smooths the upstream transition and reduces the amplitude of the solitary wave. The maximum peak observed in the CD simulation is 1.089, while dispersive shock-fitting predicts an amplitude of 1.099. Thus the discrepancies are small enough that dispersive shock-fitting may be used to estimate the speed of the leading solitary wave—the analytical prediction is $\widetilde{s}_{\rm u} = 0.128$ while the average speed of the leading peak over $200 < t < 900$ in the CD simulation is 0.120. For the parameters used in (a) $\widetilde{s}_{\rm d} > 0$ so that the downstream DSW is attached to the topography, and indeed the CD simulation shows that a modulated wave-train develops on the downstream side of the forcing region but does not propagate away. Long-wave theory may be used to predict the size of the largest wave: the stationary solitary wave on the background $Y_\infty = Y_{\rm d}$ has its crest at $Y_{\rm d}^s = 1.25$, while at $t = 900$ in the CD integrations the crest of the largest wave is at $Y = 1.26$.

In (b), both DSWs are detached from the topography. However for this set of parameters $F < F_{\rm cr}$ so that the downstream DSW is partially degenerate and its properties cannot be predicted using dispersive shock-fitting. Indeed, the amplitude of the leading wave in the downstream DSW is greater than the prediction obtained using El's technique (bottom horizontal dotted line). The theory again appears to underpredict the amplitude of the leading wave upstream (upper dotted line), although in this case the amplitude was still increasing when the integration was halted

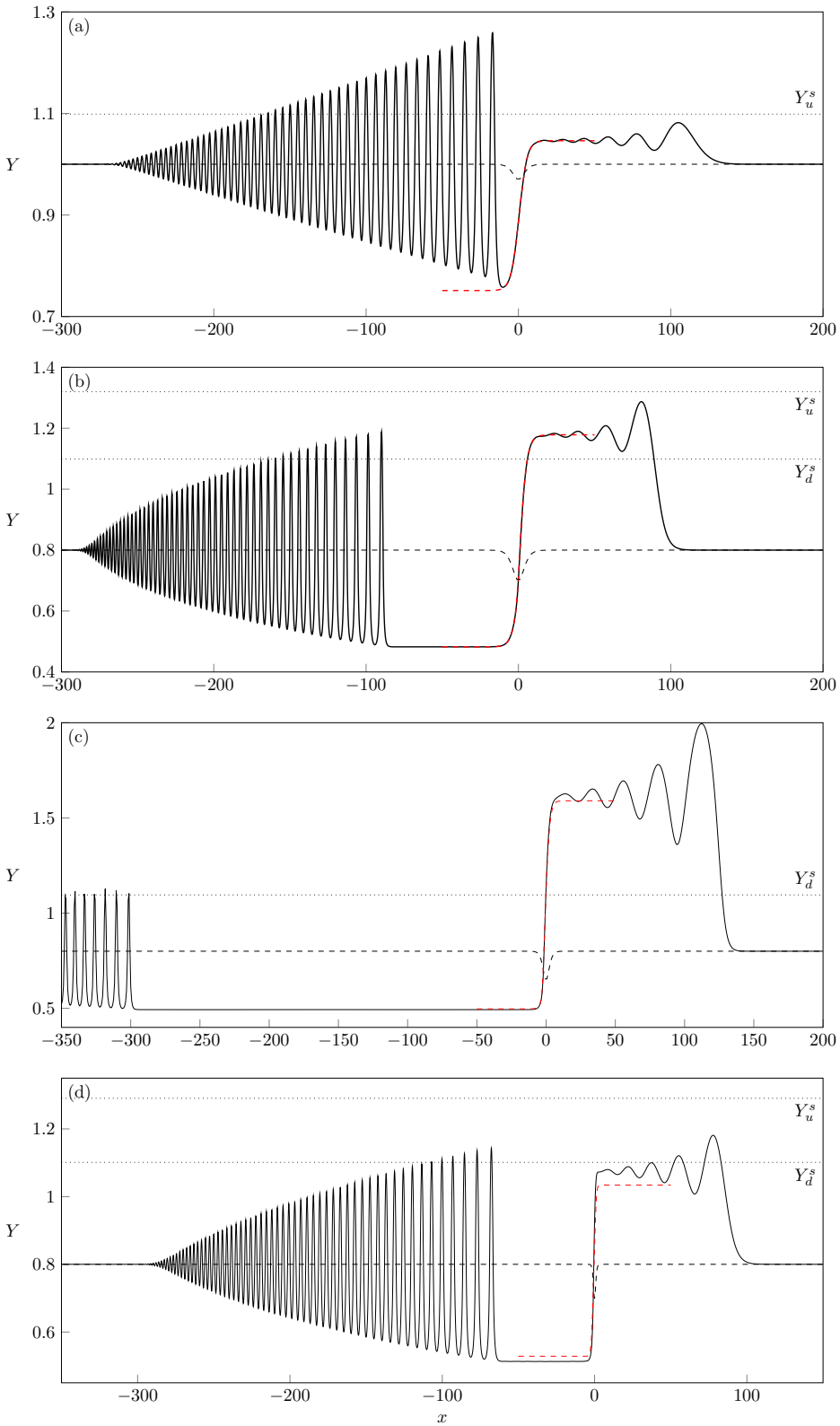

Figure 5.12: Contour dynamic simulations showing critically-controlled flow in the full QG problem. In (a), the downstream DSW is attached to the topography, in (c) the upstream DSW is attached, and in (b) and (d) both DSWs are detached. Red dashed curves show the dispersive controlled solution, black dashed curves show the topography, and black dotted lines show the solitary-wave amplitude predictions from dispersive shock-fitting. Full details are given in table 5.3.

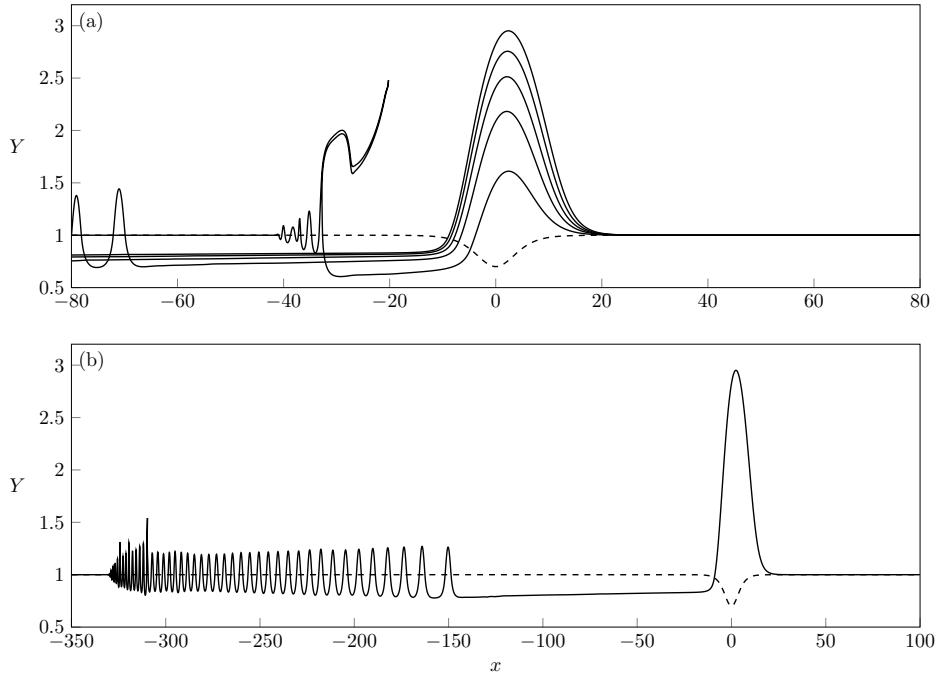

Figure 5.13: Contour dynamic simulation in the offshore plume regime. (a) Snapshots of the solution in the source region, every 200 time units starting from $t = 100$. (b) The solution at $t = 900$. Full details are given in table 5.3.

at $t = 1000$. The analytical prediction for the speed is $\widetilde{s}_{\mathrm{u}} = 0.129$ while in the CD simulation $s = 0.127$ when averaged over $750 < t < 1000$. In (c), the upstream DSW is attached to the topography. Here, $F > F_{\mathrm{cr}}$ and the dispersive long-wave theory accurately predicts the amplitude of the solitary wave that leads the downstream DSW.

Figure 5.12(d) shows a simulation with $\epsilon = 1$ and thus is a check on the validity of the long-wave theory. At this extreme value of ϵ the dispersive long-wave theory does not accurately predict the adjusted values $Y_{\mathrm{u/d}}$, but the difference is still less than 5%. In fact the contour dynamic simulation lies between the hydraulic and dispersive long-wave predictions in the source region, which suggests that the departure from hydraulic theory is not a monotonic function of ϵ. However the qualitative behaviour is much the same, with a monotonic steady solution across the source region and dispersive wave-trains up- and downstream. The difference between the dispersive controlled solution and that selected by the CD simulation is greater upstream, and correspondingly the prediction for Y_{u}^{s} is better than that for Y_{d}^{s}. Further CD simulations (not shown) suggest that the dispersive long-wave theory provides an accurate quantitative description of the QG system up to $\epsilon \approx 0.5$.

Figure 5.13 shows a contour dynamic simulation in the offshore plume

Subplot	Type	F	Y_0	Δ	a	ϵ	t
5.12(a)	Downstream attached	0.75	1	0.03	1.07	0.2	900
5.12(b)	Both detached	0.8	0.8	0.1	1.19	0.2	700
5.12(c)	Upstream attached	0.92	0.8	0.15	1.11	0.33	1900
5.12(d)	Both detached	0.8	0.7	0.1	1.2	1	700
5.13(b)	Offshore plume	1.1	1	0.3	0.88	0.2	900

Table 5.3: Details of the initial value problems displayed in figures 5.12 and 5.13.

regime, where neither the controlled nor the supercritical solution exist and the shelf water is directed offshore. The growing behaviour is highlighted in (a), which shows snapshots of the solution in the source region, taken every 200 time units starting from $t = 100$. Since the flow is unsteady the downstream state Y_d is not well-defined and the modulated wavetrain that forms in the transition to far-field flow is irregular. A filament is ejected at early times, and the wavetrain is not ordered by amplitude, as seen in (b) where the full solution is shown at $t = 900$.

5.5 Discussion

A fully-nonlinear, dispersive long-wave model has been used to study hydraulic control of barotropic topographic Rossby waves. This model therefore complements previous works by Gill [1977] and Dale and Barth [2001] by exploring control by coastal-trapped waves in the limit of small S, and extends the rigid-lid channel-flow model of Haynes et al. [1993] to a coastal setup. Section 5.2 classifies the behaviour of the hydraulic (non-dispersive long-wave) equation and derives conditions for critical control in terms of Y_0, the far-field width of the shelfbreak; Δ, the maximum magnitude of the shelfbreak perturbation; and the Froude number F, which is a function of Y_0, the strength of the background flow, and the depth of the shelf. The downstream transition between the controlled state and the far-field flow is always resolved by a shock, while the upstream transition may be resolved by a shock, a rarefaction, or a compound-wave shock-rarefaction. Figure 5.6 gives an example of each type of resolution, and shows how the (Δ, F)-plane is divided when $Y_0 = 0.8$. In §5.3.2 we use dispersive shock-fitting to analyse the dispersive long-wave equation, and show that shocks are replaced by modulated wave-trains which remain attached to the topography when F is near the boundary for critical flow. Figure 5.10 shows that the theory accurately describes upstream DSWs, whereas figure 5.11 shows that the downstream solitary wave speed can

have a turning point when plotted as a function of F. In this case the downstream wave-train is not a fully-developed DSW, and the assumptions required for dispersive shock-fitting to be applicable do not hold. Figure 5.12 confirms that this behaviour also occurs in the full QG system, and that the dispersive long-wave theory accurately predicts the solution in the forcing region and upstream at large times.

The present model is too simple to make quantitative comparisons with real CSWs. A sloping shelf and a more realistic background current can be incorporated following the discussion of §5.1, while other factors such as stratification, external forcing and dissipation will of course also be important in the real ocean. However, some of the qualitative features that are noted here merit further investigation. First and most important is to understand the regimes in which CTWs exert hydraulic control in the real ocean. Zhang and Lentz [2017] and Saldías and Allen [2020] both present numerical simulations of CTWs in a configuration very similar to that used here, albeit with sloping topography and a background flow driven by (constant) wind forcing. While Zhang and Lentz [2017] report steady flow when the background current opposes CTW propagation, and a response consistent with an arrested CTW, Saldías and Allen [2020] find that their simulations never become steady in the forcing region and instead develop a meandering wave-train upstream. The reason for this difference is not clear, although Saldías and Allen [2020] estimate that the Froude number for the first three CTW modes in their model is 2, 0.2 and 0.1 respectively so that they may be outside the range in which hydraulic control occurs.

Another interesting question concerns the formation of attached and detached DSWs. Figure 1.3 shows that the downstream DSW in Zhang and Lentz [2017] remains attached to the topography, while the present model suggests that this only occurs when the flow is very close to the subcritical boundary. Attached DSWs continually generate waves at one edge of the forcing region, and thus would be easier to identify and analyse in more complex models than detached DSWs, which may quickly degrade due to diabatic effects. Finally, in the present model some solutions on very wide shelves ($Y_0/L_\mathrm{R} > \log(2)$) never become steady and instead develop ever-growing offshore plumes (§5.2.2 and figure 5.13). While it is true that a sudden decrease in shelf width can induce the separation of a Western Boundary Current (as happens to the Gulf Stream at Cape Hatteras [Tansley and Marshall, 2000]), the situation is more complicated than in the present model. In a flat-bottomed ocean columns of fluid that cross the shelfbreak can continue to move offshore easily, whereas in an ocean with a sloping bottom the proclivity of depth-integrated flow to

follow isobaths limits exchange between the shelf and open ocean. Columns of fluid must instead separate from the bottom as they cross the shelfbreak, and thus the dynamics differ from the barotropic model employed here.

Chapter 6

Conclusions and future work

This thesis presents idealised models of three coastal flows. The focus is on understanding how vortex effects (image vorticity and Rossby waves driven by a jump in PV) interact with a background coastal-intensified current. In all cases theoretical predictions have been verified using numerical simulations In particular, we employ contour dynamics in chapters 3-5 to test the validity of the long-wave approximation which is required for the analysis.

In chapter 2 we use a long-wave, $1\frac{1}{2}$-layer shallow-water model to study the behaviour of river plumes. As in the QG model introduced by Johnson et al. [2017], the qualitative behaviour of the plume depends critically on whether columns of fluid stretch or squash as they emerge from the river mouth, and the relative strengths of the vorticity-driven dynamics to the alongshore flow set up by the internal Kelvin wave. We derive a complete theory for outflows with positive PVa by matching steady solutions in the source region with similarity solutions downstream, and show that at all times the outflow plume is led by a finite-amplitude Kelvin wave which sets the coastal boundary condition for the plume behind. This justifies the use of such a boundary condition in the quasi-geostrophic models employed in later chapters, where the Kelvin wave propagates at infinite speed. When the outflow has negative PVa, the resulting plume is bidirectional and may either grow indefinitely, become steady in the source region, or attempt to separate from the coast. Chapter 3 extends the QG model to include outflows with non-uniform (but still piecewise-constant) PV, and shows that the sign and distribution of source vorticity can be used to

understand the behaviour of the plume. When the integral of vorticity across competitive regions of the source is positive, all of the expelled fluid turns to the right and the outflow operates in coastal current mode. If the net contribution of source vorticity is zero—as is often assumed to be the case in laboratory and numerical experiments—a quasi-steady anticyclonic gyre may form downstream of the source mouth.

Chapter 4 looks at the behaviour of long, dispersive waves on a PV front, and how those waves are influenced by the presence of a coastal boundary. At leading order, propagation of long waves is entirely driven by coastal effects (image vorticity and the background current), and the richest dynamics are found in the regime where vortical effects are dominant. We explore the range of behaviours for the front using the canonical example of the Riemann problem, which in the dispersive equation is analysed by considering the corresponding potential function and using the method of dispersive shock-fitting. The flux function for this problem is non-convex when vortical effects are sufficiently strong, so that in some cases the initial step is resolved by a compound-wave structure (a combination of a kink soliton and a rarefaction or dispersive shock-wave). Contour dynamic simulations show that the dispersive long-wave theory provides quantitative predictions for the long-time behaviour of the full QG system, even though the initial condition involves a rapid transition.

In chapter 5 the coastal-front model is extended to include a flat continental shelf of variable width. The PV front is initially aligned with the shelfbreak and is displaced by a coastal-intensified background current. When the background current opposes the direction of coastal-trapped wave propagation and the shelfbreak perturbation is a local decrease in width, the flow can become critically controlled. We derive the conditions for critical control, and show how the transition between controlled and far-field flow depends on the Froude number and magnitude of the shelfbreak perturbation. The upstream transition can be resolved by a compound-wave structure, while the downstream transition is always resolved by a shock. When first-order dispersive effects are included in the model these shocks are replaced by DSWs, which remain attached to the perturbation when the incoming flow is close to the boundary between critical and non-critical.

We will now discuss the limitations of the models used in this thesis, as well as some ideas for future work.

6.1 The vorticity dynamics of coastal outflows

The idealised model employed here seeks to explain how vorticity dynamics affect plume behaviour, rather than provide quantitative predictions of plume properties (although see figure 2.15). It is important to consider how factors omitted by the model may affect the results, and how the model can be used by researchers wishing to conduct further investigation.

The most obvious difference between the present work and other outflow models is that here the expelled fluid has the same density as the upper ocean layer. Outcropping of density surfaces is prohibited in the QG limit, and the semi-geostrophic model is singular when $H = 0$ so that the initial-value problem with no outer layer is ill-posed. A similar situation occurs in the rotating dam break problem when the channel in front of the dam is initially dry. This is resolved by Helfrich et al. [1999], who find that analytic results can be obtained by smoothing the transition region so that the depth of the fluid is continuous. The presence of a finite-depth outer layer in the model used here means that the effects of buoyancy gradients and mixing are ignored. While these surely contribute to plume behaviour, in the limit of weak horizontal stratification vorticity and Kelvin-wave dynamics may be dominant. This could be tested in numerical simulations or a laboratory setting by adjusting the density contrast $\Delta\rho$ between the expelled and ocean fluid. When there is no buoyancy gradient ($\Delta\rho = 0$) the present model should accurately describe the behaviour of the outflow plume. It would be interesting to see at what value of $\Delta\rho$ qualitative differences emerge, and whether any real outflows fall into the low-gradient regime where the present model could be applied quantitatively. Another major difference between our results and those of most other studies is that bulges are comparatively rare here. These two differences may be related: Yankovsky [2000] presents numerical results which suggest that bulges are an effect of finite $\Delta\rho$ (their figures 2 and 3), and we show in §3 that when the outer layer is shallow the plume tries to separate from the coast upstream of the source, which could indicate that the model is attempting to form a round bulge typical of numerical plumes.

One possible extension to the present model would be to allow exchange between the expelled and ocean fluid at the plume boundary. Garvine [1981] parameterises this cross-front mixing in a shallow-water model by taking a long-wave limit in which the mass and momentum balance in the (finite-width) frontal region are replaced by jump conditions across a density interface. Mixing (or any other dissipative process) homogenises PV, and thus, in the real oceans, the Rossby-wave component of the dynamics

would decrease over time as the PV jump decays so that the flow becomes Kelvin wave-dominated at late times. A background current, tides, or a variable-strength outflow can be incorporated into the semi-geostrophic model following Southwick et al. [2017] and are likely to affect plume behaviour in a similar way as for the QG model discussed there. Piecewise-constant topography can be included in the QG model (as in §5) and is likely to enhance downstream propagation of the plume through additional vortex stretching (see An and McDonald [2004] and the discussion of §3.5).

We hope that the discussion of vortical effects presented here is also relevant for the more general problem of the separation of a coastal current, for example in flow through a sea strait or around a cape, in which buoyancy gradients are likely to be of secondary importance. Whitehead and Miller [1979] and Bormans and Garrett [1989] discuss flow through the Strait of Gibraltar, where a surface current of Atlantic water flows eastward through the strait and separates from the coast to form an anticyclonic gyre in the Alboran sea. Bormans and Garrett [1989] suggest that the flow turns through an inertial circle, and thus separates when the inertial radius U/f is greater than the radius of curvature at the corner of the strait. A similar inertial theory is developed for bulge formation in the outflow context by Avicola and Huq [2003b]. As discussed in §3.5, in the QG limit advective terms are omitted and thus the inertial radius is assumed to be small. The results of that chapter, where the current turns at a right angle and remains attached to the coast provided the cyclonic component of vorticity is dominant, are therefore consistent with the inertial approach. Advective terms are included in the semi-geostrophic model, but separation is implicitly forbidden by the particular formulation of the governing hyperbolic system. Klinger [1994] studies steady flow around a curved coastline in the semi-geostrophic limit, and shows that r_c, the maximum radius of curvature for which the flow separates from the coast, depends on the upstream properties of the current. Klinger finds that r_c is proportional to U/f, but the relationship is sensitive to the definition of the velocity scale U. One way to clarify the above results would be to perform a detailed numerical study of the full shallow-water equations, where the Rossby number is varied systematically in order to control the relative contributions of vortical effects and advection.

6.2 Coastal potential-vorticity fronts

There are a number of interesting questions that could be addressed within the modelling framework used here. One could study coastal fronts in

the shallow-water equations, and compare the linear dispersion relation with the expression for a free front, which was derived in Nycander et al. [1993] and Cushman-Roisin et al. [1993]. The phase speed would still have the (quadratic) dependence on k given by (4.38), and presumably any additional terms in the coefficients would decay off-shore like some power of $\exp(-y/L_{\mathrm{R}})$. This would allow for the study of waves on a density front by taking the limit $h_1 \to 0$, and β-plane dynamics could also be incorporated. The purpose of doing this would be to identify the parameter regimes in which different mechanisms are dominant, and thus understand what drives the meandering behaviour of PV fronts in the real oceans. As discussed in §4.5 finite-amplitude meanders on a PV front such as the Gulf Stream may be better modelled as solitary waves. The shallow-water soliton phase speed can easily be computed from ω, and it would be interesting to compare these predictions with observations of, for example, Kuroshio Extension meanders [Tracey et al., 2012]. Thin-jet theory has recently been shown to be a useful way of understanding the variability of the Kuroshio Extension and the Gulf Stream [Sasaki and Schneider, 2011a,b] and it is possible that other currents could be described using the coastal version presented here.

However it is likely that time-dependent analysis of coastal fronts in the shallow water equations would be restricted to finding the dispersion relation. The path equation for a shallow-water free front is formulated in an intrinsic co-ordinate system (along-jet and cross-jet), and although Cushman-Roisin et al. [1997] have derived a steady model for thin barotropic jets over small bottom topography, it seems that the assumption of steady flow is necessary to make analytical progress in the presence of a fixed boundary. Casting the equations in the intrinsic co-ordinate system also allows one to study certain multi-valued solutions (breathers, or envelope solitons) analytically [Ralph and Pratt, 1994] although it should be noted that some of these structures violate the thin-jet assumption. Persistent multi-valued solutions were not observed in any of the contour dynamic simulations conducted in §4, but may well occur in other initial-value problems. Again it would be interesting to unify the free-front and coastal models and identify why breathers appear not to occur in the coastal regime.

The present model does not include buoyancy gradients or eddy diffusion. While the former may be of secondary importance in certain boundary currents, including eddies would qualitatively change the dynamics. In fact the original study of Pratt and Stern [1986] aimed to investigate whether vortical effects alone could lead to eddy pinch-off. The analytical results of Ralph and Pratt [1994], and the contour-dynamic simulations conducted

here, suggest that such a situation rarely occurs and instead eddy pinch-off is a purely diffusive process, which therefore alters the PV of the jet and limits the applicability of the present model. Diabatic processes are also likely to prevent the fine structure of DSWs from being realised in the real oceans, as PV would certainly not be conserved over the timescales required for a DSW to form. However it would be interesting to perform similar numerical experiments to those of §4 and Pratt and Stern [1986] in an eddy-resolving model, to see whether there is a length- or time-scale over which purely dispersive effects can be observed. In parameter regimes where dispersion acts over shorter timescales than diffusion, vorticity dynamics could be used to model the initial folding of a front, before diffusive eddy pinch-off takes over.

Finally, it is not clear why El's technique breaks down for certain initial steps (the shaded areas in figure 4.11). Those in the upper-right quadrants are of particular interest; the initial step does not straddle the inflexion point and numerical simulations show that it is resolved by a modulated wave-train. Of the conditions that must be satisfied for El's technique to apply, the one that is least certain is hyperbolicity. Why this should fail along the particular curve marked in figure 4.11 is not clear. It would be helpful to find a simpler equation in which the same breakdown occurs, and for which the Whitham system could be studied directly, to identify the cause of the breakdown and the properties of the structure that resolves the initial-value problem in the shaded region.

6.3 Hydraulic control of continental shelf waves

As discussed in §5.5, it is not clear whether hydraulic control by coastal-trapped waves is a common phenomenon in the real oceans. The results of Zhang and Lentz [2017] are encouraging: the Hövmoller diagram reproduced in figure 1.3 shows that information propagates away from the valley in both directions, and that this only occurs when the background flow opposes CTW propagation. Further, figure 14 of Zhang and Lentz [2017] shows that cross-shelf profiles of the SSH, bottom pressure and alongshore velocity from their numerical simulations all agree well with shapes predicted by a linear CTW model. Zhang and Lentz performed several numerical simulations where the strength of the wind forcing was varied systematically, but it seems that in all of these they observed control by the same mode. By contrast, Saldías and Allen [2020] did not observe controlled flow in any of their numerical simulations. By exploring a wider range of flow speeds in a numerical model, one could potentially identify

the boundaries for critical flow, as well as boundaries at which control changes between different modes. An improved understanding of hydraulic control could lead to a better parameterisation of boundary currents in global ocean models. The controlled flows in §5 decrease the transport of the background flow by recirculating some of the shelf water. This suggests that the parameterisation of such currents may need to account for large variations in shelf width that could significantly alter their structure and transport.

Perhaps the most restrictive assumption of the present model is that, in common with most theoretical studies of hydraulic control, it eliminates all but one mode. The extension of control theory to continuous PV and several modes would be a very important result, although Hughes [1985] shows that analytically identifying the controlling mode for a given geometry is likely to be difficult. One possibility is to follow Mitsudera and Grimshaw [1990] and Zhang and Lentz [2017] and identify the controlling mode as that with the phase speed which is nearest to the (negative of the) background flow velocity. This suggests that control may in fact be more common in models with several modes, as there is a wider range of phase speeds that can become arrested. Grimshaw [1987] shows that the controlling mode is resonant, and thus if that mode has a non-zero coefficient initially it will grow to dominate the response at later times. However, in general mode-mode interactions may limit growth of resonant terms at higher modes, and thus control is likely to be restricted to the first few modes. Indeed, mode-1 resonant CSWs (defined as having small group velocity) have been observed off the coasts of Scotland [Gordon and Huthnance, 1987] and Antarctica [Wåhlin et al., 2016].

The agreement between the dispersive long-wave theory and numerical simulations is not as good as for the coastal front model. In particular, the theoretical prediction for the downstream solitary wave amplitude can have a qualitatively different dependence on F as that observed in the numerical results (figure 5.11(a), dash-dotted curves and triangles). We have suggested that this is due to a turning point in the observed solitary wave speed, but a more detailed investigation of the equation is needed to confirm this. The numerical results appear to show a DSW forming downstream, but it is not clear what the equivalent for a finite-amplitude wave-front is for a DSW that is degenerate at the solitary wave end, or indeed whether the minimum in $\widetilde{s}$ does correspond to degeneracy of the Whitham system. Finding an equation that displays this behaviour and has an integrable structure could lead to further developments in the theory of dispersive shock waves.

Appendix A

Riemann invariants of the semi-geostrophic model

A.1 Expressions for λ and $\alpha_{\mathbf{C/R}}$

The governing equations (2.15) and (2.16) are diagonalised and hence recast in the form

$$\frac{\partial}{\partial t}\begin{pmatrix} U \\ w \end{pmatrix} + \frac{1}{a+b}\begin{pmatrix} c+b\left(U+\sqrt{H}\right) & d \\ c-a\left(U+\sqrt{H}\right) & d \end{pmatrix}\frac{\partial}{\partial x}\begin{pmatrix} U \\ w \end{pmatrix} = \frac{Q'(x)}{a+b}\begin{pmatrix} 1 \\ 1 \end{pmatrix} \tag{A.1}$$

where

$$\begin{aligned}
a &= -1 + H + \cosh w + \sqrt{H}\sinh w, \\
b &= (H-1)\left(-1+\cosh w\right) + \left(\sqrt{H}\cosh w + \sinh w\right)U, \\
c &= \left(\sqrt{H}\cosh w + \sinh w\right)\left(1 + U\sinh w + \cosh w\left(-1+H+\sqrt{H}U\right)\right), \\
d &= \left((H-1)\sinh w + U\left(\cosh w + \sqrt{H}\sinh w\right)\right) \\
&\quad \times \left(1 + U\sinh w + \cosh w\left(-1+H+\sqrt{H}U\right)\right),
\end{aligned}$$

which leads to the eigenvalues

$$\begin{aligned}
\lambda_{\pm} = \frac{1}{2(a+b)}\Big(&c + d + b(U+\sqrt{H}) \\
&\pm\sqrt{(-4d(a+b)(U+\sqrt{H}) + (c+d+b(U+\sqrt{H}))^2)}\Big).
\end{aligned} \tag{A.2}$$

Outside of the source region, the right side of (A.1) is homogenous and so there exist left eigenvectors $\mathbf{k}_\pm$ such that

$$\mathbf{k}_\pm^T \left(\frac{\partial}{\partial t} \begin{pmatrix} U \\ w \end{pmatrix} + \lambda_\pm \frac{\partial}{\partial x} \begin{pmatrix} U \\ w \end{pmatrix} \right) = 0, \tag{A.3}$$

or,

$$k_{\pm,1} \frac{\mathrm{d}U}{\mathrm{d}t} + k_{\pm,2} \frac{\mathrm{d}w}{\mathrm{d}t} = 0 \qquad \text{on } \frac{\mathrm{d}x}{\mathrm{d}t} = \lambda_\pm, \tag{A.4}$$

or

$$\frac{\mathrm{d}U}{\mathrm{d}w} = -\frac{k_{\pm,2}}{k_{\pm,1}} \qquad \text{on } \frac{\mathrm{d}x}{\mathrm{d}t} = \lambda_\pm. \tag{A.5}$$

These are the ODEs that determine the Riemann invariants as described in (2.34). The eigenvectors $\mathbf{k}$ can always be chosen so that $k_{\pm,2} = 1$, in which case

$$\frac{\mathrm{d}U}{\mathrm{d}w} = -\frac{d}{\lambda_\pm(a+b)} \left(\frac{\mu_\pm + d}{\mu_\pm - d} \right) = \alpha_{\mathrm{C/R}},$$

$$\mu_\pm = c + b(U + \sqrt{H}) \tag{A.6}$$

$$\pm \sqrt{(-4d(a+b)(U+\sqrt{H}) + (c+d+b(U+\sqrt{H}))^2)} \tag{A.7}$$

A.2 Values of λ in various limits

Note that

$$a + b = (\sqrt{H} \cosh w + \sinh w)(\sqrt{H} + U) \tag{A.8}$$

which is positive, subject to the observation that w and U are non-negative in all solutions here. Thus, from (A.2), we can define $\lambda_\mathrm{C} = \lambda_+$ and $\lambda_\mathrm{R} = \lambda_-$ with $\lambda_\mathrm{C} \geq \lambda_\mathrm{R}$ always, and from now on it is only necessary to consider the numerator when checking the sign of $\lambda_{\mathrm{C/R}}$.

Further, taking $w = 0$ gives the following:

$$[a, b, c, d] = [H, \sqrt{H}U, H(U + \sqrt{H}), \sqrt{H}U(U + \sqrt{H})] \tag{A.9}$$

so that the numerator in (A.2) simplifies to

$$(2U\sqrt{H} + H)(U + \sqrt{H}) \pm H(\sqrt{H} + U) = (2U + \sqrt{H} \pm H)(\sqrt{H} + U),$$

which gives $\lambda_\mathrm{R} = U$ and $\lambda_\mathrm{C} = U + \sqrt{H}$. Thus when additionally $U = 0$, $\lambda_\mathrm{R} = 0$ and $\lambda_\mathrm{C} = \sqrt{H}$.

The repetition of terms in the numerator of $\lambda_{\mathrm{C/R}}$ shows that $\lambda_{\mathrm{C/R}} = 0$ only when

$$-4d(a+b)(U+\sqrt{H}) = 0 \tag{A.10}$$

with $\lambda_{\mathrm{R}} = 0$ if $c + d + b(U + \sqrt{H}) > 0$ and $\lambda_{\mathrm{C}} = 0$ otherwise. Equation (A.10) is satisfied only if $d = 0$, or equivalently if one of

$$(H - 1 + \sqrt{H}U)\sinh w + U\cosh w = 0,$$
$$(H - 1 + \sqrt{H}U)\cosh w + U\sinh w = -1,$$

holds. But, from (2.9) and (2.11) this requires that either $u_{\mathrm{w}} = 0$ or $h_{\mathrm{w}} = 0$. The latter is forbidden in the model used here, and setting $u_{\mathrm{w}} = 0$ gives

$$c + d + b(U + \sqrt{H}) = (\sqrt{H}\cosh w + \sinh w)(U + \sqrt{H})^2$$

which is always positive. Hence λ_{C} is never zero, and since λ_{C} is positive when $t = 0$ it must remain so for $t > 0$. Further, $\lambda_{\mathrm{R}} = 0$ for $t > 0$ is equivalent to $u_{\mathrm{w}} = 0$, a constraint which is physical only if $H < 1$. Thus, λ_{R} cannot change sign in outflows with positive PVa. Expanding for small w and U gives

$$\lambda_{\mathrm{R}} \sim U + (H - 1)w \quad \text{as } U \to 0, w \to 0 \tag{A.11}$$

so that $\lambda_{\mathrm{R}} > 0$ initially, and hence always, when $H > 1$.

Appendix B

Vortex competition in the semi-geostrophic model

§2 discusses the outflow problem for $O(1)$ Rossby number using a semi-geostrophic (long-wave) model with uniform PV. Here we consider the equivalent set-up for a competitive outflow, and show that the coastal current mode is only possible if the net contribution from the source vorticity is positive.

The governing equations for semi-geostrophic flow are:

$$\begin{aligned} \frac{\partial u}{\partial t} + u\frac{\partial u}{\partial x} + v\frac{\partial u}{\partial y} - v &= -\frac{\partial h}{\partial x}, \\ u &= -\frac{\partial h}{\partial y}, \\ \frac{\partial h}{\partial t} + \frac{\partial}{\partial x}(uh) + \frac{\partial}{\partial y}(vh) &= 0, \end{aligned} \tag{B.1}$$

where, following §2, x has been non-dimensionalised with W, y with L_{R}, u and v with $\sqrt{g'H_S}$ and $\sqrt{g'H_S}(L_{\mathrm{R}}/W)$ respectively, h with H_S and t with $W/\sqrt{g'H_S}$. The long-wave parameter is L_{R}/W and is assumed to be small (note that the long-wave parameter is L_{V}/W in the QG model). The potential vorticity q is piecewise constant, and takes non-dimensional values $1/H$, 1, and q^{R} in the ambient ocean, the HPVF and the LPVF respectively. The presence of an ambient ocean-layer with $H > 1$ is a necessary requirement in this model for the plume to have $\zeta > 0$ at $y = w_2$.

From conservation of PV and continuity of h and u, the layer-depth h is

$$h = \begin{cases} 1 + (H-1)\cosh(y - w_2) & w_1 < y < w_2 \\ \frac{1}{q^{\mathrm{R}}} + A\cosh[\sqrt{q^{\mathrm{R}}}(y-w_1)] + B\sinh[\sqrt{q^{\mathrm{R}}}(y-w_1)] & y < w_1, \end{cases} \tag{B.2}$$

where

$$\begin{aligned} A =& \frac{q^{\mathrm{R}} - 1}{q^{\mathrm{R}}} + (H-1)\cosh(w_1 - w_2), \\ B =& (H-1)\sinh(w_1 - w_2)/\sqrt{q^{\mathrm{R}}}. \end{aligned}$$

As in the QG model, the ambient ocean is undisturbed. The interface widths w_1 and w_2 are determined by the flux conditions

$$Q_0 = \int_0^{w_2} uh \ \mathrm{d}y = \frac{h_S^2 - H^2}{2}, \tag{B.3}$$

$$Q_+ = \int_{w_1}^{w_2} uh \ \mathrm{d}y = \frac{h_1^2 - H^2}{2}, \tag{B.4}$$

where Q_0 is the non-dimensional volume flux of the outflow, and h_S and h_1 are the layer-depths at the coast and w_1 respectively. The expressions for w_1 and w_2 are complicated, but can be found computationally using symbolic manipulation. For a given Q_0 and H we test values of Q_+ and q^{R} to numerically determine the region of the parameter space where w_1 is valid and so the coastal current mode is possible. For the particular case of $Q_0 = 1.5$, $H = 2$, the region of the parameter space where a coastal current is possible is shown shaded in figure B.1.

We then compute the source vorticity integral analytically.

$$\begin{aligned} \int_{\text{source}} \zeta_S \ \mathrm{d}Q &= \int_0^{Q_0} qh_S - 1 \ \mathrm{d}Q \\ &= -Q_0 + \int_0^{Q_+} h_S \ \mathrm{d}Q + q^{\mathrm{R}} \int_{Q_+}^{Q_0} h_S \ \mathrm{d}Q \\ &= -Q_0 - \frac{H^3}{3} + \frac{1 - q^{\mathrm{R}}}{3}\left(H^2 + 2Q_+\right)^{3/2} + \frac{q^{\mathrm{R}}}{3}\left(H^2 + 2Q_0\right)^{3/2}, \end{aligned} \tag{B.5}$$

where the last step has made use of (B.3). The region to the right of the dashed line in figure B.1 shows where the net contribution is positive. There is good agreement between these two regions, so again it seems that the coastal current mode can occur if and only if the net contribution of source vorticity is positive.

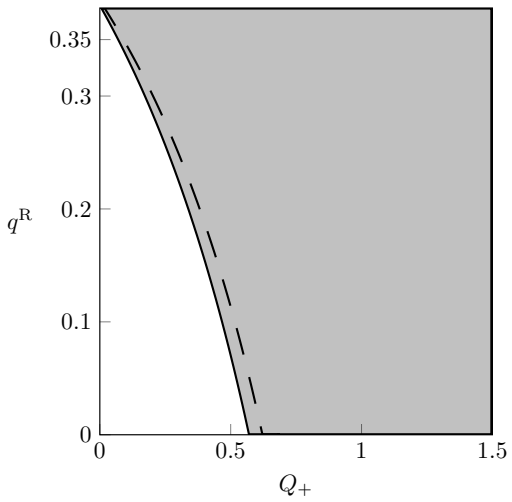

Figure B.1: Numerically computed region of the (Q_+, q^{R}) parameter space for which the coastal current mode exists (shaded grey). The integrated source vorticity is positive to the right of the dashed line. The outflow parameters are $Q_0 = 1.5$ and $H = 2$.

Bibliography

B. W. An and N. R. McDonald. Coastal currents generated by outflow and vorticity and their interaction with topography. *Cont. Shelf Res.*, 24(13-14):1531–1547, 2004.

G. Avicola and P. Huq. The characteristics of the recirculating bulge region in coastal buoyant outflows. *J. Mar. Res.*, 61(4):435–463, 2003a.

G. Avicola and P. Huq. The role of outflow geometry in the formation of the recirculating bulge region in coastal buoyant outflows. *J. Mar. Res.*, 61(4):411–434, 2003b.

R. C. Beardsley, R. Limeburner, H. Yu, and G. A. Cannon. Discharge of the Chang Jiang (Yangtze river) into the East China sea. *Cont. Shelf Res.*, 4(1-2):57–76, 1985.

T. B. Benjamin and M. J. Lighthill. On cnoidal waves and bores. *P. Roy. Soc. Lond. A Mat.*, 224(1159):448–460, 1954.

M. Bormans and C. Garrett. A simple criterion for gyre formation by the surface outflow from a strait, with application to the Alboran Sea. *J. Geophys. Res. – Oceans*, 94(C9):12637–12644, 1989.

K. H. Brink. Coastal-trapped waves and wind-driven currents over the continental shelf. *Annu. Rev. Fluid Mech.*, 23(1):389–412, 1991.

G. A. Cannon. Circulation in the Strait of Juan de Fuca: some recent oceanographic observations. Technical report, Environmental Research Laboratories (US), 1978.

R. J. Chant. Interactions between estuaries and coasts: River plumes – their formation, transport, and dispersal. In E. Wolanski and D. McLusky,

editors, *Treatise on Estuarine and Coastal Science*, pages 213 – 235. Academic Press, Waltham, 2011.

R. J. Chant, S. M. Glenn, E. Hunter, J. Kohut, R. F. Chen, R. W. Houghton, J. Bosch, and O. Schofield. Bulge formation of a buoyant river outflow. *J. Geophys. Res. – Oceans*, 113(C1), 2008.

S.-N. Chen. Enhancement of alongshore freshwater transport in surface-advected river plumes by tides. *J. Phys. Oceanogr.*, 44(11):2951–2971, 2014.

S. R. Clarke and E. R. Johnson. Finite-amplitude topographic Rossby waves in a channel. *Phys. Fluids*, 11(1):107–120, 1999.

T. Congy, G. A. El, M. A. Hoefer, and M. Shearer. Nonlinear Schrödinger equations and the universal description of dispersive shock wave structure. *Stud. Appl. Math.*, 142(3):241–268, 2019.

D. M. Conlon. On the outflow modes of the Tsugaru Warm Current. *La mer*, 20:60–64, 1982.

T. J. Crawford. *An experimental study of the spread of buoyant water into a rotating environment*. PhD thesis, University of Cambridge, 2017.

C. A. Curran, C. P. Konrad, R. L. Dinehart, and E. H. Moran. Bank topography, bathymetry, and current velocity of the lower Elwha river, Clallam county, Washington, May 2006. Technical report, Geological Survey (US), 2008.

B. Cushman-Roisin, L. J. Pratt, and E. A. Ralph. A general theory for equivalent barotropic thin jets. *J. Phys. Oceanogr.*, 23(1):91–103, 1993.

B. Cushman-Roisin, J. A. Proehl, and D. T. Morgan. Barotropic thin jets over arbitrary topography. *Dyn. Atmos. Oceans*, 26(2):73–93, 1997.

A. C. Dale and J. A. Barth. The hydraulics of an evolving upwelling jet flowing around a cape. *J. Phys. Oceanogr.*, 31(1):226–243, 2001.

T. F. Donato and G. O. Marmorino. The surface morphology of a coastal gravity current. *Cont. Shelf Res.*, 22(1):141–146, 2002.

D. G. Dritschel. Contour surgery: a topological reconnection scheme for extended integrations using contour dynamics. *J. Comput. Phys.*, 77(1): 240–266, 1988.

D. G. Dritschel. Contour dynamics and contour surgery: numerical algorithms for extended, high-resolution modelling of vortex dynamics in two-dimensional, inviscid, incompressible flows. *Comput. Phys. Rep.*, 10(3):77–146, 1989.

G. A. El. Resolution of a shock in hyperbolic systems modified by weak dispersion. *Chaos*, 15(3):037103, 2005.

G. A. El, R. H. J. Grimshaw, and N. F. Smyth. Unsteady undular bores in fully nonlinear shallow-water theory. *Phys. Fluids*, 18(2):027104, 2006.

G. A. El, R. H. J. Grimshaw, and N. F. Smyth. Transcritical shallow-water flow past topography: finite-amplitude theory. *J. Fluid Mech.*, 640:187, 2009.

G. A. El, M. A. Hoefer, and M. Shearer. Dispersive and diffusive-dispersive shock waves for nonconvex conservation laws. *SIAM Rev.*, 59(1):3–61, 2017.

B. Engquist, P. Lötstedt, and B. Sjögreen. Nonlinear filters for efficient shock computation. *Math. Comput.*, 52(186):509–537, 1989.

J. G. Esler and J. D. Pearce. Dispersive dam-break and lock-exchange flows in a two-layer fluid. *J. Fluid Mech.*, 667:555–585, 2011.

A. V. Fedorov and W. K. Melville. Hydraulic jumps at boundaries in rotating fluids. *J. Fluid Mech.*, 324:55–82, 1996.

D. A. Fong and W. R. Geyer. The alongshore transport of freshwater in a surface-trapped river plume. *J. Phys. Oceanogr.*, 32(3):957–972, 2002.

R. W. Garvine. Frontal jump conditions for models of shallow, buoyant surface layer hydrodynamics. *Tellus*, 33(3):301–312, 1981.

R. W. Garvine. A dynamical system for classifying buoyant coastal discharges. *Cont. Shelf Res.*, 15(13):1585–1596, 1995.

R. W. Garvine. The impact of model configuration in studies of buoyant coastal discharge. *J. Mar. Res.*, 59(2):193–225, 2001.

A. E. Gill. The hydraulics of rotating-channel flow. *J. Fluid Mech.*, 80(04): 641–671, 1977.

A. E. Gill and E. H. Schumann. Topographically induced changes in the structure of an inertial coastal jet: application to the Agulhas Current. *J. Phys. Oceanogr.*, 9(5):975–991, 1979.

R. L. Gordon and J. M. Huthnance. Storm-driven continental shelf waves over the Scottish continental shelf. *Cont. Shelf Res.*, 7(9):1015–1048, 1987.

S. O. Gregorio, D. B. Haidvogel, P. J. Thomas, E. S. Taskinoglu, and A. J. Skeen. Laboratory and numerical simulations of gravity-driven coastal currents: Departures from geostrophic theory. *Dyn. Atmos. Oceans*, 52 (1):20–50, 2011.

R. H. J. Grimshaw. Resonant forcing of barotropic coastally trapped waves. *J. Phys. Oceanogr.*, 17(1):53–65, 1987.

A. V. Gurevich and L. P. Pitaevskii. Nonstationary structure of a collisionless shock wave. *Zh. Eksp. Teor. Fiz.*, 65:590–604, 1973.

P. H. Haynes, E. R. Johnson, and R. G. Hurst. A simple model of Rossby-wave hydraulic behaviour. *J. Fluid Mech.*, 253:359–384, 1993.

K. R. Helfrich. Nonlinear adjustment of a localized layer of buoyant, uniform potential vorticity fluid against a vertical wall. *Dyn. Atmos. Oceans*, 41(3):149–171, 2006.

K. R. Helfrich, A. C. Kuo, and L. J. Pratt. Nonlinear Rossby adjustment in a channel. *J. Fluid Mech.*, 390:187–222, 1999.

A. J. Hermann, P. B. Rhines, and E. R. Johnson. Nonlinear Rossby adjustment in a channel: beyond Kelvin waves. *J. Fluid Mech.*, 205: 469–502, 1989.

M. A. Hoefer and M. Ablowitz. Dispersive shock waves. *Scholarpedia*, 4 (11):5562, 2009.

J. R. Holbrook and D. Halpern. Winter-time near-surface currents in the strait of Juan de Fuca. *Atmos. Ocean*, 20(4):327–339, 1982.

J. R. Holbrook, R. D. Muench, D. G. Kachel, C. Wright, P. M. Klutznick, R. A. Frank, and W. N. Hess. Circulation in the Strait of Juan de Fuca: Recent oceanographic observations in the eastern basin. Technical report, Environmental Research Laboratories (US), 1980.

A. R. Horner-Devine. The bulge circulation in the Columbia River plume. *Cont. Shelf Res.*, 29(1):234–251, 2009.

A. R. Horner-Devine, D. A. Fong, S. G. Monismith, and T. Maxworthy. Laboratory experiments simulating a coastal river inflow. *J. Fluid Mech.*, 555:203–232, 2006.

A. R. Horner-Devine, R. D. Hetland, and D. G. MacDonald. Mixing and transport in coastal river plumes. *Annu. Rev. Fluid Mech.*, 47:569–594, 2015.

R. L. Hughes. Multiple criticalities in coastal flows. *Dyn. Atmos. Oceans*, 9(4):321–340, 1985.

P. Huq. The role of Kelvin number on bulge formation from estuarine buoyant outflows. *Estuaries Coasts*, 32(4):709–719, 2009.

A. Isobe. Ballooning of river-plume bulge and its stabilization by tidal currents. *J. Phys. Oceanogr.*, 35(12):2337–2351, 2005.

S. Jamshidi and E. R. Johnson. Coastal outflow currents into a buoyant layer of arbitrary depth. *J. Fluid Mech.*, 858:656–688, 2019a.

S. Jamshidi and E. R. Johnson. Vortex competition in coastal outflows. *J. Mar. Res.*, 77(3):325–349, 2019b.

S. Jamshidi and E. R. Johnson. The long-wave potential-vorticity dynamics of coastal fronts. *J. Fluid Mech.*, 888:A19, 2020. doi: 10.1017/jfm.2020.30.

E. R. Johnson and S. R. Clarke. Dispersive effects in Rossby-wave hydraulics. *J. Fluid Mech.*, 401:27–54, 1999.

E. R. Johnson and S. R. Clarke. Rossby wave hydraulics. *Annu. Rev. Fluid Mech.*, 33(1):207–230, 2001.

E. R. Johnson and N. R. McDonald. Vortical source-sink flow against a wall: The initial value problem and exact steady states. *Phys. Fluids*, 18 (7):076601, 2006.

E. R. Johnson, O. R. Southwick, and N. R. McDonald. The long-wave vorticity dynamics of rotating buoyant outflows. *J. Fluid Mech.*, 822: 418–443, 2017.

A. M. Kamchatnov. Dispersive shock wave theory for nonintegrable equations. *Phys. Rev. E*, 99(1):012203, 2019.

B. A. Klinger. Inviscid current separation from rounded capes. *J. Phys. Oceanogr.*, 24(8):1805–1811, 1994.

A. Kubokawa. On the behaviour of outflows with low potential vorticity from a sea strait. *Tellus A*, 43(2):168–176, 1991.

A. Kubokawa and K. Hanawa. A theory of semigeostrophic gravity waves and its application to the intrusion of a density current along a coast. *J. Oceanogr. Soc. Jpn.*, 40(4):247–259, 1984a.

A. Kubokawa and K. Hanawa. A theory of semigeostrophic gravity waves and its application to the intrusion of a density current along a coast. Part 2: Intrusion of a density current along a coast in a rotating fluid. *J. Oceanogr. Soc. Japan*, 40:260–270, 1984b.

T. Lee and P. Cornillon. Propagation of Gulf Stream meanders between 74 and 70 W. *J. Phys. Oceanogr.*, 26(2):205–224, 1996.

S. Magome and A. Isobe. Current structure and behavior of the river plume in Suo-Nada. *J. Oceanogr.*, 59(6):833–843, 2003.

M. D. Maiden, N. A. Franco, E. G. Webb, G. A. El, and M. A. Hoefer. Solitary wave fission of a large disturbance in a viscous fluid conduit. *J. Fluid Mech.*, 883, 2020.

C. M. Martell and J. S. Allen. The generation of continental shelf waves by alongshore variations in bottom topography. *J. Phys. Oceanogr.*, 9 (4):696–711, 1979.

J. R. Martin, D. A. Smeed, and G. F. Lane-Serff. Rotating gravity currents. part 2. potential vorticity theory. *J. Fluid Mech.*, 522:63–89, 2005.

J. P. McCreary, S. Zhang, and S. R. Shetye. Coastal circulations driven by river outflow in a variable-density 1 1/2-layer model. *J. Geophys. Res. – Oceans*, 102(C7):15535–15554, 1997.

A. J. Miller, P. F. J. Lermusiaux, and P.-M. Poulain. A topographic–Rossby mode resonance over the Iceland–Faeroe Ridge. *J. Phys. Oceanogr.*, 26 (12):2735–2747, 1996.

H. Mitsudera and R. H. J. Grimshaw. Resonant forcing of coastally trapped waves in a continuously stratified ocean. *Pure Appl. Geophys.*, 133(4): 635–664, 1990.

A. Münchow and R. W. Garvine. Buoyancy and wind forcing of a coastal current. *J. Mar. Res.*, 51(2):293–322, 1993a.

A. Münchow and R. W. Garvine. Dynamical properties of a buoyancy-driven coastal current. *J. Geophys. Res. – Oceans*, 98(C11):20063–20077, 1993b.

D. Nof and T. Pichevin. The ballooning of outflows. *J. Phys. Oceanogr.*, 31(10):3045–3058, 2001.

J. Nycander, D. G. Dritschel, and G. G. Sutyrin. The dynamics of long frontal waves in the shallow-water equations. *Phys. Fluids A – Fluid Dynamics*, 5(5):1089–1091, 1993.

T. Pichevin and D. Nof. The momentum imbalance paradox. *Tellus A*, 49 (2):298–319, 1997.

R. S. Pickart, T. J. Weingartner, L. J. Pratt, S. Zimmermann, and D. J. Torres. Flow of winter-transformed Pacific water into the Western Arctic. *Deep Sea Res. Part II*, 52(24-26):3175–3198, 2005.

F. M. Pimenta, A. D. Kirwan Jr, and P. Huq. On the transport of buoyant coastal plumes. *J. Phys. Oceanogr.*, 41(3):620–640, 2011.

L. J. Pratt. Meandering and eddy detachment according to a simple (looking) path equation. *J. Phys. Oceanogr.*, 18(11):1627–1640, 1988.

L. J. Pratt and M. E. Stern. Dynamics of potential vorticity fronts and eddy detachment. *J. Phys. Oceanogr.*, 16(6):1101–1120, 1986.

L. J. Pratt and J. A. Whitehead. *Rotating Hydraulics*, volume 1. Springer, 2008.

L. J. Pratt, J. Earles, P. Cornillon, and J.-F. Cayula. The nonlinear behavior of varicose disturbances in a simple model of the Gulf Stream. *Deep-Sea Res. Pt. I*, 38:S591–S622, 1991.

E. A. Ralph and L. J. Pratt. Predicting eddy detachment for an equivalent barotropic thin jet. *Journal of Nonlinear Science*, 4(1):355–374, 1994.

G. S. Saldías and S. E. Allen. The influence of a submarine canyon on the circulation and cross-shore exchanges around an upwelling front. *J. Phys. Oceanogr.*, 50(6):1677–1698, 2020.

Y. N. Sasaki and N. Schneider. Decadal shifts of the Kuroshio Extension jet: Application of thin-jet theory. *J. Phys. Oceanogr.*, 41(5):979–993, 2011a.

Y. N. Sasaki and N. Schneider. Interannual to decadal Gulf Stream variability in an eddy-resolving ocean model. *Ocean Modell.*, 39(3-4): 209–219, 2011b.

S. R. Shetye, A. D. Gouveia, S. S. C. Shenoi, D. Sundar, G. S. Michael, and G. Nampoothiri. The western boundary current of the seasonal subtropical gyre in the Bay of Bengal. *J. Geophys. Res. – Oceans*, 98 (C1):945–954, 1993.

O. R. Southwick, E. R. Johnson, and N. R. McDonald. Potential vorticity dynamics of coastal outflows. *J. Phys. Oceanogr.*, 47(5):1021–1041, 2017.

M. A. Spall, R. S. Pickart, P. S. Fratantoni, and A. J. Plueddemann. Western Arctic shelfbreak eddies: Formation and transport. *J. Phys. Oceanogr.*, 38(8):1644–1668, 2008.

M. E. Stern. Geostrophic fronts, bores, breaking and blocking waves. *J. Fluid Mech.*, 99(4):687–703, 1980. doi: 10.1017/S0022112080000833.

M. E. Stern. On the amplification of convergences in coastal currents and the formation of squirts. *J. Mar. Res.*, 44(3):403–421, 1986.

M. E. Stern and K. R. Helfrich. Propagation of a finite-amplitude potential vorticity front along the wall of a stratified fluid. *J. Fluid Mech.*, 468: 179–204, 2002.

M. E. Stern and L. J. Pratt. Dynamics of vorticity fronts. *J. Fluid Mech.*, 161:513–532, 1985.

M. E. Stern and J. A. Whitehead. Separation of a boundary jet in a rotating fluid. *J. Fluid Mech.*, 217:41–69, 1990. doi: 10.1017/S0022112090000623.

M. E. Stern, J. A. Whitehead, and B. L. Hua. The intrusion of a density current along the coast of a rotating fluid. *J. Fluid Mech.*, 123:237–265, 1982.

C. E. Tansley and D. P. Marshall. On the influence of bottom topography and the Deep Western Boundary Current on Gulf Stream separation. *J. Mar. Res.*, 58(2):297–325, 2000.

P. J. Thomas and P. F. Linden. Rotating gravity currents: small-scale and large-scale laboratory experiments and a geostrophic model. *J. Fluid Mech.*, 578:35–65, 2007.

K. L. Tracey, D. R. Watts, K. A. Donohue, and H. Ichikawa. Propagation of Kuroshio Extension meanders between 143° and 149° E. *J. Phys. Oceanogr.*, 42(4):581–601, 2012.

H. Tsujino, N. Usui, and H. Nakano. Dynamics of Kuroshio path variations in a high-resolution general circulation model. *J. Geophys. Res. – Oceans*, 111(C11), 2006.

G. K. Vallis. *Atmospheric and oceanic fluid dynamics.* Cambridge University Press, 2017.

A. K. Wåhlin, O. Kalen, K. M. Assmann, E. Darelius, H. K. Ha, T.-W. Kim, and S. H. Lee. Subinertial oscillations on the Amundsen Sea shelf, Antarctica. *J. Phys. Oceanogr.*, 46(9):2573–2582, 2016.

J. A. Whitehead and A. R. Miller. Laboratory simulation of the gyre in the Alboran sea. *J. Geophys. Res. – Oceans*, 84(C7):3733–3742, 1979.

J. A. Whitehead and J. Salzig. Rotating channel flow: Control and upstream currents. *Geophys. Astrophys. Fluid Dyn.*, 95(3-4):185–226, 2001.

A. E. Yankovsky. The cyclonic turning and propagation of buoyant coastal discharge along the shelf. *J. Mar. Res.*, 58(4):585–607, 2000.

A. E. Yankovsky and D. C. Chapman. A simple theory for the fate of buoyant coastal discharges. *J. Phys. Oceanogr.*, 27(7):1386–1401, 1997.

W. G. Zhang and S. J. Lentz. Wind-driven circulation in a shelf valley. part I: Mechanism of the asymmetrical response to along-shelf winds in opposite directions. *J. Phys. Oceanogr.*, 47(12):2927–2947, 2017.